FACULTY
OF MATHEMATICS
AND PHYSICS
Charles University

MASTER THESIS

Matúš Hodoš

Raman spectroscopic study of biogenic crystals of sulphate and phosphate complexes with alkaline earth metals present in microorganisms

Division of Biomolecular Physics
Institute of Physics of Charles University

Supervisor of the master thesis: doc. RNDr. Peter Mojzeš, CSc.

Study programme: Biophysics and Chemical Physics

Prague 2024

I declare that I carried out this master thesis independently, and only with the cited sources, literature and other professional sources.

I understand that my work relates to the rights and obligations under the Act No. 121/2000 Coll., the Copyright Act, as amended, in particular the fact that the Charles University has the right to conclude a license agreement on the use of this work as a school work pursuant to Section 60 paragraph 1 of the Copyright Act.

In Prague 18.07.2024 Matúš Hodoš

I would like to express my deepest gratitude to my supervisor doc. RNDr. Peter Mojzeš, CSc., for his patience, guidance, support and encouragement during sample preparation, measurements and writing of this thesis.

I would also like to express my gratitude thank all of my teachers for the vast amount of knowledge they have shared with me.

Finally, I would like to extend my heartfelt thanks to my family, friends and my girlfriend for their unwavering support and encouragement throughout my academic journey.

Title: Raman spectroscopic study of biogenic crystals of sulphate and phosphate complexes with alkaline earth metals present in microorganisms

Author: Matúš Hodoš

Department: Institute of Physics, Charles University

Supervisor: doc. RNDr. Peter Mojzeš, CSc., Institute of Physics of Charles University

Abstract: It has been known for several tens of years that many microorganisms can form intracellular crystal inclusions. One of these crystal inclusions groups consists of microcrystals of barite (BaSO4) and celestine (SrSO4), which occur in some freshwater and marine microorganisms. Their function and, in general, the way of their formation is not completely clarified, despite several hypotheses. Another interesting group of intracellular crystal inclusions are complexes of some divalent cations with phosphates, for example, pyrophosphate, which plays an important role in the energy cycle of cells. This diploma thesis aims to prepare a series of microcrystals of barium and strontium, with different stoichiometric ratios, with sulphates and phosphates and their subsequent analysis using confocal Raman spectroscopy. The analysis of these spectra will subsequently serve for the qualitative characterization of crystal inclusions in living cells.

Keywords: barite, celestine, Raman spectroscopy, intracellular inclusions

Název práce: Studium biogenních krystalů síranových a fosfátových komplexů s kovy alkalických zemin vyskytujících se v mikroorganismech pomocí Ramanovy spektroskopie

Autor: Matúš Hodoš

Ústav: Fyzikální ústav UK

Vedoucí diplomové práce: doc. RNDr. Peter Mojzeš, CSc., Fyzikální ústav UK

Abstrakt: Už niekoľko desiatok rokov je známe že mnohé mikroorganizmy sú schopné tvoriť intracelulárne kryštálové inklúzie. Jednu zo skupín týchto kryštálových inklúzií tvoria mikrokryštály barytu ($BaSO_4$) a celestinu ($SrSO_4$), ktoré sa vyskytujú v niektorých sladkovodných ale aj morských mikroorganizmoch. Ich funkcia a celkovo spôsob ich vzniku nie je úplne objasnený napriek niekoľkým hypotézam. Ďalšiu zaujímavú skupinu intracelulárnych kryštálových inklúzií predstavujú komplexy niektorých dvojmocných katiónov s fosfátmi, napríklad pyrofosfátom, ktorý hrá dôležitú rolu v energetickom cykle buniek. Cieľom tejto diplomovej práce je preto pripraviť série mikrokryštálov bária a stroncia, s rôznym stechiometrickým pomerom, so síranmi a fosfátmi a ich následná analýza pomocou konfokálnej Ramanovej spektroskopie. Analýza týchto spektier následne poslúži ku kvalitatívnej charakterizácií kryštálových inklúzií v živých bunkách.

Klíčová slova: baryt, celestin, Ramanova spektroskopia, intracelulárne inklúzie

Contents

Introduction

Ever since its discovery in the first half of the 20th century, the question of particular barite and celestine (to a lesser extent) has intrigued the scientific community of marine biologists and biogeochemists. Mainly because of its nutrient-like distribution in the entire seawater column (Dehairs et al., 1980; Monnin, 1999) and despite the very low concentration of free Ba, which was well below the saturation level enabling its chemical precipitation into barite. This led scientists to hypothesize that the formation of particular barite and celestine may be induced by some marine organisms. Nowadays it is known that some marine and freshwater microorganisms actively accumulate Ba and Sr to the extent that they form microcrystals in their cells (Gonzalez-Munoz et al., 2003; Krejci, Finney, et al., 2011; Krejci, Wasserman, et al., 2011; Niedermeier et al., 2018; Pilátová et al., 2023).

This diploma thesis aims to shed a little more light on the question of particular barite and celestine function and formation in microorganisms. There are some hypotheses on the function which these crystal inclusions may have. The most prominent two are: 1) that these crystal inclusions can play a role in graviperception, or 2) they can help cells with the change in buoyancy and therefore facilitate an adjustment of depth in the water column (Raven & Knoll, 2010), which can be critical to nutrient intake. But the question of their formation is, at least for us, more important. For this purpose, we conducted a series of experiments *in vitro* and *in vivo* simulating possible means of formation of these crystal inclusions. *In vitro* experiments consist of precipitation of barium-strontium crystal series with different stoichiometric rations, using sulphate, orthophosphate, pyrophosphate and triphosphate. We also wanted to explore the idea of Ba being in the solid state, as opposed to the standard setup – Ba ions being in the liquid media from which crystals precipitate. This experiment was also conducted with sulphate, orthophosphate, pyrophosphate, and triphosphate, and yielded some interesting results. For the last *in vitro* experiment, we prepared "agarose sheets" which contained a DNA sample from the calf thymus. In this experiment, we wanted to simulate the presence of phosphate groups as some sort of ion trap which should act as a pre-concentrator of Ba ions in the cells. For our *in vivo* experiments we used two strains of freshwater algae from the genus *Closterium*, which were fed "pure" medium without added Ba or Sr, or medium with added Ba or Sr. To characterize our samples,

we used an already well-established method of Raman microscopy, for its easy-to-use approach, consistent results and ability to precisely localize crystal inclusions of micron sizes in cells. For part of our samples, we used electron microscopy as an additional method of characterization, namely, to see the degree of crystallinity of our samples.

Some of the questions that we would like to answer in this diploma thesis include: What is the difference between crystals precipitated from solutions of different molar ratios of Ba:Sr? Does some spectral characteristic exist that would enable us to precisely identify the Ba:Sr molar ratio of the initial solution? Is there a similarity with crystals precipitated from BaCl2 or SrCl2 solution and consequently transferred to the SrCl2 or BaCl2 solution respectively? Is there some spectral marker to help with differentiating the two cases? Are PO4 groups involved in barite formation? If so, are we able to measure and characterize its effect? Does *Closterium* exhibit some sort of preference for Ba/Sr in crystal formation?

This diploma thesis can be divided into five main parts. In the theoretical part, we will discuss the general properties of barite and celestine, their categorization with regards to the possible environments of formation and present possible hypotheses for biotic promotion in particular barite formation. Furthermore, we will discuss the theoretical principles of Raman microscopy and electron microscopy. The experimental part is focused on the preparation and measurement of the samples, used instruments and data manipulation. The third part is dedicated to the presentation of our results. In the fourth and fifth part, we will discuss and summarize all our results.

1. Theoretical part

1.1. Barite and celestine

General properties of barite and celestine

Barite ($BaSO_4$) and celestine ($SrSO_4$) are both naturally occurring minerals (as shown in Fig. 1), they represent end members of the barite-celestine solid solution series. Minerals of this series can be found in a vast range of geological and sedimentary environments. For example, barite can be found in deposits that extend hundreds of kilometres along Phanerozoic continental margins (Maynard & Okita, 1991) or as particulate barite of micron sizes in the marine water column (Dehairs et al., 1980). The time scale on which barite started to form on Earth can be roughly estimated to be 3.5 billion years ago (Hanor, 2000), which corresponds to the time period of ocean formation, up to the present time. Celestine is much more restricted in terms of geological distribution and its occurrences appear to be the product of the reaction of strontium-containing fluids with gypsum and anhydrite. The presence of celestine further reflects special geological environments where concentrations of Sr were higher than that of Ba (Hanor, 2000).

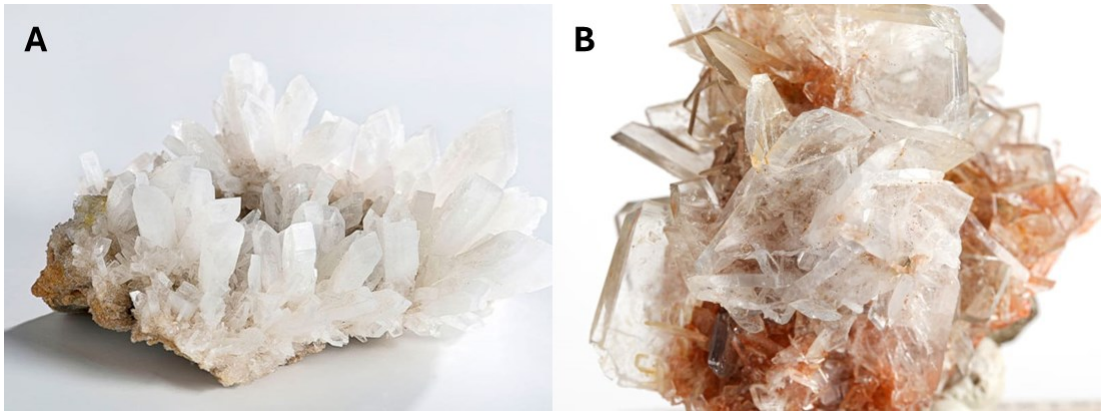

Figure 1: Examples of naturally occurring (A) barite, and (B) celestine crystals. Source: https://www.gemstones.com/

Particular barite can be divided into two major groups by its formation: (a) sedimentary barite and (b) diagenetic barite (Kravchishina et al., 2023). The sedimentary barite group consists of barite passively precipitated in the marine water column (so-called pelagic barite) and barite which was formed *via* a biological pathway by some

organism (so-called biogenic barite). Sedimentary barite particles are well known for their correlation with the bioproductivity of the oceans in the euphotic zone (Dehairs et al., 1980; Dehairs et al., 1991). This correlation has even allowed us to trace changes in ocean bioproductivity dating back nearly half a million years (Paytan et al., 1996). Currently, the sediments of particulate barite at the ocean bottom are commonly used as a proxy for past ocean bioproductivity. Diagenetic barite is of fluid-related origin, these fluids include pore water, cold seeps water and water from hydrothermal vents which are all enriched in dissolved Ba (Hein et al., 2007). It is universally recognised that diagenetic barite is formed when barium-rich fluids mix with sulphate-rich fluids, for example, seawater. Some barite crystals even contain cavities filled with fluids from the time of their formation, thus can be used as a window to the past and help us to better understand Earth´s conditions (Kravchishina et al., 2023).

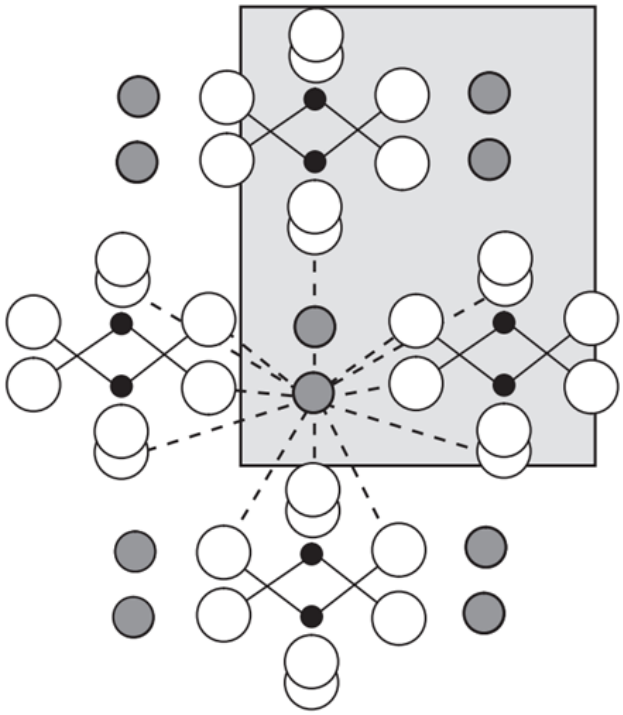

Figure 2: Barite ($BaSO_4$) or celestine ($SrSO_4$) structure projected on the [001] surface shows the 12-fold coordination of Ba or Sr. White, black and grey circles are O, S and Ba or Sr atoms, respectively. Adapted from (Paytan & Griffith, 2007).

Barite and celestine as minerals are both formed from divalent cations of alkaline-earth metal and sulphate group. Their almost identical constitution and the fact that barium ion and strontium ion have similar ionic radius of 1.34 Å and 1.18 Å respectively, leads

to the same crystallographic structure. Both minerals are orthorhombic, bipyramidal and have a space group *Pnma*. The sulphur and two oxygen atoms of each sulphate tetrahedron in the barite or celestine structure lie on a mirror plane as shown in Fig. 2. The other two oxygen atoms are equidistant above and below the plane. Barium or strontium ions lie on the same mirror plane and are in 12-fold coordination with the oxygen atoms which belong to seven different sulphate groups (Griffith & Paytan, 2012). If barium or strontium were replaced by another alkaline-earth metal such as calcium, the crystallographic structure would change from *Pnma* to *Cmcm*, with calcium in 8-fold coordination to six different sulphate groups (Gaines et al., 1997). Different ionic radius of calcium ion 1.00 Å and higher values of electronegativity 1.00 as opposed to the barium and strontium 0.89 and 0.95, respectively, are most likely responsible for this change. In addition to calcium as a possible substituent for barium or strontium, other atoms, such as potassium, radium, lead, and rare earth elements were reported also to occur (Church et al., 1979), and some minor substitutions by iron, copper, zinc, silver, nickel, mercury and vanadium were reported as well (Chang et al., 1998).

Barium and strontium cycling in a water environment

To better understand the formation of the particulate barite and celestine in oceans and its interconnection with the bioproduction of oceans in the photic zone, it is important to understand the cycles of barium and strontium in water environments. The possible processes and players participating in this global biochemical cycle are shown in Fig. 3. Common sources of barium intake in seawater can be divided into four categories. First, there is a river influx from weathering rocks and minerals from the mainland (Dehairs et al., 1980). The second is the re-dissolution of barite and other barium-containing minerals deposited as sediments in seawater (Dehairs et al., 1980). The third is an influx of dissolved barium and strontium from Earth's crust by hydrothermal vents (Von Damm, 1995) and the fourth is aerial deposition from desert sand (Moore, 1991).

Similarly, barium sinks can also be divided into several categories. First could be a formation of barite or barium-enriched celestine via chemical precipitation by sulfates abundant in seawater. The second is the formation of skeletons of some marine organisms which is known to take place in the photic zone (Pilátová et al., 2023). The

third could be not yet fully clarified biologically-assisted accumulation of barium or strontium in particulate barite but not restricted to the photic zone. However, even after accounting for all possible barium sources and sinks, we still cannot fully explain the distribution of particulate barite in the current marine environment. Just such a process, which is not limited to the photic zone but can take place throughout the water column, but on the other hand requires high biological production in the photic zone, would best explain the presence of particulate barite and its relatively uniform representation at all depths. The problem is that, for a long time, no organism or chemical process was known that would enable the local accumulation of barium in the conditions of sub-saturation concentrations to the concentrations required for its precipitation in the form of barite.

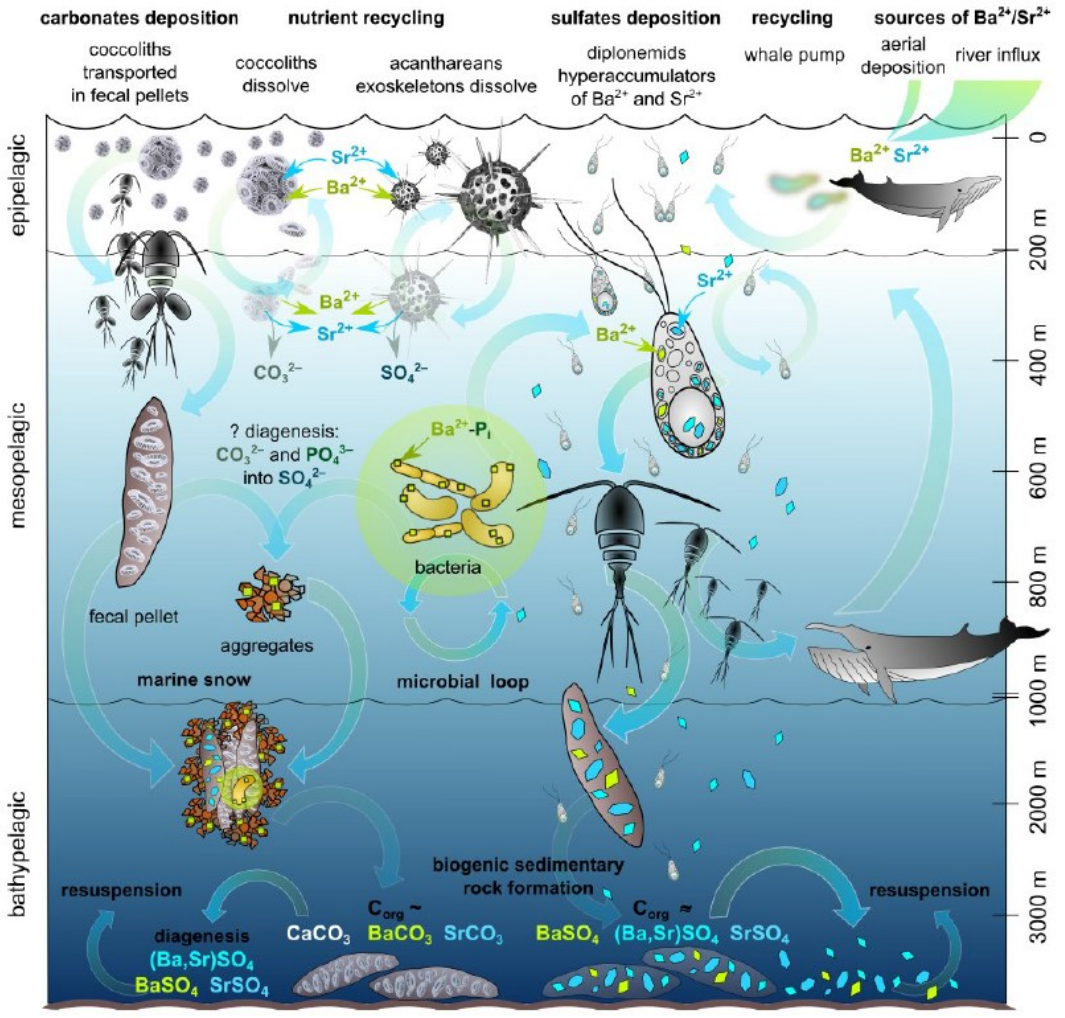

Figure 3: Schematic representation of barium and strontium cycling in the oceans, including intake of the trace elements, plankton uptake, recycling and sedimentary deposition. Adapted from (Pilátová et al., 2023)

The approximate residence time of barium in open seawater is relatively short 5×10^4 y (Chester, 1990). However, the presence of sources and sinks for barium within the water column causes significant special variations in dissolved barium (Hanor, 2000). Typical seawater concentration of barium is approximately 5-20 μg/L in open ocean settings. The lowest values were measured at the surface of the North Atlantic, while the highest values were measured in the deep waters of the North Pacific Ocean (Chan et al., 1977; Jeandel et al., 1996; Rhein et al., 1987). Although higher concentrations can be found in marine anoxic basins, such as the deep Black Sea (Falkner et al., 1993), or the anoxic hypersaline brines of the Tyro and Bannock basins, eastern Mediterranean (De Lange, Boelrijk, et al., 1990; De Lange, Middelburg, et al., 1990). Most naturally occurring waters are under-saturated with respect to barite (Monnin, 1999; Rushdi et al., 2000). Recent evidence shows pelagic barite formation at extreme barite under-saturation, suggesting that barite precipitation occurs in microenvironments where super-saturation is reached (Horner et al., 2017). Strontium is much more abundant in seawater than barium. The typical concentration of strontium is approximately in the range of 7.7-8.1 mg/L and its residence time is approximately 4×10^6 y (Chester, 1990). Sulphate is the second most common anion in modern seawater with an average concentration of 2.7 g/L and is surpassed only by chloride (Chester, 1990). All of this information and values point in the direction that to achieve barite formation, it is necessary to raise the concentration of barium or strontium, at least locally to create a suitable microenvironment.

One of the most prominent properties of barite and to a lesser extent that of celestine is their solubility, despite the solubility of their precursors. For example, the solubility of barium chloride is 375 g/L at 26°C and of strontium chloride 538 g/L at 20°C, lastly, for sodium sulphate decahydrate we have a value of 927 g/L at 30°C (Hanor, 2000). In seawater, the solubility product of barite is estimated to be around $K_{sp} \sim 8$ and for celestine $K_{sp} \sim 5$, in pK units (Rushdi et al., 2000). After a quick conversion to the same units, we get a value of solubility for barite approximately 2.3 μg/L and for celestine 1.8 mg/L. However, the actual solubility of barite and celestine is influenced by various factors such as temperature, pressure, and salinity. The effects of all of these factors are well documented. For barite, at any fixed temperature, the solubility product of barite increases with increasing pressure. At a fixed pressure, the solubility product of barite increases significantly, by nearly an order of magnitude, from 0 to

100°C. However, beyond 100°C, the solubility decreases progressively with further temperature increases. For celestine we can expect retrograde solubility, meaning its solubility decreases with increasing temperature across the entire temperature range (Bowers et al., 1984). Solubility of both barite and celestine increases with increasing salinity, at least in the range of 0 to 3 M of sodium chloride as reported (Monnin, 1999). While the effects of temperature, pressure and salinity may not influence the solubility of barite and celestine in a significant way they produce measurable changes. This very low solubility of barite in seawater led several scientists to investigate processes of its formation, occurrence in nature and possible applications. In the context of our work the most important application, based on its properties, is for barite to serve as a proxy. For example, paleo-productivity studies (Paytan et al., 1996) or studies focused on the gradual development of the water cycle on Earth.

Formation and morphology of particular barite

In the marine environment, several distinct modes of barite formation have been identified and all of them require contact and interaction between barium-rich fluids and sulphate-rich fluids, resulting in super-saturation within the environment of the formation. The origin of these fluids, the location, and the physical conditions of the environment of formation all have an impact on the barite crystal chemistry and morphology. Four general modes of barite formations were distinguished (Griffith & Paytan, 2012; Paytan et al., 2002; Widanagamage et al., 2018).

Formation of pelagic barite, the barite passively precipitated in the water column is attributed to the degrading organic matter. This creates supersaturated microenvironments through the water column, inducing precipitation of barite (Bernstein et al., 1992; Bernstein et al., 1998; Bishop, 1988). The barium content of many marine organisms is considerably higher than their surrounding environment (Fisher et al., 1991). This may provide a potential source of barium to these microenvironments through the water column in which barite precipitates (Bernstein et al., 1992; Bernstein et al., 1998; Bishop, 1988). Acantharia and bacteria have been proposed as mediators of marine barite formation (Bernstein et al., 1992; Gonzalez-Munoz et al., 2003; Gonzalez-Munoz et al., 2012). Acantahria shells are made of celestine, which usually contains barium in amounts of ppt and can be dissolved in seawater, providing both barium and sulphate to induce a supersaturated

microenvironment (Bernstein & Byrne, 2004). The work of (van Beek et al., 2007) suggests that the dissolution of acantharean shells does significantly contribute to barite formation in the upper 500 meters of the water column.

Biogenic barite as stated above is barite formed *via* biological pathway in some organisms. Some of these organisms have already been identified, for example, strains of algae from class *Zygnematophyceae* (Brook et al., 1980; Brook et al., 1988; Krejci, Finney, et al., 2011; Krejci, Wasserman, et al., 2011; Niedermeier et al., 2018; Wilcock et al., 1989), unicellular heterotrophs from class *Diplonema* (Pilátová et al., 2023), bacteria *Myxococcus xanthus* (Gonzalez-Munoz et al., 2003; Gonzalez-Munoz et al., 2012) or protozoa from class *Xenophyophorea* (Gooday & Nott, 1982). These organisms form barite crystals intracellularly, but it is not clear whether these organisms precipitate barite crystals actively or retain them in the cells during filter-feeding

As for the formation and cycling of biogenic barite, there currently exist three hypotheses. The first one is based on bacterial mediation of barite precipitation. The exact mechanism is still unknown but there is evidence that barium ions are firstly bound to the extracellular polymeric substances (EPS), which may promote the nucleation sites for barite precipitation. The EPS may be of amorphous phosphorus-rich phase nature (Martinez-Ruiz et al., 2019) or it could be the outer membrane of the cell wall, which is formed by structural polymers rich in phosphoryl and carboxyl groups. Deprotonation of these groups may provide discrete complexation sites for metals in solution (Gonzalez-Munoz et al., 2003). After the initial binding to the EPS, the phosphate groups are gradually substituted by sulphate and the barite crystals are formed.

In their work (Bernstein et al., 1992) suggested that the formation of particular barite is a thermodynamically driven process. During this process barium enriched celestine skeletons dissolve in the water column, consequently creating a barium-rich environment appropriate for barite formation. This hypothesis was further tested by (Bernstein & Byrne, 2004). The experiment was performed using crushed acantharean cysts sealed in Teflon tubes containing filtered natural seawater. During the time period of the experiment (21-158 days), the tubes were checked regularly until most of the celestine crystals were dissolved. After opening the tubes, analysis of their

contents was performed to reveal the presence of barite particles in 4 of 17 experiments, further supporting the hypothesis.

The third hypothesis heavily relies on the presence of diplonemids, as one of the most abundant groups of marine planktonic protists (Pilátová et al., 2023). In the aforementioned work, one specific species has been identified to be able to accumulate barium and strontium in conspicuous amounts 42 000 and 10 000 higher than the surrounding medium. Furthermore, planktonic copepods fed with diplonemids produced faecal pellets containing celestine. These faecal pellets travel through the water column and facilitate deposits of barite and celestine on the sea floor, which contribute to the total sedimentary barite deposition and celestine as the more soluble of the two is dissolved.

Hydrothermal diagenetic barite forms when volcanic activity associated with barium-rich fluids ascends from depths and mix with the seawater near the sea floor. The main source of barium in hydrothermal fluids is from leaching of oceanic or continental rocks driven by heat from magmatic activity (Griffith & Paytan, 2012). The size and composition of formed barite are determined by the chemical composition of the hydrothermal fluid, which in turn is determined by the amount and type of rocks it has passed through (Hanor, 2000). We can also differentiate the barite formed by the temperature of the hydrothermal fluids. At low temperatures, below 120°C, barite precipitates around so-called warm springs on the sea floor. In the temperature range of 150-250°C, where the circulation of fluids is driven by high heat, the barite is precipitated near hydrothermal plumes and forms chimneys and mounds, or within sediments as dispersed crystals (Griffith & Paytan, 2012).

Cold seeps diagenetic barite is associated with fluid flow and expulsion at the sediment-water interface. In this case barium rich fluid is pushed through the sediments by tectonic and hydrological processes not related to volcanic or hydrothermal activity (Griffith & Paytan, 2012). As these fluids pass through the sediments the barite can precipitate at or near the sea floor where they mix with sulphate-rich seawater. This type of barite is commonly found near the passive or active continental margins (Torres et al., 1996). The chemistry and seepage rate of the expelled fluids affects the amount of precipitated barite (Aloisi et al., 2004). At slow seepage rates, less than 5 cm a year, precipitation occurs in the top few meters of the

sedimentary column producing microcrystalline phases. However, when the seepage rate exceeds 100 cm a year, precipitation occurs at the sea floor rapidly enough so chimneys can form (Aloisi et al., 2004).

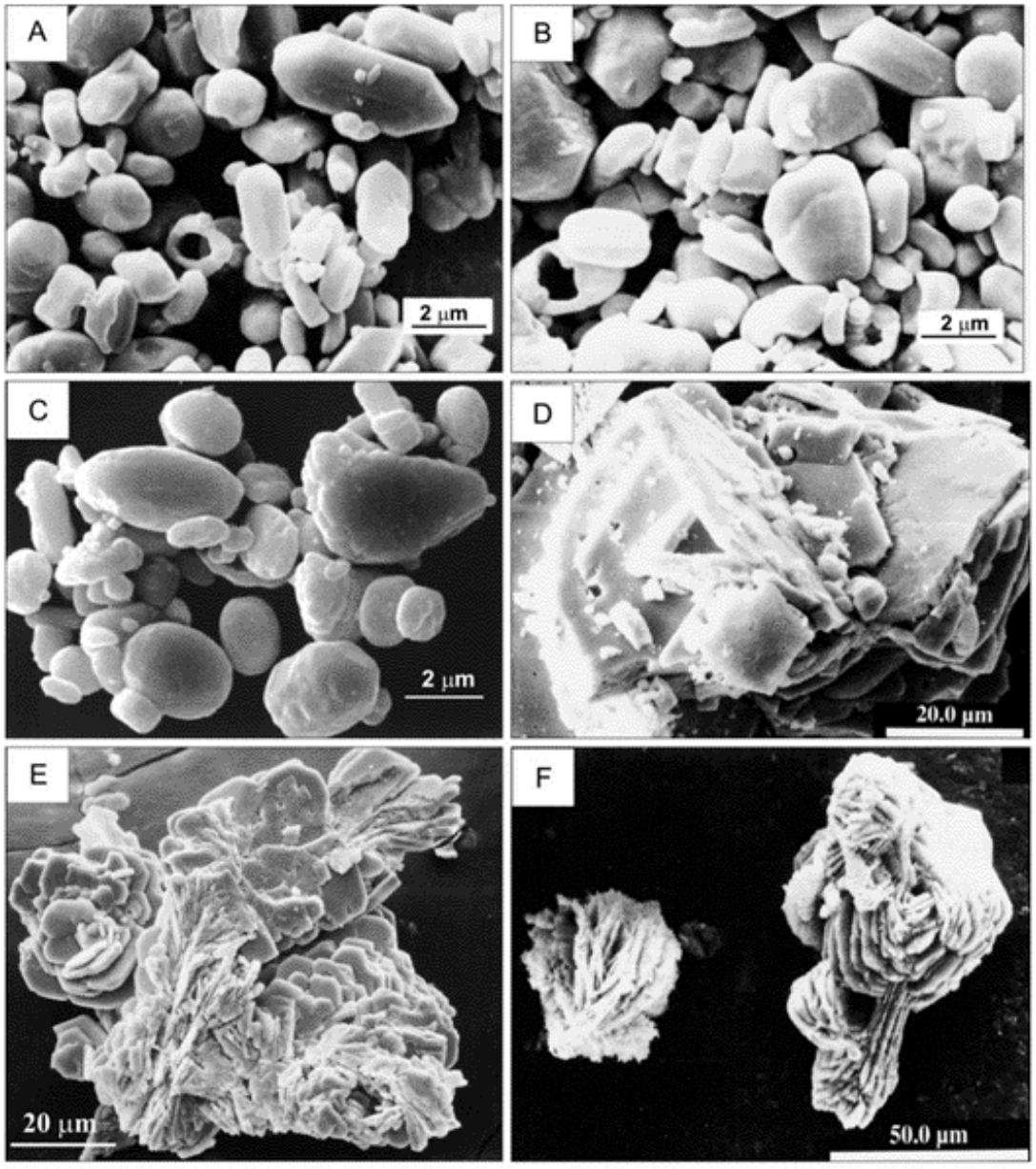

Figure 4: Scanning electron microscope image of barite crystals from different oceanic settings. A-C sedimentary barite particles from three different locations, all particles show euhedral, sub-spherical or elliptical morphology, D-F hydrothermal barite from three different locations, all particles show tabular to rosette-like morphology. Adapted from (Paytan et al., 2002)

The most common way for pore fluids diagenetic barite to be formed is through barite dissolution mediated by sulphate reduction in sediments followed by reprecipitation of barite when barium-rich pore fluids interact with pore water rich in sulphate at the redox boundaries within the sediment (Griffith & Paytan, 2012).

Since barite can form in various environments it might not be surprising that resulting crystals differ in size and morphology as shown in Fig. 4. In general crystal size and morphology are dependent on the growth conditions, such as temperature, pressure, chemical environment of the formation and the availability of surface area. Pelagic barite has been found to be mostly uniform in size and shape, typically in sub-micron up to five micrometres range, subspherical and elliptical particles with a distinct crystalline habit. This suggests that crystals formed had very stable nucleation and crystal growth rate (Griffith & Paytan, 2012). Ovoid and hexagonal barite crystals are interpreted as biogenic barite (Bertram & Cowen, 1997). Hydrothermal and cold seeps diagenetic barite can widely vary in size and morphology, they generally tend to be larger, from tens of micrometres up to several millimetres. The morphology of the crystals is usually well-formed tabular, bladed to dendric and may form rosettes (Jamieson et al., 2016; Ray et al., 2014; Widanagamage et al., 2018).

1.2. Raman microscopy

Interaction of electromagnetic field with matter

Electromagnetic fields can interact with the matter through which it passes in different ways. Besides the phenomena that arise at the interface of two substances, such as reflection or refraction of the light, electromagnetic field interacts with matter in its volume through absorption, scattering and luminescence. The electromagnetic field is described by quantum field theory using photons. The photon is the quantum of the electromagnetic field with zero mass, unit spin and energy E given field frequency f

$$E = hf \tag{1}$$

where h represents the Planck's constant. The frequency can also be expressed using values such as radial frequency ω, vacuum wavelength λ, speed of light c and wavenumber ν by the formula:

$$f = \frac{\omega}{2\pi} = \frac{c}{\lambda} = c\nu \tag{2}$$

All the matter is made from atoms and molecules. Those can receive part of the energy of the electromagnetic field or, on the contrary, lose energy themselves to the benefit electromagnetic field. These energy changes correspond to transitions between energy states of the electron shell and, in the case of molecules, their changes in vibrational and rotational energy states. Electronic, vibrational, and rotational states of the molecules are according to quantum theory discrete (quantized), *i.e.* they can only have certain values. The law of conservation of energy gives us the resonant nature of energy exchange between electromagnetic field and the matter. An absorbed or created photon must have the same energy as the difference between the energy states, which participate in said transition. This energy difference is called the energy of the transition.

The molecule has a total of 3N degrees of freedom, where N is the number of atoms. Three degrees of freedom are assigned to the translational movement of the molecule as a whole, which can be separated by transitioning to the centre-of-mass system, which is moving together with the centre of mass of the molecule. There are another

three degrees of freedom assigned to the rotational movements of the entire molecule or two for a linear molecule. Rotational states can be separated in the approximation of the fixed position of the nuclei if the influence of vibration on rotation is neglected. The rotational states of the molecule are also quantized and can exchange energy with an electromagnetic field. The energies of rotational transitions are low and correspond to the electromagnetic field with a wavelength in the order of millimetres.

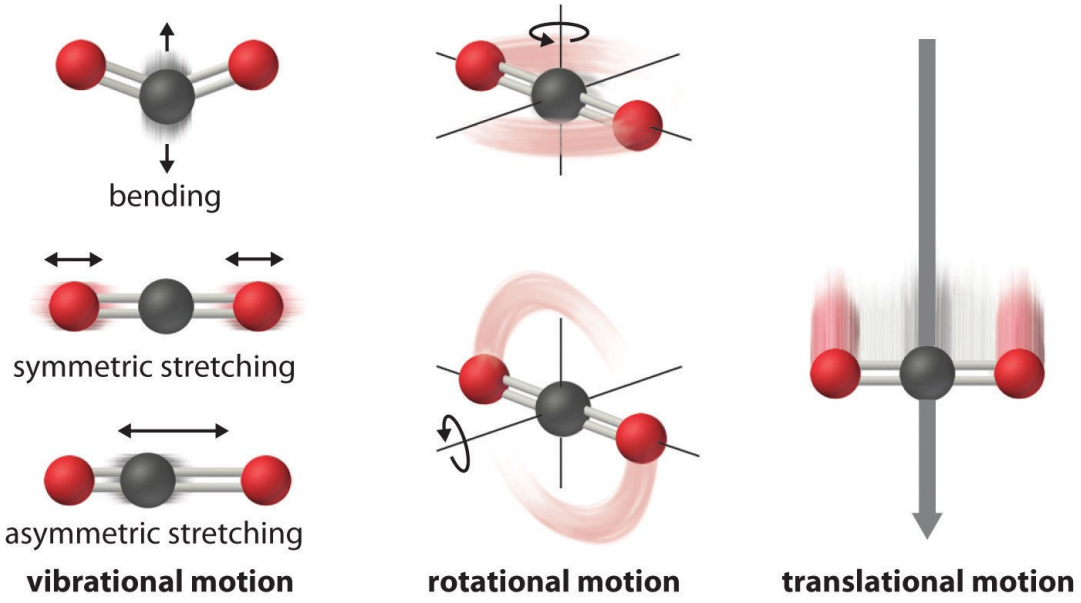

Figure 5: Illustration of vibrational, rotational and translational states of the carbon dioxide as an exemplary molecule. The fourth vibrational state is not shown (same movement as bending only perpendicular to the plane). Source: https://2012books.lardbucket.org/books/principles-of-general-chemistry-v1.0/s22-04-entropy-changes-and-the-third-.html

After all these steps of separations, we are left with either 3N – 6 (or 3N – 5 for a linear molecule) vibrational degrees of freedom. For example, a molecule of carbon dioxide a linear molecule consisting of three atoms, has nine degrees of freedom, three of which are assigned to the translation, two are bound to rotation, therefore four are left to vibrations as shown in Fig. 5. For the vibrational states of a molecule we can establish, the so-called normal coordinates. Using these coordinates, the solution of the stationary Schrödinger equation, in the approximation of small deviations of nuclei from the equilibrium position and in the harmonic approximation, is reduced to the problem of finding the solution for 3N – 6 or 3N – 5 harmonic oscillators that can

exchange energy with an electromagnetic field accordingly with the selection rules. Wavelengths of absorbed light typically correspond to infrared radiation. The vibrational states of molecules generally differ for their individual electronic states. Combined transitions can also occur in the molecule when they simultaneously change the electronic, vibrational and rotational state of the molecule or some combination of two from the three listed.

Individual transitions which can happen during the interaction of molecule and electromagnetic field can be shown in the so-called Jablonski diagram, named after the Polish physicist Aleksander Jablonski. The Jablonski diagram for scattering is shown in Fig. 6, and for absorption and luminescence (fluorescence and phosphorescence) is shown in Fig. 7. The ground, first excited and second excited electronic singlet states are marked S_0, S_1 and S_2 respectively, first excited electronic triplet state is marked T_1. To each electronic state, we have a corresponding series of vibrational states (weaker lines) and rotational states (not shown).

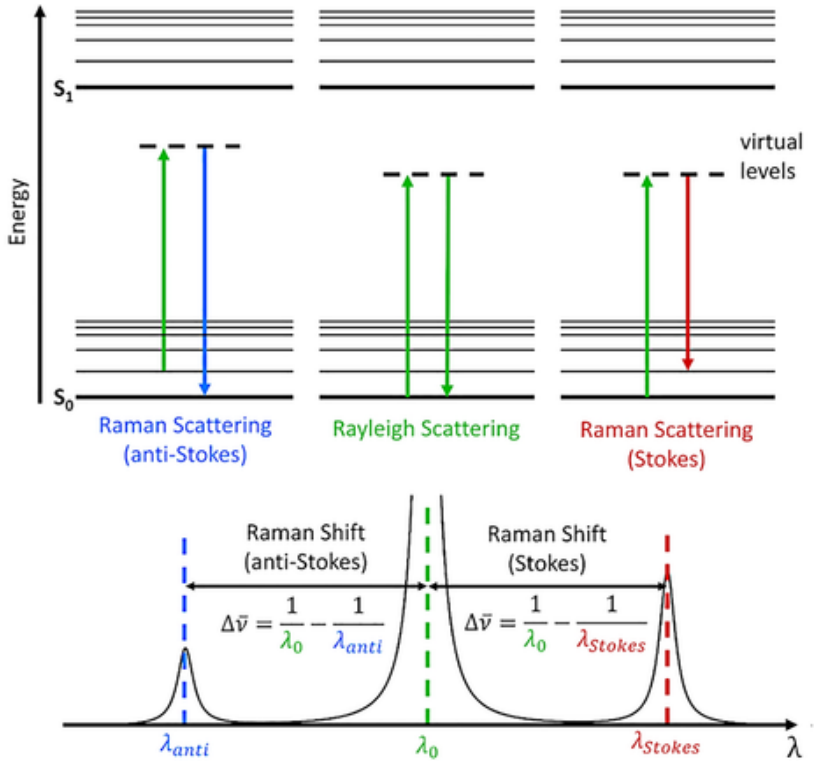

Figure 6: Jablonski diagram for Rayleigh and both branches of Raman scattering. Adapted from (Dey, 2022).

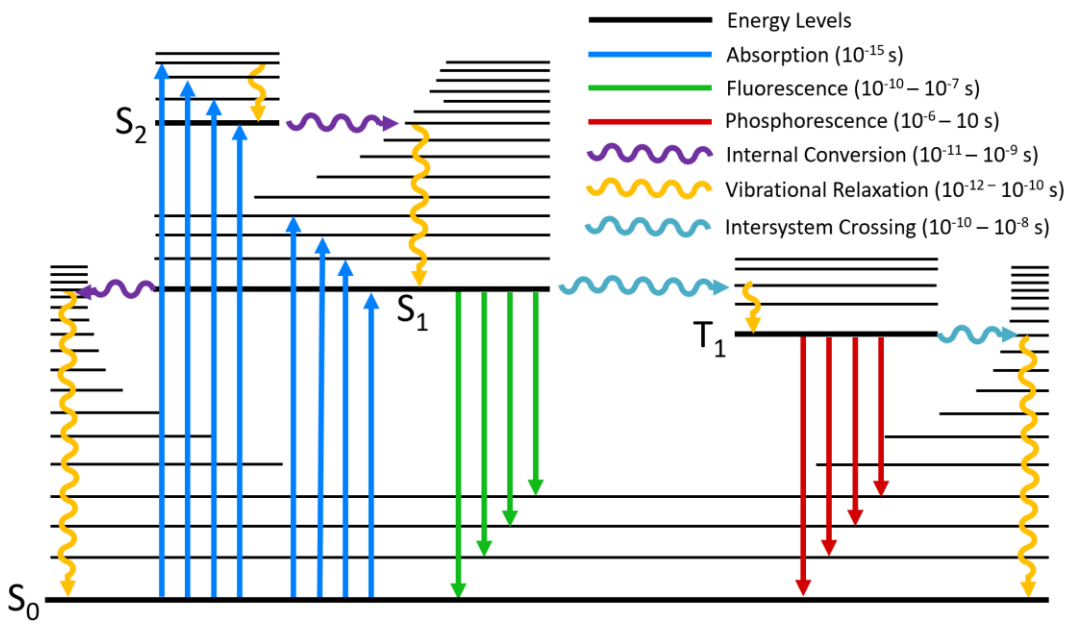

Figure 7: Jablonski diagram for absorption, fluorescence and phosphorescence. Waved lines represent non-radiative transitions and straight lines represent transitions in which absorption or creation of the photon is involved. Time scales of the transitions included. Source: https://www.edinst.com/de/blog/jablonski-diagram/

Absorption is a photophysical process wherein the energy of a photon is transferred to a molecule, provided the photon's energy matches the energy difference between two distinct molecular energy states. This transfer occurs almost instantaneously, typically within picoseconds. Upon absorbing a photon, the molecule transitions to an excited state, where it remains for a characteristic duration known as the excited state lifetime, which varies depending on the specific state and molecule. Subsequently, the molecule can return to the ground state through various photophysical pathways, including fluorescence, phosphorescence, or non-radiative decay.

Luminescence is a photophysical process during which a molecule emits photons as it transitions from an excited state to a lower energy state, typically the ground state. This process occurs after the molecule has absorbed energy, which can be from various sources such as photons, chemical reactions, or electrical energy. The emitted light's wavelength and intensity depend on the energy states involved in the transition and the specific characteristics of the molecule. Luminescence can be classified into different types based on the excitation source and the mechanism of emission. However, the most common type of classification is based on the electronic state of the molecule

before the transition. For the singlet-to-singlet transition term fluorescence is used. Fluorescence generally follows immediately after the absorption of the incident photon, can be observed on the timescale of nanoseconds, and has a longer wavelength than the absorbed photon. Phosphorescence, on the other hand, involves a longer timescale, usually ranging from milliseconds to seconds, as the molecule transitions from an excited triplet state to the ground state, often involving intersystem crossing. The study of luminescence provides valuable insights into molecular structure, dynamics, and interactions.

Among the three interactions of an electromagnetic field with matter stated above, we considered scattering the most significant in the context of this thesis. Scattering is a two-photon process involving interaction between the electromagnetic field and the molecule. One photon is annihilated, and simultaneously, another photon is created. When the scattered photon has the same wavelength as the incident photon, the process is elastic (Rayleigh scattering). On the other hand, if the scattered photon has a different wavelength, which corresponds to the energy difference between two vibrational states, the process is inelastic (Raman scattering). If the scattered photon is less energetic than the photon of the incident field, then a portion of the energy is transferred to the molecule, and we are talking about the Stokes branch of Raman scattering. In contrast, if the molecule discards part of its energy and was initially in an excited vibrational state, the scattered photon is more energetic, characterizing the anti-Stokes Raman scattering (see Fig. 6). To achieve a scattering, the energy of the incident photon does not have to be exactly the same as the energy of the transition between the states. In this case, we are talking about excitation to the virtual state, which suffices, especially when trying to analyse ground state vibrations.

Raman scattering

In the previous section, we described possible ways in which electromagnetic fields can interact with matter including Raman scattering. In this section, we will discuss the theoretical principles of Raman scattering from classical and quantum perspectives, compare Stokes and anti-Stokes branches and finally selection rules for vibrations we can expect in Raman spectra.

From the point of view of classical physics, we can describe Raman scattering by examining the behaviour of polarizable molecules in an oscillating electric field. An electric field with amplitude E_0 oscillating with frequency ω_{field} induces an electric dipole proportional to the polarizability α of the molecule that can be expressed as

$$\vec{\mu}\,(t) = \vec{\vec{\alpha}}\,\overrightarrow{E_0}\cos\left(\omega_{field}t\right) \tag{3}$$

where t is time. While the oscillating dipole can be responsible for the absorption or elastic scattering of photons, the polarizability of the molecule α changes during molecular vibrations (Shipp et al., 2017). The atomic nuclei in the molecule exhibit vibrational movements, which can be expressed using harmonic approximation and normal coordinates as

$$q_i = q_{i0}\cos(\omega_i t + \delta_i)\,, i = 1 \ldots 3N - 6 \tag{4}$$

where index i denotes degrees of freedom, index 0 denotes equilibrium position, ω_i is the frequency of *i-th* vibration and δ_i is the phase of the *i-th* vibration with respect to the incident electric field. Under the right conditions, specifically when the amplitude of the electric field E_0 is relatively small and does not induce bond breakage. We can assume that displacement from the equilibrium position is small, therefore we can expand the polarizability α in a Taylor series.

$$\vec{\vec{\alpha}} = \vec{\vec{\alpha_0}} + \sum_{i=1}^{3N-6}\left(\frac{\partial\vec{\vec{\alpha}}}{\partial q_i}\right)_0 q_i + \frac{1}{2}\sum_{i,j=1}^{3N-6}\left(\frac{\partial^2\vec{\vec{\alpha}}}{\partial q_i q_j}\right)_0 q_i q_j + \ldots \tag{5}$$

We will restrict ourselves to the first two terms in the expansion. After substituting equations (4) and (5) to the equation for the induced electric dipole (3) we get the desired formula

$$\begin{aligned}\vec{\mu}\,(t) &= \vec{\vec{\alpha_0}}\overrightarrow{E_0}\cos\left(\omega_{field}t\right) \\ &+ \sum_{i=1}^{3N-6}\left(\frac{\partial\vec{\vec{\alpha}}}{\partial q_i}\right)_0 \overrightarrow{E_0}q_{i0}\cos(\omega_i t + \delta_i)\,\cos\left(\omega_{field}t\right)\end{aligned} \tag{6}$$

Which can be rewritten using basic goniometric identity for the product of two cosine functions as

$$\begin{aligned}\vec{\mu}(t) &= \overleftrightarrow{\alpha_0}\overrightarrow{E_0}\cos(\omega_{field}t) \\ &+\frac{1}{2}\sum_{i=1}^{3N-6}\left(\frac{\partial\overleftrightarrow{\alpha}}{\partial q_i}\right)_0 \overrightarrow{E_0}q_{i0}\cos\left[(\omega_i+\omega_{field})t+\delta_i\right] \\ &+\frac{1}{2}\sum_{i=1}^{3N-6}\left(\frac{\partial\overleftrightarrow{\alpha}}{\partial q_i}\right)_0 \overrightarrow{E_0}q_{i0}\cos\left[(\omega_i-\omega_{field})t+\delta_i\right]\end{aligned} \quad (7)$$

As we can see from equation (7) the induced electric dipole of the molecule has three components. The first one corresponds to the emission of the radiation at the same frequency as incident radiation and, therefore, is responsible for elastic (Rayleigh) scattering. We assign the second and third terms to the inelastic (Raman) scattering with frequencies $\omega_i + \omega_{field}$ and $\omega_i - \omega_{field}$ for anti-Stokes and Stokes branches respectively. It is necessary to point out that both terms for Raman scattering include the phase of the vibrations δ_i, which usually differs for each molecule in the sample since the vibrations across the molecules of the sample are not synchronized. This has a significant implication for Raman scattering, it renders the scattered light non-coherent, allowing the scattered light from each molecule in the sample to be simply summed to form the resulting detected scattered light.

While the classical approach provides a foundational understanding, a quantum perspective offers deeper insights into the underlying mechanisms of Raman scattering, specifically the difference in intensities of Stokes and anti-Stokes bands of Raman scattering. As we already know Raman scattering is a process which can be described using two vibrational states of ground electronic state, one vibrational state of either virtual or excited electronic state and the transition between them. It would be a missed opportunity to not examine this process through Fermi´s golden rule, which can be written in the form

$$R_{|i\rangle\rightarrow|f\rangle} \approx \left|\langle f|\mu_{if}|i\rangle\right|^2 |E_0|^2 \delta(e_f) \quad (8)$$

where $R_{|i\rangle\rightarrow|f\rangle}$ is the rate of transition from initial state $|\, i\,\rangle$ to final state $|\, f\rangle$, μ_{if} is the perturbation of the Hamiltonian coupling $|\, i\,\rangle$ to $|\, f\rangle$, E_0 is the amplitude of electric

field and $\delta(e_f)$ is density o final states (Shipp et al., 2017). The transition between the states is facilitated by transition dipole $d_{|i\rangle \to |f\rangle} = \mu_{if} E_0$, which can be expressed as

$$d_{|i\rangle \to |f\rangle} = \frac{E_0}{\hbar} \sum_e \left[\frac{\mu_{ef}^{(1)} |\, e\rangle\langle e\, | \mu_{ie}^{(1)}}{\omega_{field} - \omega_{ei} - i\Gamma_e} + \frac{\mu_{ef}^{(2)} |\, e\rangle\langle e\, | \mu_{ie}^{(2)}}{\omega_{field} + \omega_{ei} + i\Gamma_e} \right] \quad (9)$$

where $|\, e\,\rangle$ is an arbitrary excited electronic state, ω_{field} is the frequency of incident light, ω_{ei} is the energy difference between initial state $|\, i\,\rangle$ and excited state $|\, e\,\rangle$ expressed as frequency and Γ_e is $\hbar/2\tau_e$, where τ_e is a lifetime of excited state (Shipp et al., 2017). As we can see from equation (9) all possible excited states $|\, e\,\rangle$ contribute to the total transition. By applying Fermi´s golden rule and limiting this examination to the most important terms, the rate of Raman scattering takes the form

$$\begin{aligned} R_{|i\rangle \to |f\rangle} &\approx \left| \langle f | \mu_{|i\rangle \to |f\rangle} | i \rangle \right|^2 \\ &\approx \sum_e \left[\frac{\langle f\, |\mu_{ef}|\, e\rangle\langle e\, |\mu_{ie}|\, i\rangle}{\omega_{field} - \omega_{ei} + i\Gamma_e} \right]^2 |E_0|^2 \delta(e_f) \end{aligned} \quad (10)$$

The two-step or two-photon nature of Raman scattering can be viewed in the numerator of equation (10). The term $\langle e\, |\mu_{ie}|\, i\rangle$ describes the transition from the initial state to the excited state and the term $\langle f\, |\mu_{ef}|\, e\rangle$ describes the transition from the excited state to the final state, usually the excited vibrational state of the ground electronic state. The equation holds true with the assumption that $\omega_{field} > \omega_{fi}$, where ω_{fi} is the frequency, which represents the energy difference between the initial and final state. In other words, the incident photon must have more energy than the energy difference between the initial and final state. This condition is usually satisfied since vibrational transition corresponds to the energies of infrared radiation.

From the classical approach, we have already derived two branches of Raman scattering, Stokes and anti-Stokes, of the same intensity. However, for the presence of an anti-Stokes branch, there is one necessary condition to fulfil, the existence of molecules in an excited vibrational state. The number of molecules in any state, at a given temperature *T*, is governed by Boltzman distribution. Accordingly, we can determine the number of molecules in the excited vibrational state N_v relative to the ground vibrational state N_g as

$$\frac{N_v}{N_g} = e^{-\frac{\hbar\omega_v}{k_B T}} \tag{11}$$

where ω_v is the frequency corresponding to the energy difference between the excited and ground vibrational states, k_B is the Boltzmann constant and T is the temperature of the sample. The number of anti-Stokes scattered photons will be proportional to the number of molecules in an excited vibrational state and therefore the ratio of anti-Stokes to Stokes intensities in Raman spectra (see Fig. 8) can be estimated as

$$\frac{I_{AS}}{I_S} = e^{-\frac{\hbar\omega_v}{k_B T}} \tag{12}$$

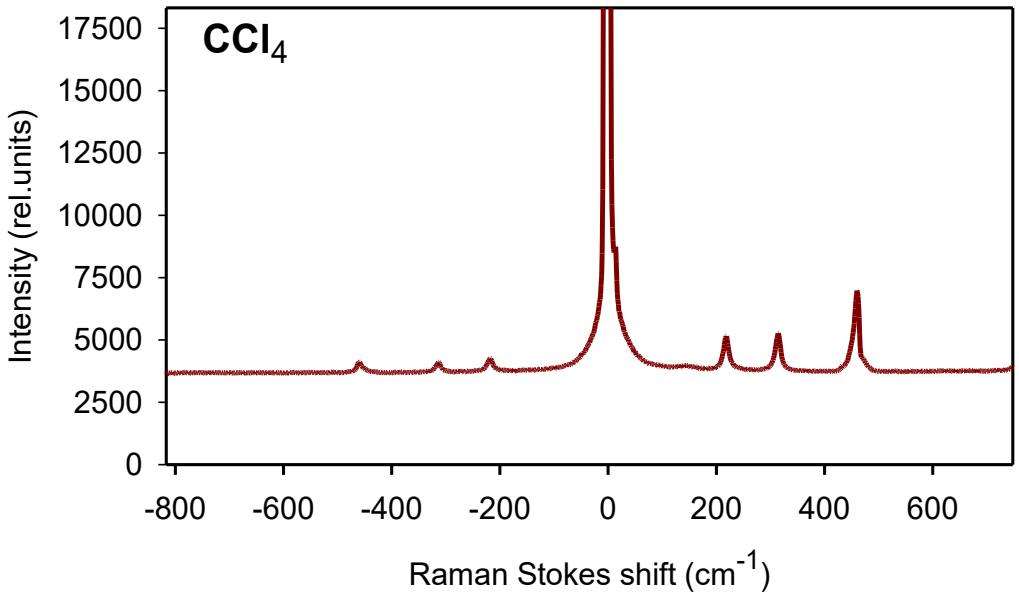

Figure 8: Raman spectra of tetrachloromethane at a given temperature T, showing both Stokes and anti-Stokes branches and the disparity in their intensities.

The selection rules, the final topic we will discuss in this section, represent one of the signature traits of the experimental approaches involving Raman scattering. As we can see from equation (7) for the Rayleigh scattering to be present it is necessary condition that polarizability of the molecules in the sample to have non-zero values. On the other hand, for Raman scattering to occur we have different conditions to fulfil, a non-zero value of the Raman tensor defined as

$$\overleftrightarrow{\alpha_i^{Raman}} = \frac{1}{2}\left(\frac{\partial \overleftrightarrow{\alpha}}{\partial q_i}\right)_0 q_{i0} \qquad (13)$$

As we can see from equation (13) Raman tensor for *i-th* vibrational state or mode depends on the first derivative of the polarizability tensor by *i-th* normal coordinate in the equilibrium position. Which can be zero and therefore not present in resulting Raman spectra. More generalized selection rules can be obtained by using group theory.

Raman microscopy

Raman microscopy, or confocal Raman microspectroscopy, is a combination of two experimental approaches, Raman spectroscopy and confocal optical microscopy. A possible scheme of the confocal microscope is shown in Fig. 9. The excitation light from the laser is focused through the objective on the sample, which is located in the focal plane of the objective on the microscope stage. The stage is usually movable by using piezoelectric motors, allowing horizontal and vertical movement. Scattered light is collected by the same objective and passes through the confocal pinhole. The presence of the pinhole is crucial, and the pinhole is positioned so that only the light from the excited point of volume of the sample is focused on the pinhole, therefore significantly reduces signal from above and below planes as shown in Fig. 10. Collected light then passes further into the spectrograph, where it is spectrally decomposed by grating, and then to the detector. The Rayleigh scattered light is filtered out by a dichroic mirror, which reflects the excitation light and allows it to pass only the inelastically scattered light, and a notch or edge filter placed between the objective and confocal pinhole. Observation of the sample is possible through the camera if the movable mirror is removed.

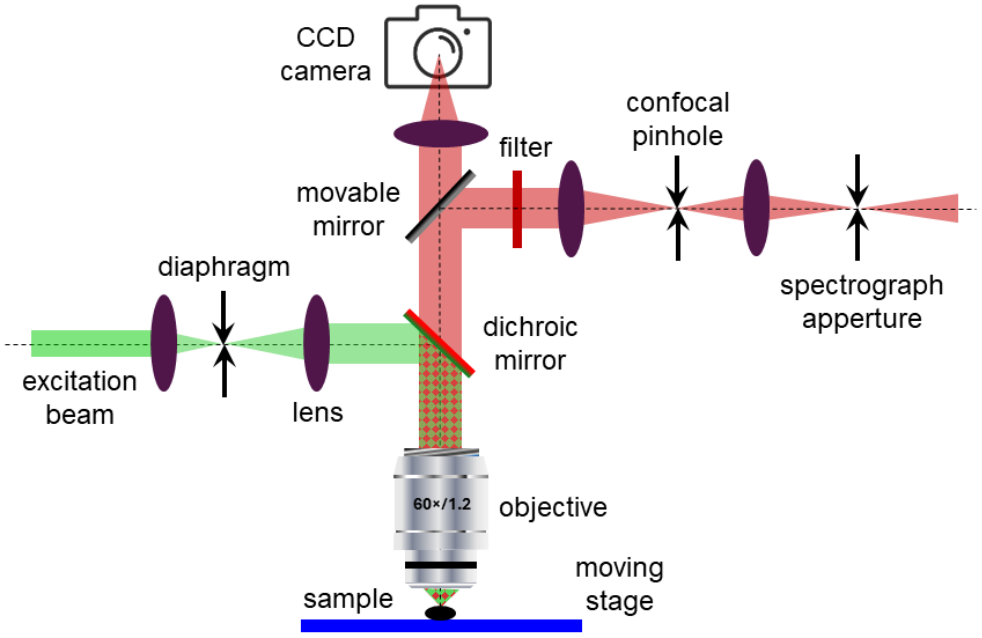

Figure 9: Possible scheme for Raman microscope. Adapted from (Mojzeš et al., 2011)

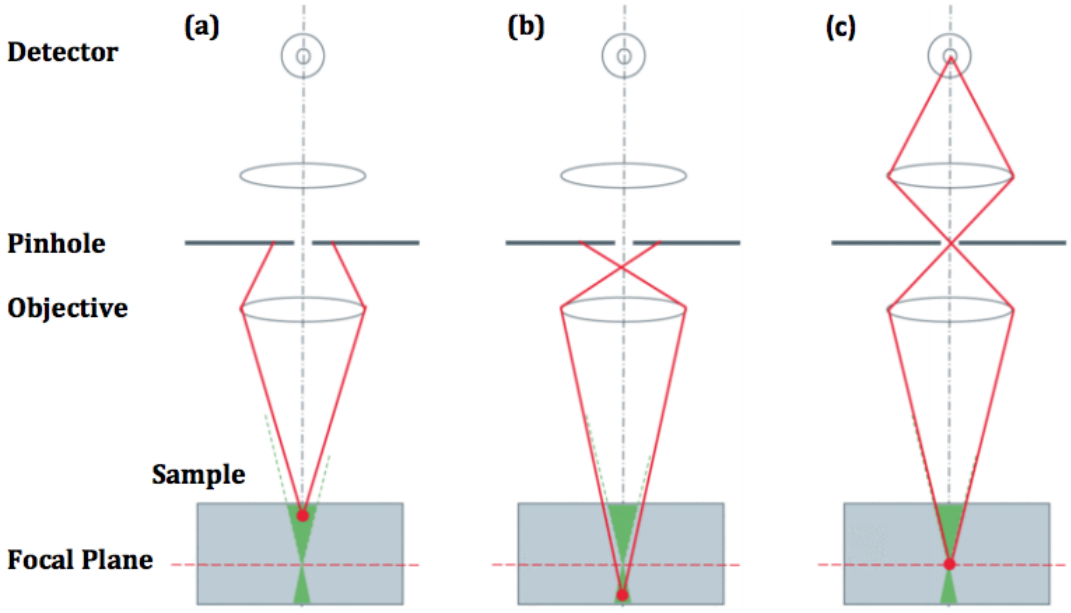

Figure 10: Effect of the confocal pinhole on the signal form (a) plane above the focal plane, (b) below the focal plane (c) the focal plane, thus significantly enhancing the signal from the measured volume of the sample.

Source: https://www.photometrics.com/learn/spinning-disk-confocal-microscopy/what-is-spinning-disk-confocal-microscopy

The principle of confocality in optical microscopy is used to enhance resolution and contrast (Hollricher & Ibach, 2010). In the image plane of the microscope, the image of the point from the focal plane is not a point but a series of concentric discs with intensity given by Airy´s function as shown in Fig. 11. The resolution of the microscope is defined as the smallest distance between the two point light sources at which we can differentiate them. Given the Rayleigh´s criterion, we can distinguish two light sources if the main maximum of the one is located in the first minimum of the other.

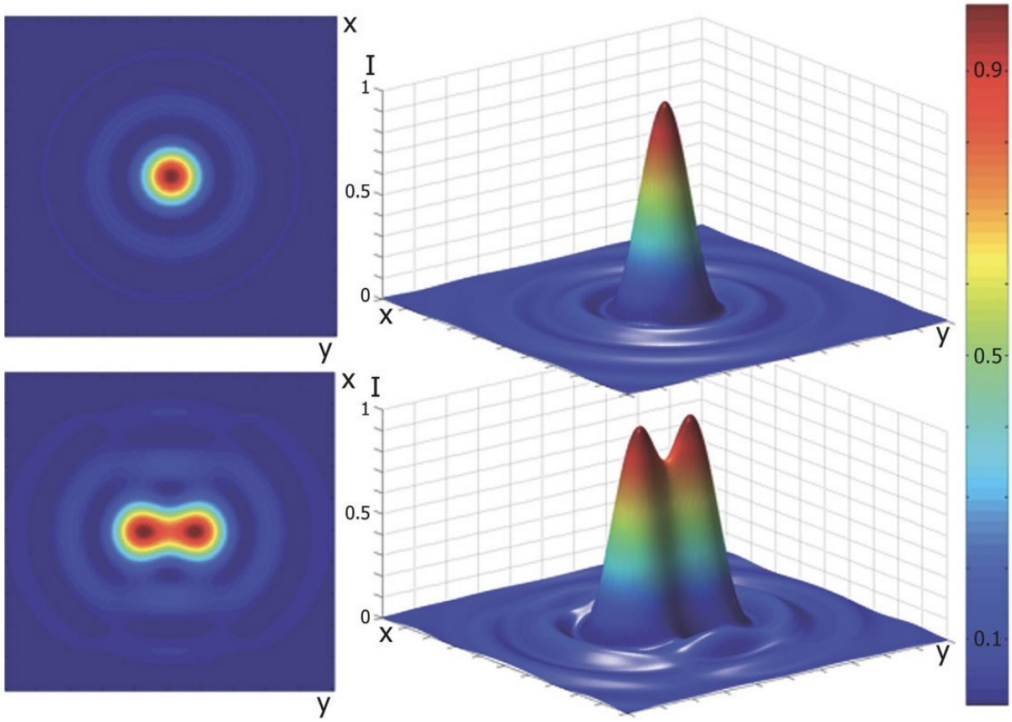

Figure 11: Intensity of Airy´s function for one-point source (upper part) and two-point sources (lower part). Adapted from (Cremer et al., 2011)

Depending on the used wavelength and the numerical aperture defined as

$$NA = n \sin \theta \tag{14}$$

where n is an index of refraction of the medium in which the objective is located and θ is the half angle of the maximum cone of light that can enter the objective. Lateral (in-plane xy) and axial (along the z-axis) resolution is given as:

$$R_{lateral} = \frac{1.22\lambda}{2NA} \tag{15}$$

$$R_{axial} = \frac{1.4\lambda n}{NA^2} \tag{16}$$

As we can see numerical aperture is directly involved, in both lateral and axial, resolution in a reciprocal way. Thus, any process leading to an increase in its value, usually using immersion fluid (water or oils), can significantly affect the resolution of the microscope.

1.3. Transmission electron microscopy - TEM

Transmission electron microscopy is a technique analogous to optical microscopy, where a ray of electrons is used instead of photons. As we already discussed optical microscopy has a limit in resolution given the used wavelength and cannot effectively overcome the resolving limit. This limitation was conquered with the use of electrons as particles which fulfil the de Broglie wave-particle duality hypothesis, which assigns wavelength to the particles of matter as

$$\lambda = \frac{h}{p} = \frac{h}{mv} \tag{17}$$

where *h* is Planck´s constant. The velocity of the electrons is given as

$$v = \sqrt{\frac{2eU}{m}} \tag{18}$$

where *e* is the charge of the electron, *U* is the accelerating voltage and *m* is the mass of the electron. By substituting equation (18) to equation (17) we obtain the relation for calculating the wavelength of the electron depending on the accelerating voltage:

$$\lambda = \frac{h}{\sqrt{2meU}} \tag{19}$$

This relation holds true for accelerating voltage $U < 100$ kV, further, we have to take into account relativistic effects.

The necessary component used for TEM to work properly is the source of electrons or electron gun, composed of a cathode, usually specifically oriented and processed crystal of lanthanum hexaboride or simply heated tungsten wire, Wehnelt cylinder and anode with a hole for an electron to pass through. Wehnelt cylinder is used to concentrate emitted electrons to the point source. After passing through the anode the ray of electrons is manipulated with the system of the electromagnetic lens to the sample (specimen in Fig. 12) stage and to the detector or phosphor screen. The general scheme of TEM is shown in the Fig. 12.

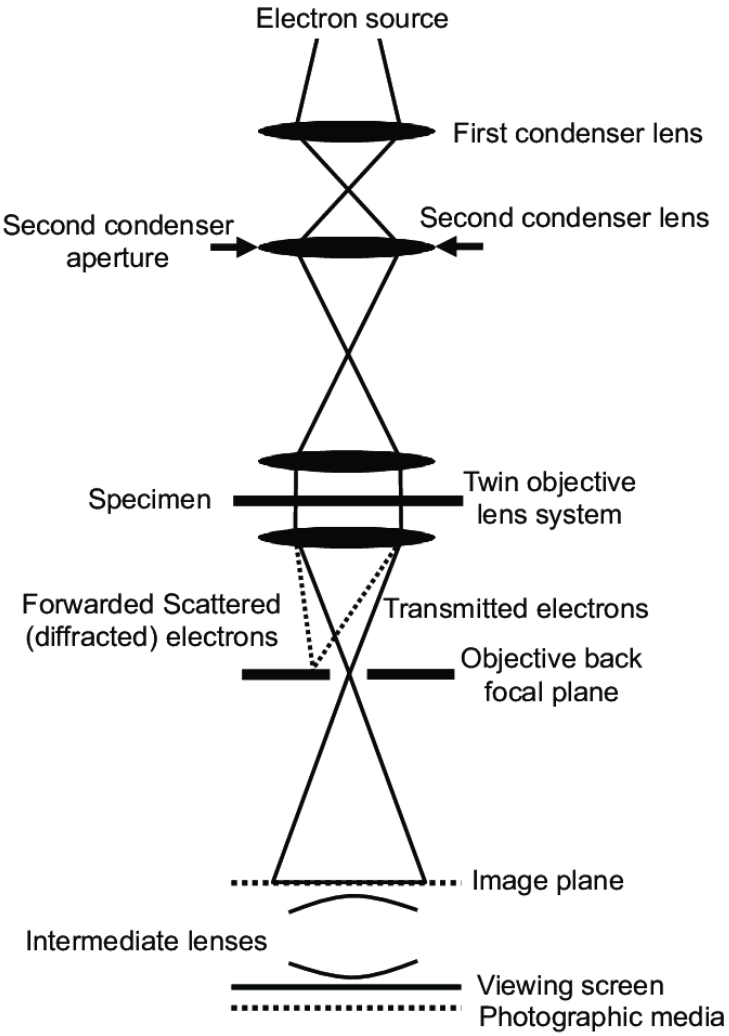

Figure 12: General scheme of TEM. Source: https://www.tribonet.org/wiki/transmission-electron-microscopy/

TEM imaging is possible in two modes brightfield and darkfield, the crucial difference being the position of the aperture. In brightfield mode, transmitted electron rays that

remain parallel to the incident rays are allowed to pass through the aperture. On the other hand, in darkfield mode, diffracted electron rays are permitted to pass through the aperture. Switching between these modes is achieved by adjusting the aperture within the microscope body as shown in the Fig. 13.

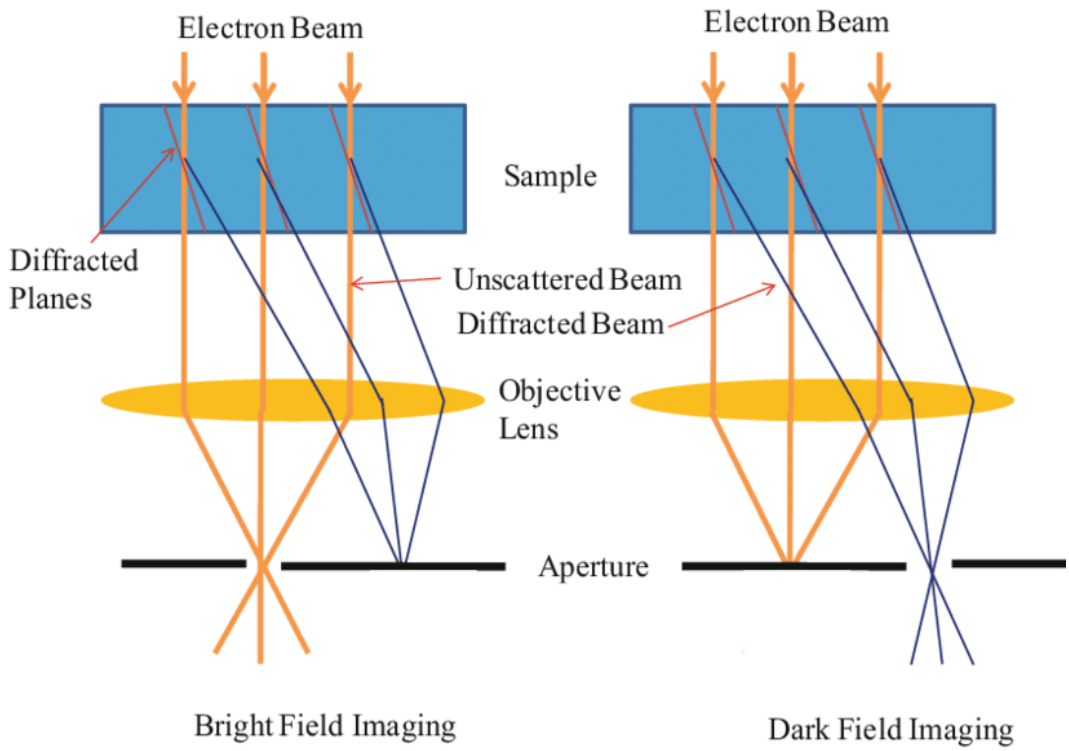

Figure 13: Schematic comparison between brightfield and darkfield imaging using TEM. Adapted from (Javed et al., 2018)

2. Experimental part

2.1. Raman microscope WITec

All Raman measurements of barite and celestine crystals, model samples, and cells were performed on a WITec alpha300 RSA confocal Raman microscope (WITec, Wissenschaftliche Instrumente und Technologie, GmbH; from 2021 part of the Oxford Instruments Group). The equipment is located in the laboratories of the Department of Biomolecular Physics, Institute of Physics, Faculty of Mathematics and Physics, Charles University. The equipment was acquired in 2015 as part of the Operational Program "Modernization of equipment for physical research and development CZ.1.05/4.1.00/16.0340" and was later upgraded and modernized several times.

The instrument is a classic upright Raman microscope based on a Zeiss Axio Scope fluorescence microscope, modified and supplemented with a tower with exchangeable modules containing fiber couplers for connecting six different laser excitations (442, 532, 633, 647, 785, and 830 nm). These couplers made it possible to introduce excitation radiation from lasers using polarization-maintaining single-mode optical fibers. The couplers were equipped with half-wave phase plates that allowed continuous rotation of the polarization plane of the excitation beam with respect to the orientation of the sample. In the detection part, the instrument was equipped with a polarization analyzer enabling the selection of scattered radiation only with the selected polarization, a camera for the optical display of the sample with a rotating polarizer, a power meter, a built-in Ar-Hg arc lamp for spectral calibration of the spectrometers and couplers for conducting the signal using special optical fibers into two optimized spectrographs.

The microscope was equipped with a set of dry metallurgic, water immersion, and immersion oil objectives with magnification ranging from 5× to 100×. In this work, the water immersion objective Olympus UPlanSApo 60×, NA 1.2, was mainly used for measuring spectra from specimens covered by coverslips. The instrument enables diascopic and episcopic illumination of the sample using white LEDs with adjustable polarization.

Positioning of the sample under the objective in the lateral x-y plane was ensured by a motorized microscope stage in the range of 25 × 25 mm. Focusing of the sample was realized by mechanical displacement of the entire detection tower of the microscope

with respect to the microscope stage and the sample, in the range of 0 - 40 mm. Mechanical displacement in all axes was possible with a step of 0.01 μm. For Raman mapping, it was possible to use the positioner with appropriate accuracy, or a piezoelectric scanning stage allowing displacement in the x, y, and z axes in the range of 200 × 200 × 20 μm, with a step of 0.001 μm.

The WITec instrument is currently equipped with six lasers of different wavelengths and fiber couplers with rotators, dichroic, and edge filters allowing to adapt the excitation wavelength to the needs of the experiment. However, in all experiments included in this thesis, a laser with a wavelength of 532 nm was used for excitation. Scattered radiation from the sample was collected by the same objective as used for sample imaging and excitation and guided through the tower modules as a collimated beam. In the respective output coupler, the radiation was focused on the entrance aperture of the endlessly single-mode photonic crystal fiber, which simultaneously served as a confocal diaphragm with a fixed dimension.

Through the fiber, the radiation was fed to one of two grating spectrographs equipped with CCD detectors, optimized for the detection of signals in the blue-green spectral region 400 - 700 nm (Newton EMCCD, Andor) and the red-infrared region 600 - 1000 nm (iDUS DU401A-BR -DD, Andor). The highly sensitive CCD detectors were cooled thermoelectrically to a working temperature of -80 °C by Peltier cells with their own cooling water circuit ensuring high thermal stability. The spectrograph for the blue-green region, which was used in this work, was equipped with two gratings: a panoramic grating with 600 grooves/mm and a grating with 1800 grooves/mm for measuring spectra with a high spectral resolution. The panoramic grating enabled a spectral region as wide as 3900 cm^{-1} with a spectral resolution of 6 cm^{-1} to be displayed on the CCD detector under 532 nm excitation. Using a grating for a high spectral resolution, a region of about 1300 cm^{-1} with a resolution of 2 cm^{-1} was displayed on the same CCD detector.

Control of the entire instrument was provided by the WITec Control Six Plus (WITec) company software supplied together with the instrument, which controlled all motorized functions. Some functions had to be set manually.

Figure 14: Photo of the Raman microscope WITec alpha300 RSA.

2.2. TEM

The TEM measurements were performed with the transmission electron microscope JEM-1400 JEOL at the Laboratory of Electron Microscopy, Biology center of Czech Academy of Sciences, České Budějovice. The JEM-1400 JEOL transmission electron microscope operates at an accelerating voltage in the range of 80 to 120 kV. It utilizes a tungsten filament cathode and offers a resolution of 0.38 nm. Image acquisition is facilitated by a 20MP CMOS camera, XAROSA (EMSIS GmbH). The microscope maintains a vacuum level of 10^{-5} Pa during operation. It is equipped with a Cryo Transfer Tomography Holder 2550, a high-tilt tomography holder capable of tilting up to 80 degrees, and a JEOL Specimen quartet holder which was used the most during our measurements.

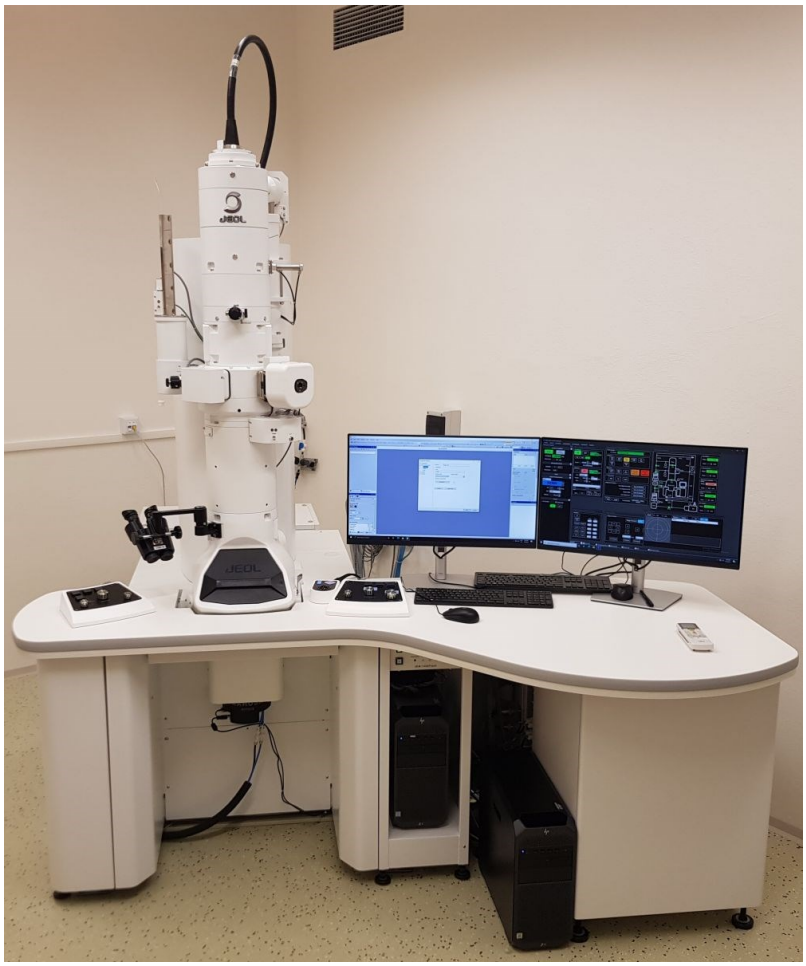

Figure 15: Photo of the transmission electron microscope JEM-1400 JEOL. Source: https://www.bc.cas.cz/en/core-facility/laboratory-of-electron-microscopy/for-users/microscopes/

2.3. Chemicals

All chemicals used in this diploma thesis are listed in Tab.1 below.

Table 1: List of chemicals used, including the producer and purity.

Formula	Producer	Purity
$BaCl_2$	Sigma-Aldrich	≥99.9%
$SrCl_2$	Sigma-Aldrich	≥99.99%
BaF_2	unknown	crystal
$Na_2SO_4 \cdot 10H_2O$	Merck	p.a., ≥99%
$HNa_2O_4P \cdot 12H_2O$	Sigma-Aldrich	puriss p.a., ≥99%
$Na_4O_7P_2 \cdot 12H_2O$	Sigma-Aldrich	puriss p.a., ≥99%
$Na_5O_{10}P_3$	Sigma-Aldrich	purum p.a. ≥98%
$Na_6[(PO_3)_6]$ sodium hexametaphosphate	Fluka	purum, 65-70% P_2O_5
Phytic acid, sodium salt hydrate	Sigma-Aldrich	≥90%
$Ca(NO_3)_2 \cdot 4H_2O$	Lachema	pur.
KNO_3	Penta	p.a., ≥99%
β-Na_2glycerophosphate$\cdot 5H_2O$	EMD Milipore	≥97%
$MgSO_4 \cdot 7H_2O$	Penta	p.a., ≥99%
Vitamin B_{12}	Sigma-Aldrich	≥98%
Biotin	Sigma-Aldrich	≥99%
Thiamine HCl	Sigma-Aldrich	≥99%
Tris (hydroxymethyl) aminomethane	Fluka	≥99.8%
$Na_2EDTA \cdot 2H_2O$	Roth	p.a., ≥99%
$FeCl_3 \cdot 6H_2O$	Lachema	p.a., ≥99%
$MnCl_2 \cdot 4H_2O$	Penta	p.a., ≥99%
$ZnCl_2$	Sigma-Aldrich	puriss. p.a., ≥98%
$CoCl_2 \cdot 6H_2O$	Riedel-de Haën	≥99%
$Na_2MoO_4 \cdot 2H_2O$	Penta	≥99%
Low-Melt Agarose	Carl Roth	≥99%
DNA-calf thymus	Pharmacia	research grade
DNA-salmon testes	Serva	research grade

2.4. Preparation of *in vitro* samples

First, stock solutions of $BaCl_2$, $SrCl_2$, $Na_2SO_4 \cdot 10H_2O$, $HNa_2O_4P \cdot 12H_2O$, $Na_4O_7P_2 \cdot 12H_2O$ and $Na_5O_{10}P_3$ were prepared. The volumes, weighted dry masses and final concentrations of chemicals are listed in Tab. 2 below.

Table 2: Volume, weighted dry mass and final concentration of stock solutions.

Formula	Volume [ml]	Weighted dry mass [g]	Final concentration [mM]
$BaCl_2$	50	0.2091	50
$SrCl_2$	50	0.1591	50
$Na_2SO_4 \cdot 10H_2O$	50	1.610	100
$HNa_2O_4P \cdot 12H_2O$	50	1.791	100
$Na_4O_7P_2 \cdot 12H_2O$	50	2.231	100
$Na_5O_{10}P_3$	50	1.839	100

After we prepared stock solutions we could move to preparation of our *in vitro* samples. The samples were prepared as follows: using a pipette we transferred a set volume of $BaCl_2$ and/or $SrCl_2$ solution from a stock solution to a clean 2-ml Eppendorf tube then vortexed for a few (~5) seconds to thoroughly mix the solutions and finally added set volume of Na_2SO_4, HNa_2O_4P, $Na_4O_7P_2$, or $Na_5O_{10}P_3$ solution depending on the sample series. We changed the pipette tip between each step so as not to cross-contaminate the samples or stock solutions. The volumes of each solution for each sample are listed in Tables 3-6 below. Immediately after the addition of Na_2SO_4, HNa_2O_4P, $Na_4O_7P_2$, or $Na_5O_{10}P_3$ the white cloud of precipitated crystals could be seen.

Samples were stored at room temperature in a tube holder. Before the measurement, we centrifuged the 2-ml tube for ~20 seconds at 2000 ×g to concentrate the precipitated crystals at the bottom. Consequently, the 20 µl of the sample from the bottom of the tube was pipetted to the clean tube, to which the 20 µl of the low-melting agarose was added and vortexed for a few (~5) seconds. Finally, 6 µl of the prepared sample was transferred to the quartz slide and covered with the quartz coverslip. The sample was slightly pressed to evenly distribute already solidifying agarose, sealed with CoverGrip™ Coverslip sealant and left for a few (2-5) minutes to let the sealant dry.

A sample prepared this way could be directly mounted to the microscope stage for the measurement.

Table 3: Volumes of the solutions used for the Na_2SO_4 sample series preparation.

Sample: $[Ba_{1-x}Sr_x]SO_4$	$BaCl_2$ [µl]	$SrCl_2$ [µl]	Na_2SO_4 [µl]
x = 0	100	0	900
x = 0.1	90	10	900
x = 0.2	80	20	900
x = 0.3	70	30	900
x = 0.4	60	40	900
x = 0.5	50	50	900
x = 0.6	40	60	900
x = 0.7	30	70	900
x = 0.8	20	80	900
x = 0.9	10	90	900
x = 1	0	100	900

Table 4: Volumes of the solutions used for the HNa_2O_4P sample series preparation.

Sample: $[Ba_{1-x}Sr_x]PO_4$	$BaCl_2$ [µl]	$SrCl_2$ [µl]	HNa_2O_4P [µl]
x = 0	100	0	900
x = 0.1	90	10	900
x = 0.2	80	20	900
x = 0.3	70	30	900
x = 0.4	60	40	900
x = 0.5	50	50	900
x = 0.6	40	60	900
x = 0.7	30	70	900
x = 0.8	20	80	900
x = 0.9	10	90	900
x = 1	0	100	900

Table 5: Volumes of the solutions used for the $Na_4O_7P_2$ sample series preparation.

Sample: $[Ba_{1-x}Sr_x]_2P_2O_7$	$BaCl_2$ [µl]	$SrCl_2$ [µl]	$Na_4O_7P_2$ [µl]
x = 0	100	0	900
x = 0.1	90	10	900
x = 0.2	80	20	900
x = 0.3	70	30	900
x = 0.4	60	40	900
x = 0.5	50	50	900
x = 0.6	40	60	900
x = 0.7	30	70	900
x = 0.8	20	80	900
x = 0.9	10	90	900
x = 1	0	100	900

Table 6: Volumes of the solutions used for the $Na_5O_{10}P_3$ sample series preparation.

Sample: $[Ba_{1-x}Sr_x]_3P_3O_{10}$	$BaCl_2$ [µl]	$SrCl_2$ [µl]	$Na_5O_{10}P_3$ [µl]
x = 0	500	0	250
x = 0.1	450	50	250
x = 0.2	400	100	250
x = 0.3	350	150	250
x = 0.4	300	200	250
x = 0.5	250	250	250
x = 0.6	200	300	250
x = 0.7	150	350	250
x = 0.8	100	400	250
x = 0.9	50	450	250
x = 1	0	500	250

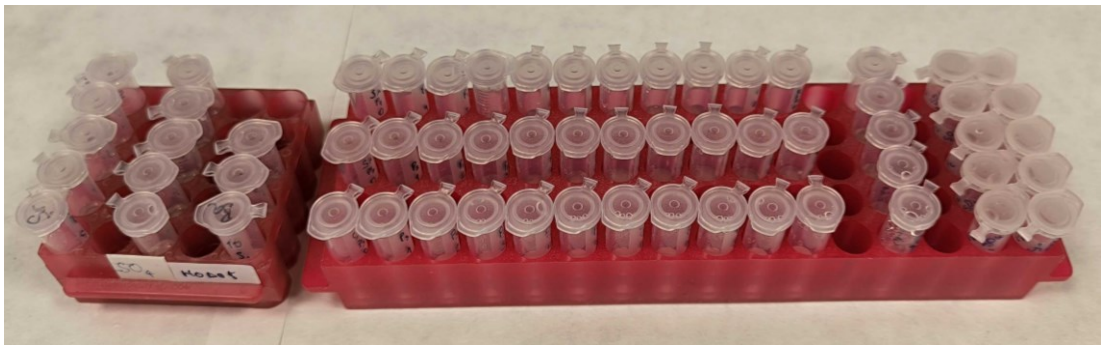

Figure 16: Photo of prepared *in vitro* samples described in Tabs. 3-6.

2.5. Preparation of BaF_2 samples

The piece of BaF_2 crystal was given to us by our colleagues. It was formerly used as a cell for infrared absorption spectroscopy. Unfortunately, it broke and was not viable for any other measurements in their research. However, since our research is heavily focused on the presence of Ba, we thought we could use it in our experiments as a solid-state substrate containing Ba.

To be able to use the crystal in the experiments it had to be manually broken down into smaller pieces approximately one millimetre thick. The pieces were transferred to the clean 2-ml Eppendorf tubes, which were afterwards filled with HNa_2O_4P, $Na_4O_7P_2$, $Na_5O_{10}P_3$, $Na_6[(PO_3)_6]$ or phytic acid solutions (as shown in Table 7) and left to rest for 24 hours. After 24 hours the crystal pieces were removed, washed with deionized water and transferred to tubes containing Na_2SO_4 solution for 24 hours. Before the measurement crystal pieces were removed, washed with deionized water, placed on a quartz slide and covered with a quartz coverslip. Since the crystals were tens to hundreds of microns thick, a small amount of warmed low-melting agarose was pipetted between the slide and the coverslip to ensure that the coverslip was stable during the measurement and did not move due to friction between the coverslip and immersion objective. After the agarose solidified the edge of the coverslip was sealed with CoverGrip™ Coverslip sealant and left for a few (2-5) minutes to let the sealant dry.

Table 7: Solution used for BaF_2 samples.

Phosphate solution [50 mM]	Sulphate solution [50 mM]
$HNa_2O_4P \cdot 12H_2O$	Na_2SO_4
$Na_4O_7P_2 \cdot 12H_2O$	Na_2SO_4
$Na_5O_{10}P_3$	Na_2SO_4
$Na_6[(PO_3)_6]$	Na_2SO_4
Phytic acid	Na_2SO_4

2.6. Preparation of DNA-agarose sheets

The first step to prepare the DNA-agarose sheets was to rehydrate 100 mg of lyophilized/freeze-dried DNA in 10 ml of deionized water. After the process of rehydration was fully completed 1.1 g of low-melting agarose was introduced and the solution was heated slightly above the melting temperature (65.5°C) of the agarose for a few minutes. While the solution was still in liquid form, the solution had to be mixed properly to ensure that the DNA was well incorporated in the agarose matrix. Then we carefully transferred 1.5 ml of the solution to the Petri dishes, so that it formed a uniform layer approximately 1 mm in thickness. Petri dishes with the DNA-agarose layer were left to dry in a dryer for 2 hours at 40°C. This process yielded dry, uniform, DNA-containing agarose sheets a few tenths of a millimetre thick. Afterwards, the sheets were cut up into smaller pieces approximately a centimetre long and half a centimetre wide to be used in the experiment. As a control in the experiment, we prepared samples with only the agarose in exactly the same way.

Samples of the agarose sheets were carefully exposed to the $BaCl_2$ or $SrCl_2$ solution in the 2-ml Eppendorf tubes for 24 hours to potentially bind the ions of Ba or Sr. The radii of Ba and Sr are small in comparison to the structure of DNA and agarose, so they should permeate freely into the agarose sheet. If the ions get to the appropriate part of the sheet with a PO_4 phosphate group or groups, they should form a complex. After 24 hours the agarose sheets were washed with deionized water and transferred to the Na_2SO_4·for another 24 hours to induce barite precipitation. Finally, sheets were removed from the sulphate solution washed again with deionized water and delicately placed on a quartz slide and covered with a quartz coverslip. Since the agarose sheets were at this point rehydrated (sheets ranged approximately a millimetre in thickness) a small amount of heated low-melting agarose was pipetted in between the slide and the coverslip. After the agarose solidified the edge of the coverslip was sealed with CoverGrip™ Coverslip sealant and left for a few (2-5) minutes to let the sealant dry.

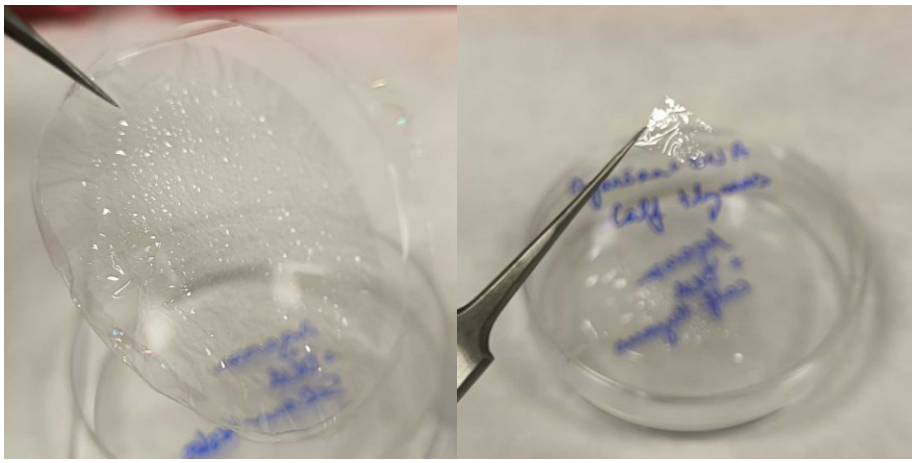

Figure 17: Photo of Petri dishes with DNA-agarose sheet (left) and prepared sample used in experiments (right).

2.7. Cultivation and preparation of algal cultures

Two freshwater algal cultures were obtained from the Microbial Culture Collection at the National Institute for Environmental Studies (NIES), Tsukuba, Japan. *Closterium peracerosum-strigosum-littorale complex* (strain NIES-68) and *Closterium moniliferum* (strain NIES-173). Cultures were cultivated in the 50-ml cell culture flasks (Greiner Bio-One, Germany) placed on the shelf near the window, therefore exposed to the natural day-night cycles and illumination of approximately 5 - 10 μmol(photons)$\cdot m^{-2} \cdot s^{-1}$, for a time period of three months prior to the experiments All cultivations of these microalgae were carried out in C medium, which was recommended by NIES. The period of three months was used to cultivate reasonable amounts of the algal cultures and to optimize the process. The cultures were transferred to the new medium every 3 weeks and were always kept in new cell culture flasks with no special coating. Each flask was filled with 20 ml of the medium-cell suspension. Before the experiment one flask of each culture (NIES-68, NIES-173) was selected and poured equally into two new flasks, if needed the new flasks were supplemented with a medium to the total volume of 10 ml. To one of the flasks, 3 μL of the $BaCl_2$ (stock) solution was added, while 4.5 μL of the $SrCl_2$ (stock) solution was added to the other. These values were calculated to reach the final concentrations of Ba or Sr in the flask of approximately 2000 μg/L. In similar work concentrations of 804 and 3744 μg/L were used (Barbosa et al., 2022). The cultures were measured 1, 3 and 7 days after the addition of Ba or Sr. On the day of the experiment, 200 μl of the cultures were

transferred into the Eppendorf tube and centrifuged for ~20 seconds at 2000 ×g to concentrate the cells. The supernatant was discarded, and a pellet was mixed with 50 µl of low-melting agarose. Finally, 6 µl of the culture was transferred to the quartz slide and covered with the quartz coverslip. The sample was slightly pressed to ensure that the cells were approximately in the same layer, sealed with CoverGrip™ Coverslip sealant and left for a few (2-5) minutes to let the sealant dry.

With the algal cultures, we also received the recipe for C medium (as shown in Tab. 8 and Tab. 9) for their cultivation. To achieve a consistent medium, we prepared stock solutions from which the medium is being prepared.

Table 8: Recipe for 100 ml of C medium.

$Ca(NO_3)_2 \cdot 4H_2O$	15 mg
KNO_3	10 mg
β-Na_2glycerophosphate$\cdot 5H_2O$	5 mg
$MgSO_4 \cdot 7H_2O$	4 mg
Vitamin B_{12}	0.01 µg
Biotin	0.01 µg
Thiamine HCl	1 µg
Tris (hydroxymethyl) aminomethane	50 mg
P IV metals	0.3 ml

Table 9: Recipe for 100 ml of P IV metals solution from Tab. 8.

$Na_2EDTA \cdot 2H_2O$	100 mg
$FeCl_3 \cdot 6H_2O$	19.6 mg
$MnCl_2 \cdot 4H_2O$	3.6 mg
$ZnCl_2$	1.04 mg
$CoCl_2 \cdot 6H_2O$	0.4 mg
$Na_2MoO_4 \cdot 2H_2O$	0.25 mg

2.8. Data acquisition and processing

The Raman mapping of the cells or model samples was performed with an excitation power of 30 mW (at the sample), with a scanning step of 200 nm in both directions, voxel size ~ 0.05 μm^3, and an integration time of 0.1 s per voxel. Data was analysed using WITec Project Six Plus v6.0 software (WITec, Germany) to implement the following steps: cosmic ray removal, background subtraction, cropping of the spectral edges affected by detector margins, spectral unmixing with the True Component Analysis tool, and averaging of the mean spectra, summarizing multiple measurements in order to optimize the signal-to-noise ratio. The respective Raman maps are presented as intensity maps with false colours, where the brightest shade corresponds to the highest intensity of the Raman signal of the respective pure component, i.e. the highest concentration of the given substance. The figures were created using Origin Pro 2024.

3. Results

3.1. *In vitro* samples

The first goal of this diploma thesis was to prepare and measure *in vitro* precipitates of barite and celestine. The aqueous solutions of $BaCl_2$ and/or $SrCl_2$ were titrated by Na_2SO_4, HNa_2O_4P, $Na_4O_7P_2$ or $Na_5O_{10}P_3$ depending on the sample series as shown in Tabs. 3-6. These series should serve as reference spectra for the next parts of the thesis and future works. A total of 11 samples, each with varying molar Ba:Sr ratios, were prepared for every series. In each sample, 4-6 precipitated crystals were identified and measured. The resulting Raman spectra are displayed in Figs. 18 - 29 below.

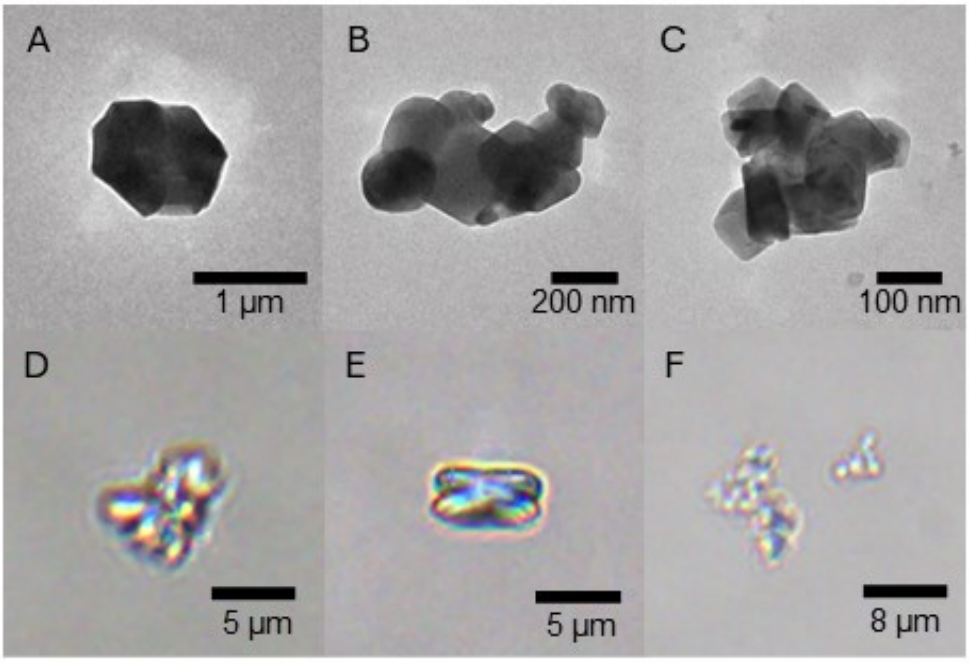

Figure 18: Exemplary images of precipitated barite crystals acquired by TEM (A-C) and optical microscope (D-F).

Sulphate series

To find out how the position of the most intense Raman band corresponding to the symmetric vibration of the sulphate group changes depending on the molar ratio of $BaCl_2$ and $SrCl_2$ in the solution from which the mixed crystal was precipitated by adding Na_2SO_4, we prepared a concentration series with a molar ratio ranging from 0 to 1. In Fig. 19, the respective spectra normalized to their respective maxima are shown. In the individual spectra it can be seen that in the mixed crystals formed this way, only single Raman band is present in the region of 980 - 1010 cm^{-1}. The position of this peak changes practically linearly between the position characteristic for pure $BaSO_4$ (987 cm^{-1}) and pure $SrSO_4$ (1000 cm^{-1}), depending on the molar ratio.

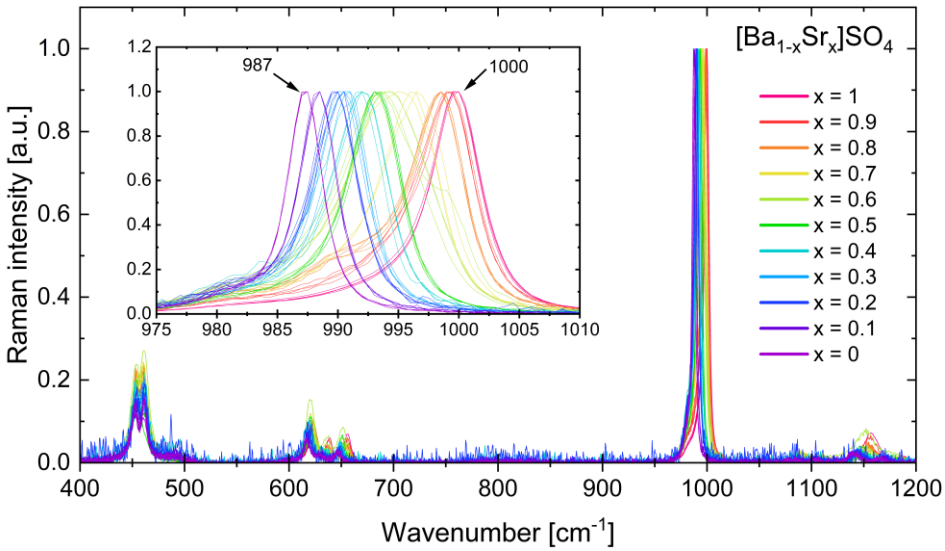

Figure 19: Raman spectra of the sulphate series samples. Different colours were assigned to the samples with different Ba:Sr ratios. Variability in the main peak position is shown in the zoomed inset. For each concentration ratio, the graph shows several spectra measured on different crystals. Spectra belonging to each other are shown in the same colour. All spectra are normalized to the maximum of their most intense band to highlight the shape of the band and its position. Some spectra were obtained with a worse signal-to-noise ratio, therefore after renormalization they show increased background noise.

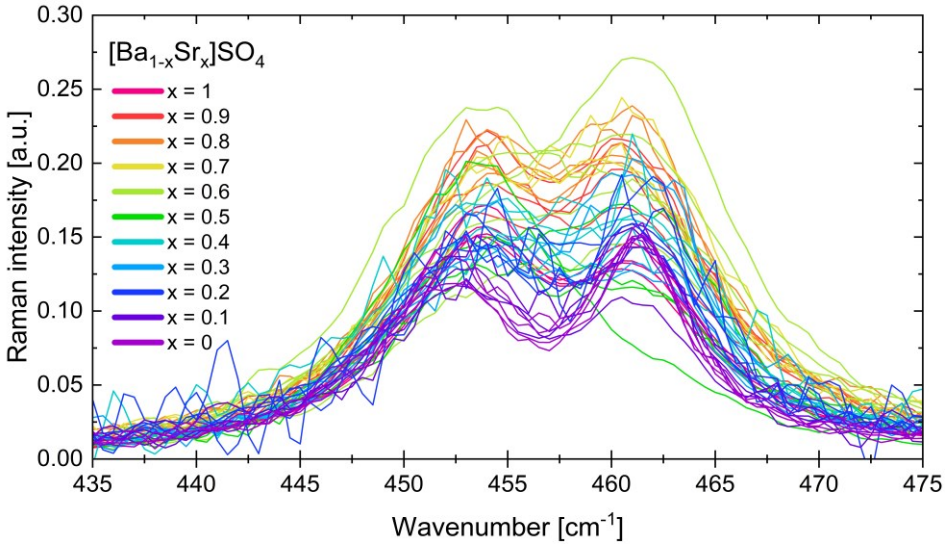

Figure 20: Zoomed part of the Raman spectra for the sulphate series samples at the low-wavenumber spectral region 435-475 cm^{-1} exhibiting no variations in the position concerning Ba:Sr ratio. However, the ratio between the intensity of the individual maxima of the doublet is dependent on the crystal orientation with respect to the polarization of excitation light.

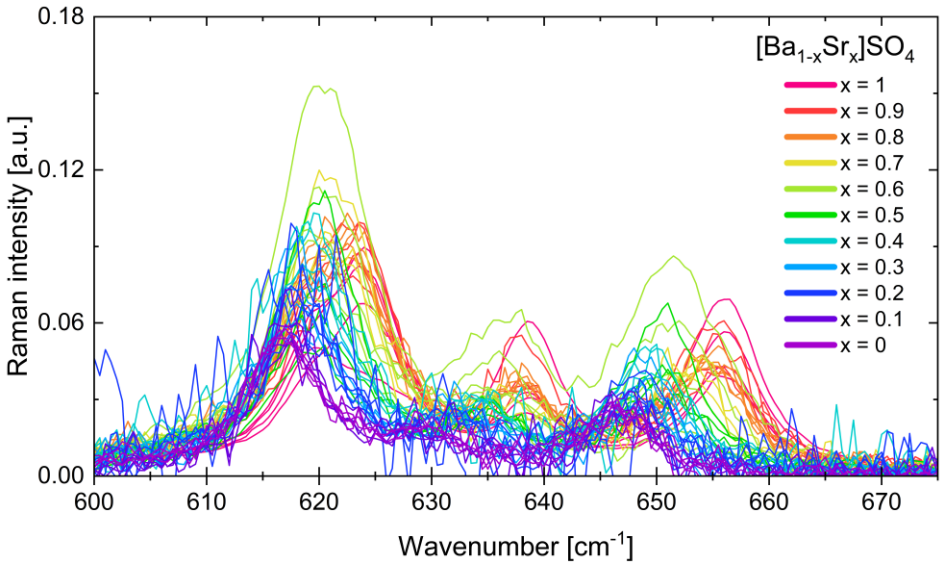

Figure 21: Zoomed part of the Raman spectra for the sulphate series samples at the spectral region 600-675 cm^{-1} exhibiting slight variability in position and ratios between peaks intensity between the samples with different Ba:Sr ratios.

In the Fig. 20 is shown the low-wavelength region of the spectra and its dependence on the Ba:Sr ratio. Comparison the positions of the individual maxima of doublet peak at 453 and 462 cm^{-1} for different molar ratios of Ba:Sr, it is clear that this band

practically does not change its position. Changes in relative intensities probably correspond to different orientations of the crystals with respect to the polarization of the excitation beam.

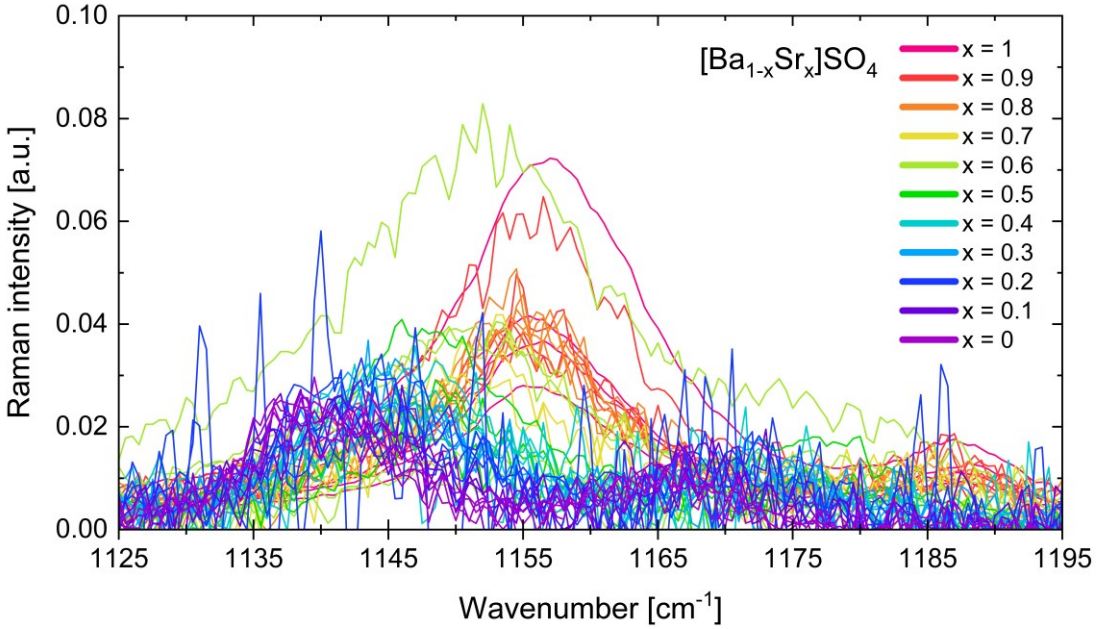

Figure 22: Zoomed part of the Raman spectra for the sulphate series samples at the spectral region 1125-1195 cm^{-1} exhibiting modest variability in position and ratios between peaks intensity between the samples with different Ba:Sr ratios.

Raman bands in the region 600 - 670 cm^{-1} behave similarly, as can be seen in Fig. 21. Even for the bands in the region 1125-1195 cm^{-1}, no clear dependence on the Ba:Sr molar ratio can be traced (Fig. 22). Thus, it appears that the fully symmetric vibration of SO_4 is the most sensitive to the molar ratio of mixed crystals. Its position could serve as a practical indicator and easily obtainable proxy of the molar ratio of Ba and Sr. For this statement to be applicable, it would be necessary to determine by an independent method the actual occurrence of Ba and Sr in crystals precipitated in vitro (*e.g.* by EDX), since, due to the different solubility of $BaSO_4$ and $SrSO_4$, it is not certain that the formed crystals retain the same molar ratio as it is in the solution.

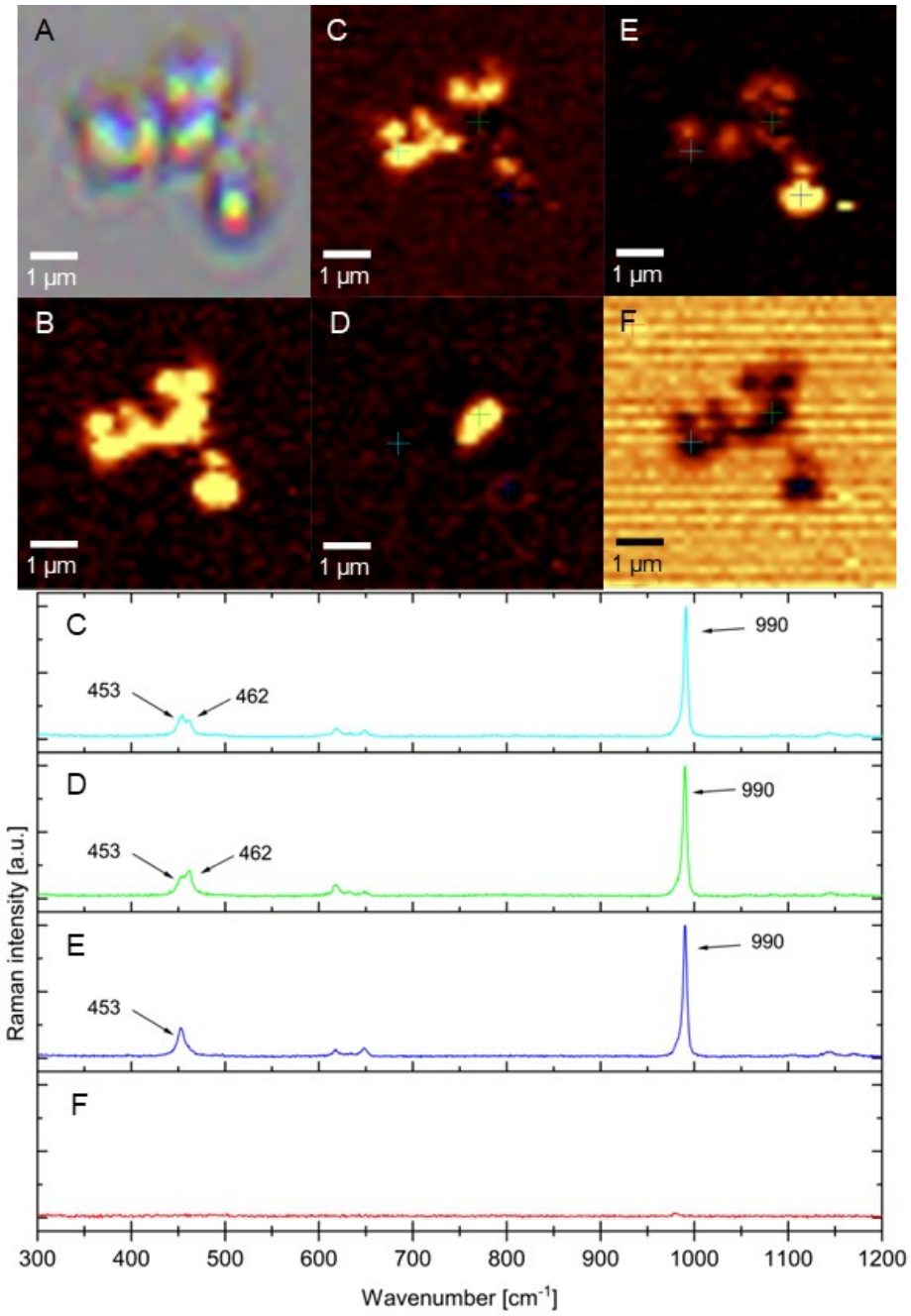

Figure 23: An example of doublet peak intensity ratios dependency on the crystal orientation with respect to the polarization of the excitation light. Image from the optical microscope (A), Raman intensity map for peak at 990 cm^{-1} (B), (C-E) Raman maps for different ratios of doublet peaks intensity and their corresponding spectra, (F) Raman map of background after subtraction (in this case water) and spectrum.

Co-crystals of sulphate series

In the work (Pilátová et al., 2023) it was reported that some diplonemids grown in media containing barium and strontium ions can form both strontiobarite $(Ba,Sr)SO_4$ crystals as well as co-crystals that seem to be conglomerates of pure barite and pure celestine. Some hypotheses explaining the presence of particulate barite in oceans describe its formation as a gradual dissolution of barium-enriched baritocelestine $(Sr,Ba)SO_4$. Baritocelestine would come from the skeletons of marine acanthareans living in the photonic zone. The celestine part of these skeletons would gradually dissolve (due to higher solubility of celestine than that of barite) and the remaining part being gradually enriched with barium ions during long sedimentation on the sea floor. The gradual increase of the barite component could be contributed to the binding of additional barium ions from the surrounding environment, when seed crystals losing strontium ions would serve as condensation cores. In order to clarify the possibility of forming co-crystals on condensation cores, or mixed $(Sr,Ba)SO_4$ crystals, experiments were carried out where microcrystals of pure barite and celestine were transferred to a medium containing only $SrCl_2$ or $BaCl_2$, respectively, and exposed to their action for a long time.

In Fig. 24 it can be seen that barite crystals exposed to $SrCl_2$ solution form an outer barium-enriched celestine layer as indicated by a celestine peak at 999 cm^{-1} while retaining their barite cores practically unchanged in terms of composition given by the presence of the peak at 987 cm^{-1}. Spectral Raman maps corresponding to the microcrystals identified due to their individual spectra shown as well. On the other hand, celestine crystals exposed to the $BaCl_2$ solution were probably dissolved, therefore leaching out part of the strontium ions to the solution and replacing them by barium. Afterwards, the strontium-enriched barite crystals were formed, as shown in Fig. 25. This is further supported by the presence of only a single peak at 988 cm^{-1} and the Raman spectral maps which determine the spatial variability of the sample based on the ratio of the peaks at 452 cm^{-1} and 461 cm^{-1}, not by the variability or presence of other main peaks.

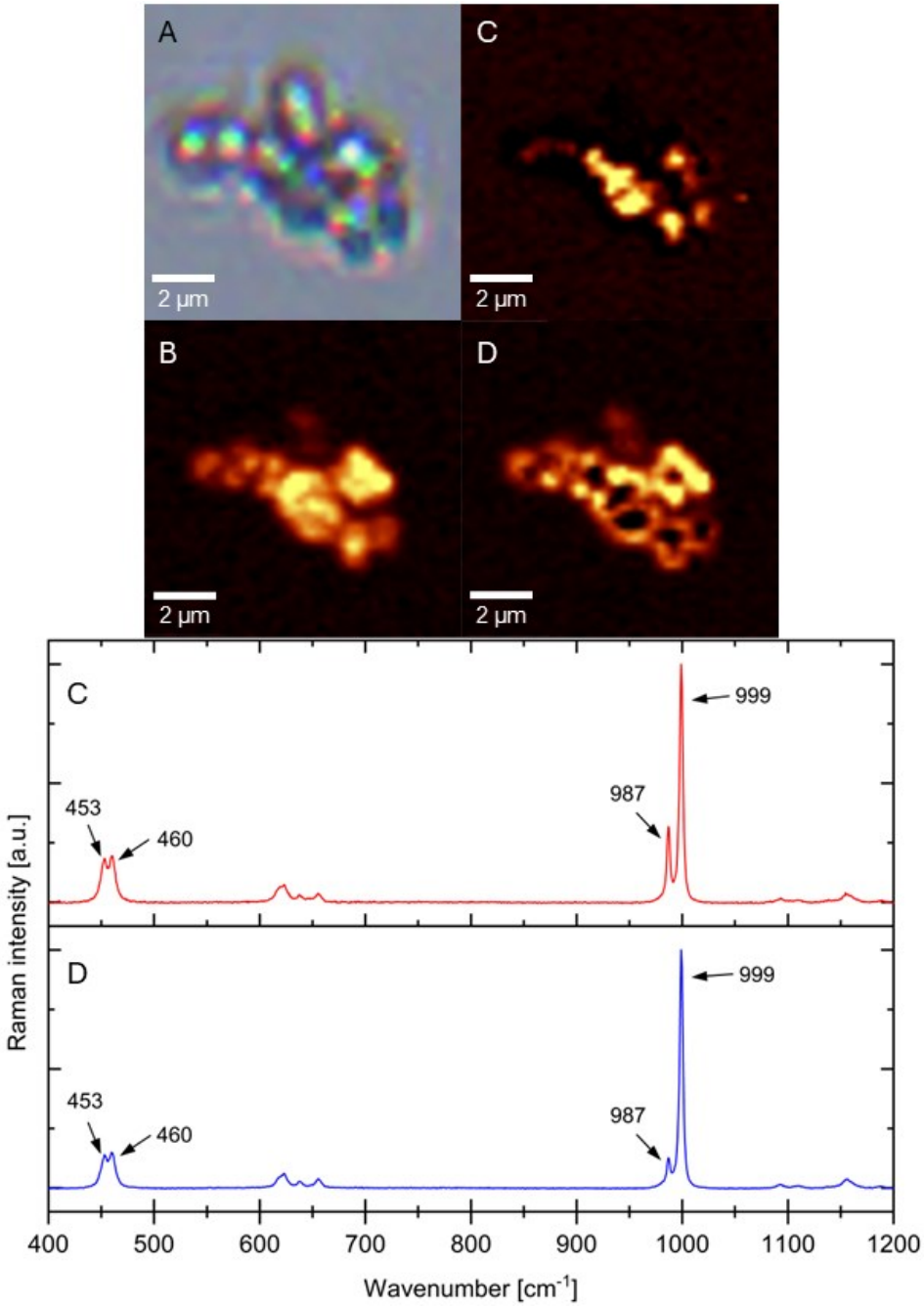

Figure 24: Barite crystals transferred to the $SrCl_2$ solution. Image from the optical microscope (A), Raman intensity map for Raman band of characteristic of pure celestine at 999 cm^{-1} (B), Raman intensity maps for different 987 cm^{-1} and 999 cm^{-1} peak ratios and their spectra corresponding to the spatial distribution of barite and celestine (C, D). Well-differentiated bands of barite (987 cm^{-1}) and celestine (999 cm^{-1}) testify that a layer of pure barite has formed on the surface of celestite.

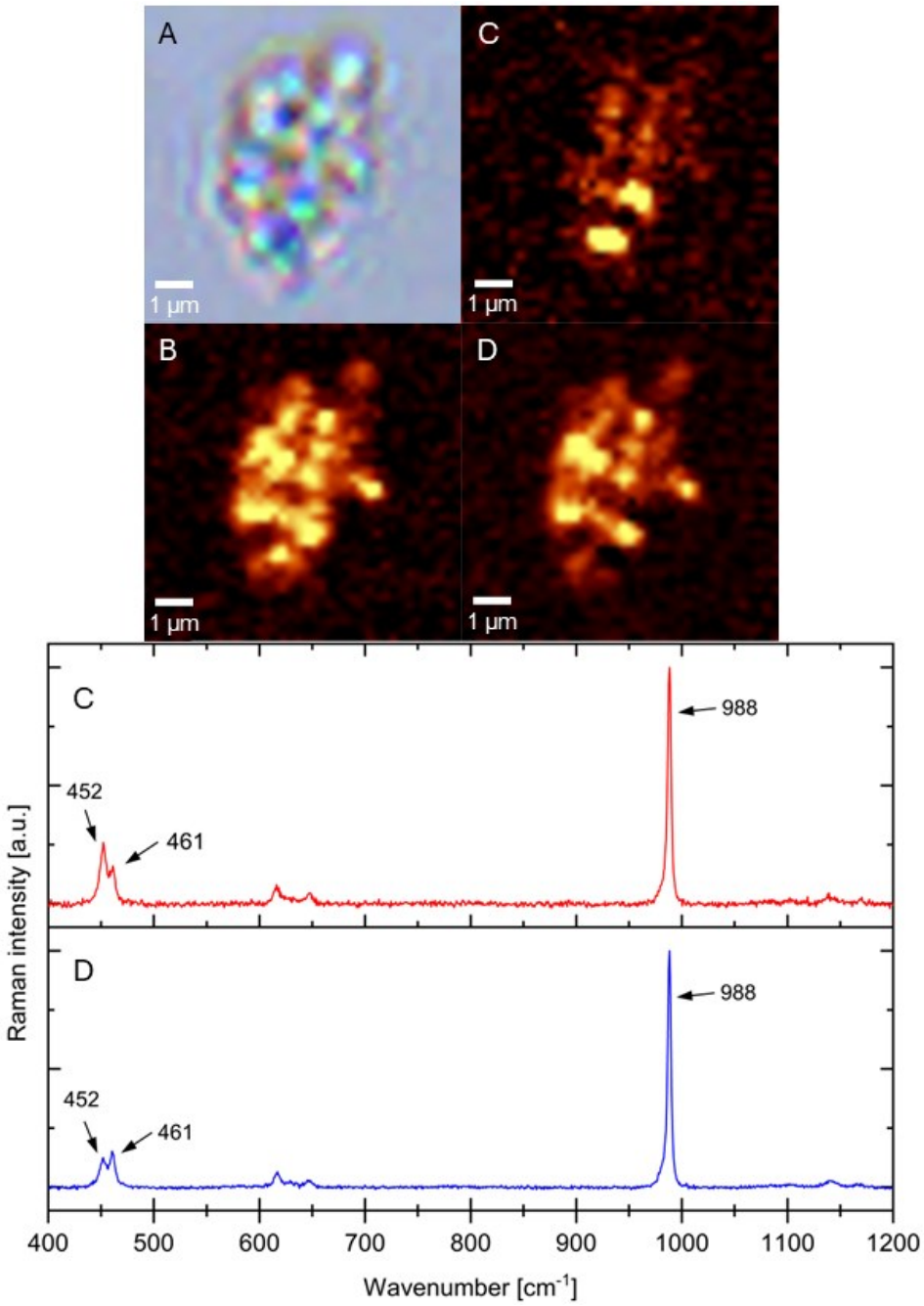

Figure 25: Celestine crystals transferred to the $BaCl_2$ solution. Image from the optical microscope (A), Raman intensity map for barite peak at 988 cm^{-1} (B), Raman intensity maps for different 452 cm^{-1} and 461 cm^{-1} peak ratios and their spectra (C, D).

The above results show that such a process of gradual enrichment of celestine with barium is possible in principle. The question is whether it can also take place in conditions of extremely low barium concentration, such exist in oceans.

Monophosphate series

Similarly to the sulphate series, we prepared the concentration series with a molar ratio of $BaCl_2$ and $SrCl_2$ ranging from 0 to 1 for monophosphate series. The changes in the position of the most intense Raman band corresponding to the totally symmetric vibration of a PO_4 group, eventually some other spectral characteristics were determined based on the molar ratio of the solution from which the crystals precipitated by adding HNa_2O_4P.

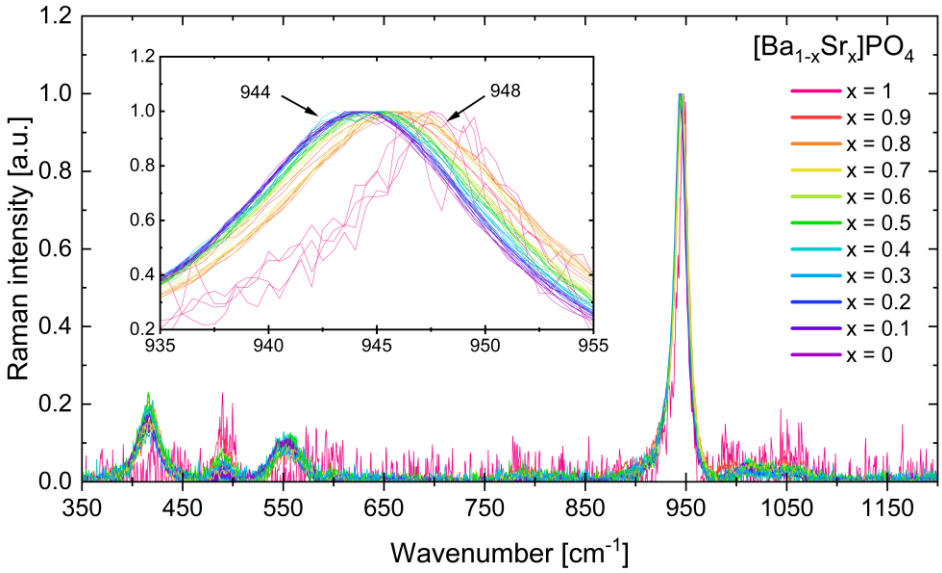

Figure 26: Raman spectra of monophosphate series samples. Different colours were assigned to the samples with different Ba:Sr ratios. Spectra belonging to the same ratio are shown in the same colour. Variability in the main peak position is shown in the zoomed inset.

In the Fig. 26, the respective spectra normalized to the respective maxima are shown. The individual spectra of mixed crystals formed by the precipitation can be seen, only the most intense Raman band is present in the region of 940 - 950 cm^{-1}. Its position, alike the sulphate series, changes slightly (upshift of ca 2 cm^{-1}) but linearly depending on the molar ratio between 944 cm^{-1} for pure $BaPO_4$ and 948 cm^{-1} for pure $SrPO_4$, however only for the ratio between 0 and 0.9. However, the last 2 cm^{-1} upshift to the final position of pure celestine is achieved only in the complete absence of barium ions in the solution. Figs. 27 and 28 show low-wavenumber regions of the spectra and by comparing the positions of peaks in individual spectra can be seen that the position of

these bands seem to be independent on the molar ratio of Ba:Sr in the solution from which the crystals precipitate.

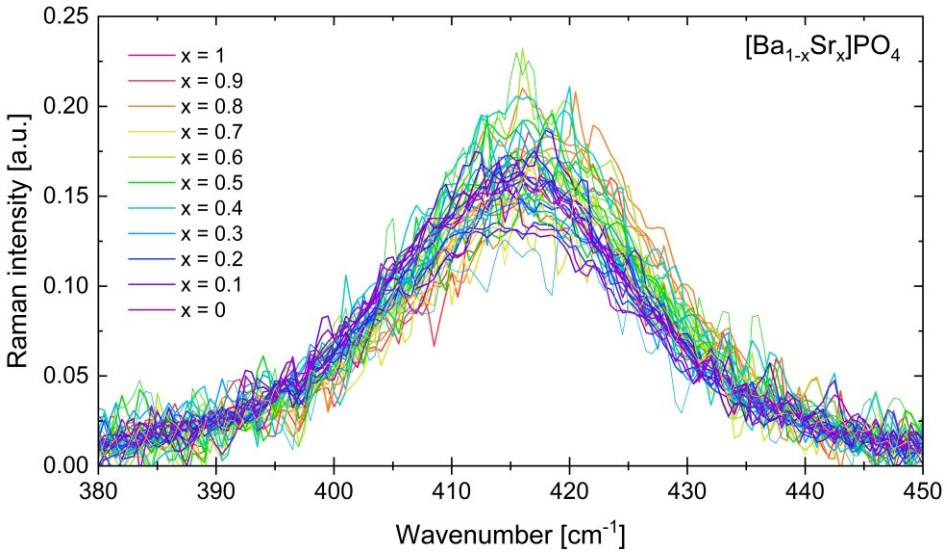

Figure 27: Zoomed part of the Raman spectra for the monophosphate series samples at the spectral region 380-450 cm^{-1} exhibiting no variations in the position and ratios between peaks intensity between the samples with different Ba:Sr ratios.

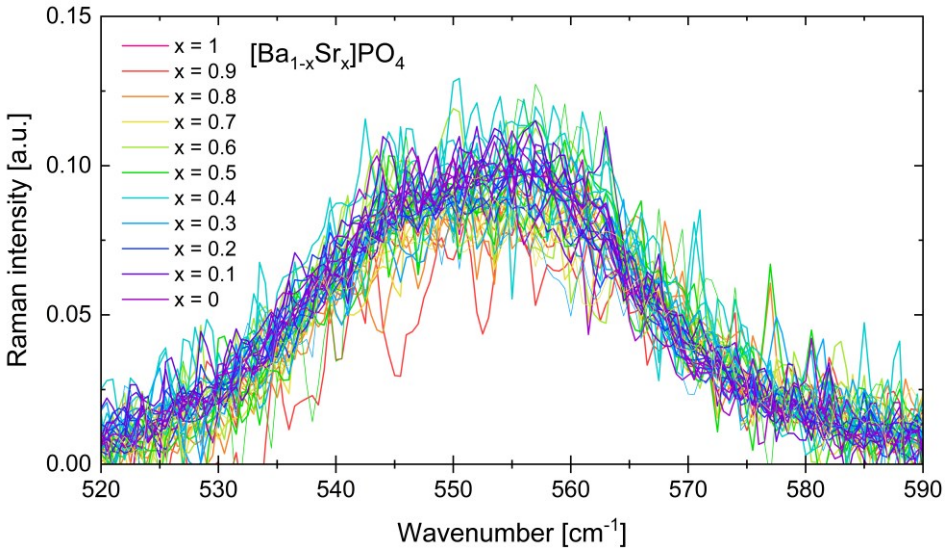

Figure 28: Zoomed part of the Raman spectra for the monophosphate series samples at the spectral region 520-590 cm^{-1} exhibiting no variations in the position and ratios between peaks intensity between the samples with different Ba:Sr ratios.

Diphosphate series

Likewise, to the sulphate and monophosphate series we prepared the diphosphate concentration series with a molar ratio of $BaCl_2$ and $SrCl_2$ ranging from 0 to 1. The changes in position of the most intense Raman band corresponding to the antisymmetric stretching vibration of $HPO_4^{2-}PO_4^{3-}$, and other spectral characteristics were determined based on the molar ratio of the solution from which the crystals precipitated by adding $Na_4O_7P_2$.

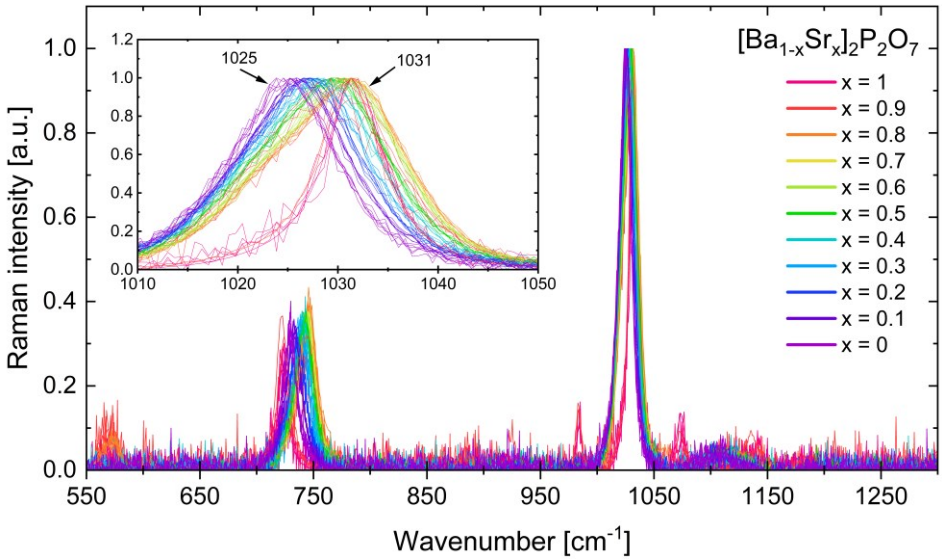

Figure 29: Raman spectra of diphosphate series samples. Different colours were assigned to the samples with different Ba:Sr ratios. Variability in the main peak position is shown in the zoomed part.

In the Fig.29, the respective spectra normalized to the respective maxima are shown. However, as can be seen from the position and the shape of the Raman band in the region 1020 - 1040 cm^{-1}, with increasing Ba:Sr molar ratio the band is shifted from 1025 cm^{-1} for pure $Ba_2P_2O_7$ and 1031 cm^{-1} for pure $Sr_2P_2O_7$, however, its asymmetric broadening occurs up to a ratio of 0.9 when the band suddenly narrows again for the diphosphate complex containing only Sr. The asymmetric shape and step change probably indicate that complex is formed preferentially with Ba than with Sr. It seems that the affinity of the diphosphate for Ba is greater than for Sr, and that this affinity is increasing with the number of phosphate groups in the chain. Fig. 30 shows an intriguing phenomenon in the spectral region of 710 - 770 cm^{-1}. Based on the Ba:Sr molar ratio the first two peaks' maxima (from lower Raman shifts to the higher)

correspond to the pure $Sr_2P_2O_7$ and pure $Ba_2P_2O_4$ respectively, the next peaks correspond to the compounds whose composition gradually decreases in Ba and increases in Sr.

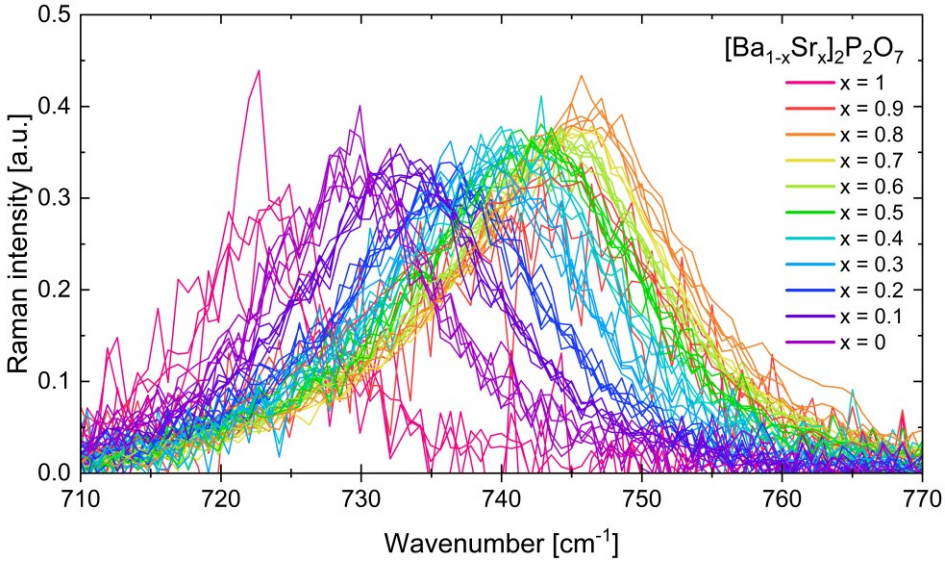

Figure 30: Zoomed part of the Raman spectra for the diphosphate series samples at the spectral region 710-770 cm^{-1}. Similarly, as the main peak, this peak's position changes with different Ba:Sr ratios.

Triphosphate series

The last series we prepared, was a triphosphate concentration series with a molar ratio of $BaCl_2$ and $SrCl_2$ ranging from 0 to 1. The changes in position of the most intense Raman band corresponding to the antisymmetric stretching vibration of HPO_4^{2-}–PO_4^{3-}, and spectral characteristics of the second most intense band were determined based on the molar ratio of the solution from which the crystals precipitated by adding $Na_5O_{10}P_3$.

In Fig. 31, the respective spectra normalized to the respective maxima are shown. The individual spectra of formed mixed crystals can be seen, only the most intense Raman band is present in the region of 1010 - 1070 cm^{-1}. Its position, alike previous series of mono and di-phosphates, changes slightly and linearly depending on the molar ratio between 1027 cm^{-1} for pure $Ba_3P_3O_{10}$ to 1061 cm^{-1} for pure $Sr_3P_3O_{10}$., with the sudden unexplained shift from 1032 cm^{-1} to 1059 cm^{-1}. Fig. 31 shows the same phenomenon in the spectral region of 720 - 770 cm^{-1}.

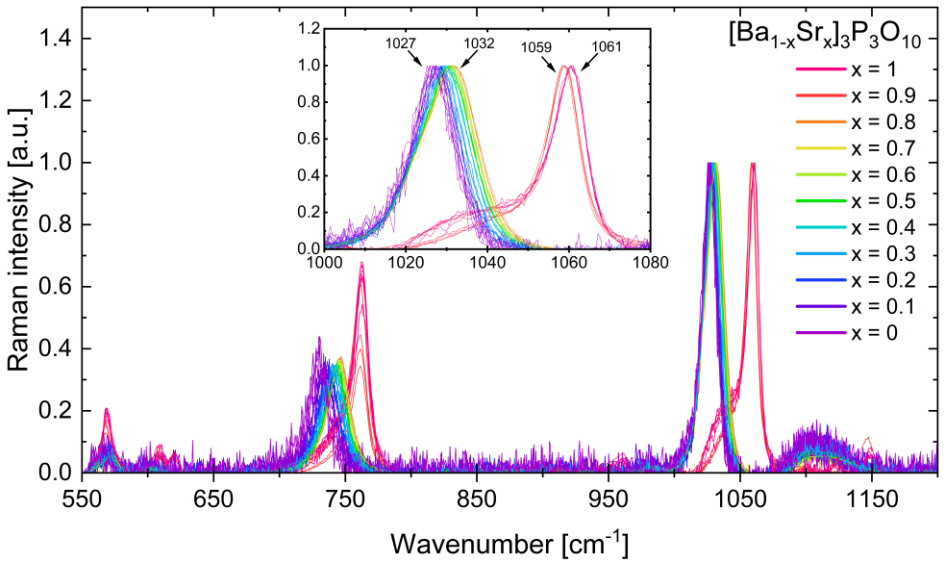

Figure 31: Raman spectra of triphosphate series samples. Different colours were assigned to the samples with different Ba:Sr ratios. Variability in the main peak position is shown in the zoomed part.

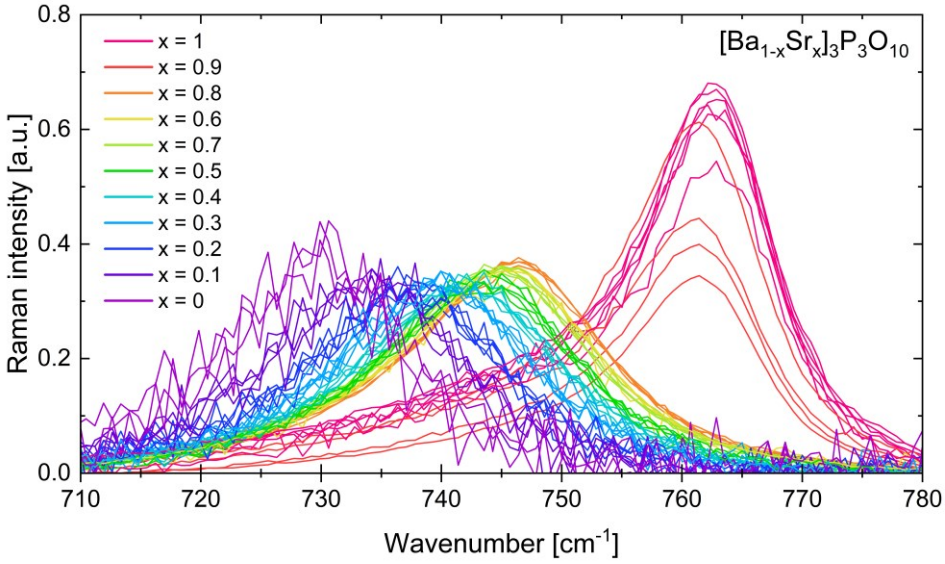

Figure 32: Zoomed part of the Raman spectra for the triphosphate series samples at the spectral region 730-780 cm^{-1}. Similarly, as the main peak, this peak's position changes with different Ba:Sr ratios.

3.2. BaF_2 samples

The cornerstone of the EPS hypothesis for barite formation is the presence of a phosphate groups-containing matrix that acts as a pre-concentrator of Ba ions. Once barium ions reach sufficient concentrations and interact with the abundant sulphate in the seawater environment, barite formation can occur.

In this experiment, we tried to reverse the roles of the matrix and the solution. The BaF_2 crystal should act as a solid matrix to bind the phosphate groups in the solution to the surface. The sulphate with a higher affinity to the barium ions should be able to substitute the phosphate to form the barite layer at the surface of the BaF_2.

Solutions of HNa_2O_4P, $Na_4O_7P_2$, $Na_5O_{10}P_3$, $Na_6[(PO_3)_6]$ or phytic acid were used as model substances for a medium containing phosphate groups.

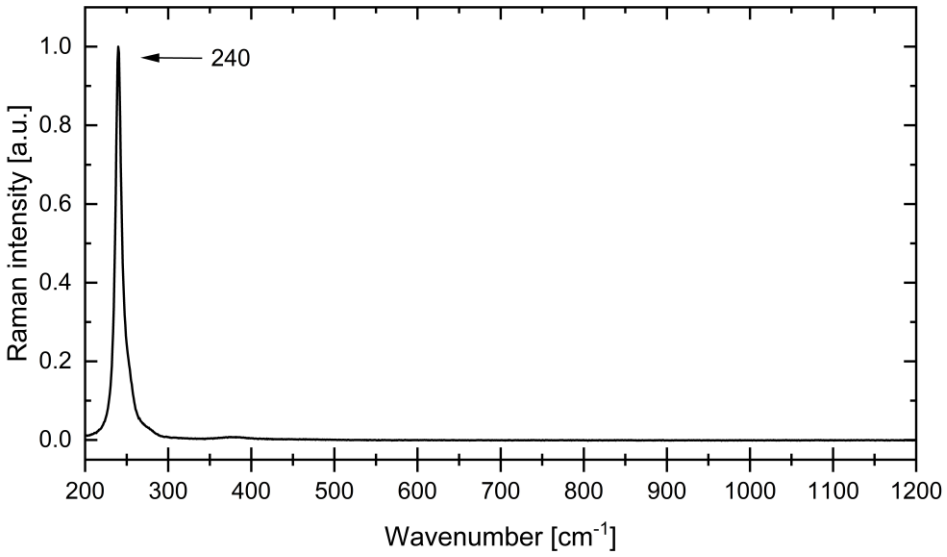

Figure 33: Raman spectrum of pure BaF_2 crystal. Solid BaF_2 exhibits only one strong Raman band at 240 cm^{-1}.

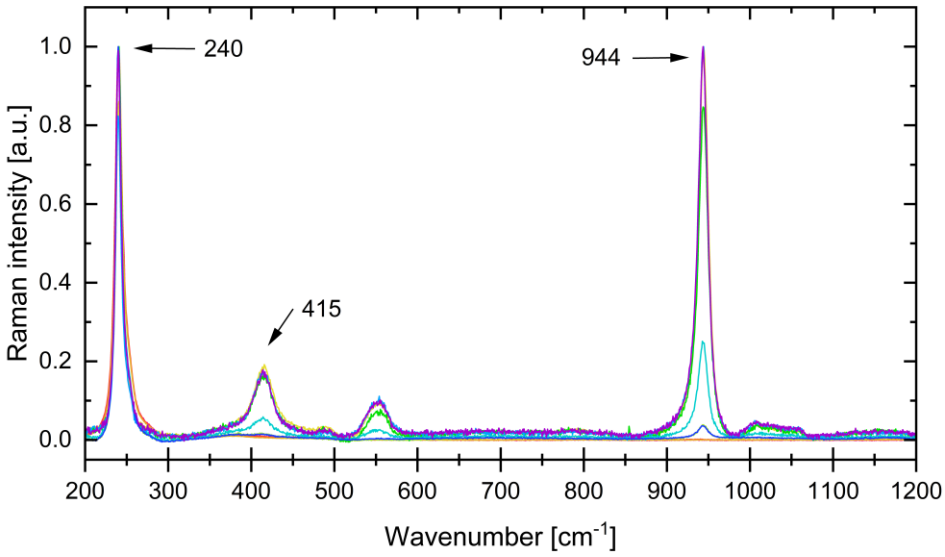

Figure 34: Raman spectra of BaF_2 after 24 hours in HNa_2O_4P solution. The presence of a peak at 944 cm^{-1} suggests that the phosphate group was bound to the surface of BaF_2 crystal and formed $BaPO_4$.

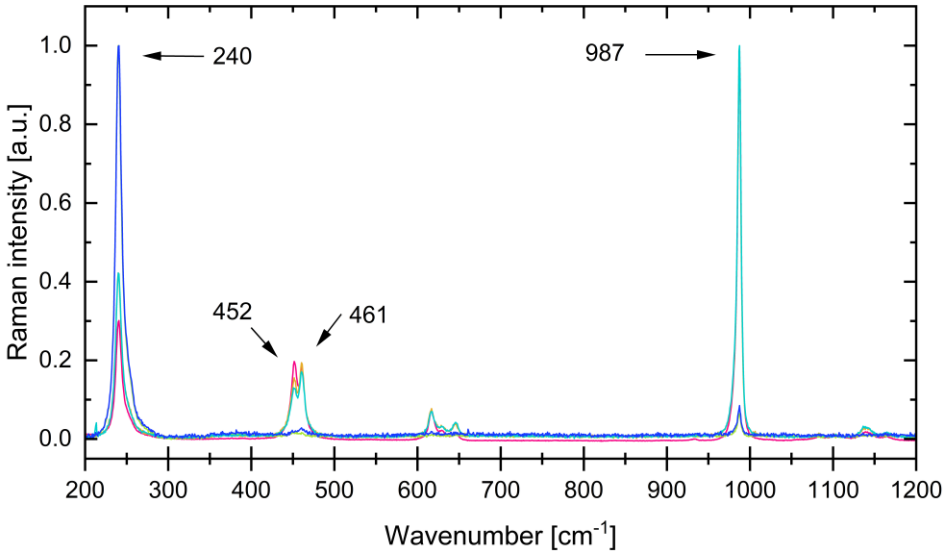

Figure 35: Raman spectra of BaF_2 pre-treated by incubation in the HNa_2O_4P solution after 24 hours in Na_2SO_4 solution. The absence of a peak at 944 cm^{-1} and the presence of a peak at 987 cm^{-1} suggests that phosphate bound to the surface of BaF_2 was substituted by sulphate and a barite layer at the surface was formed.

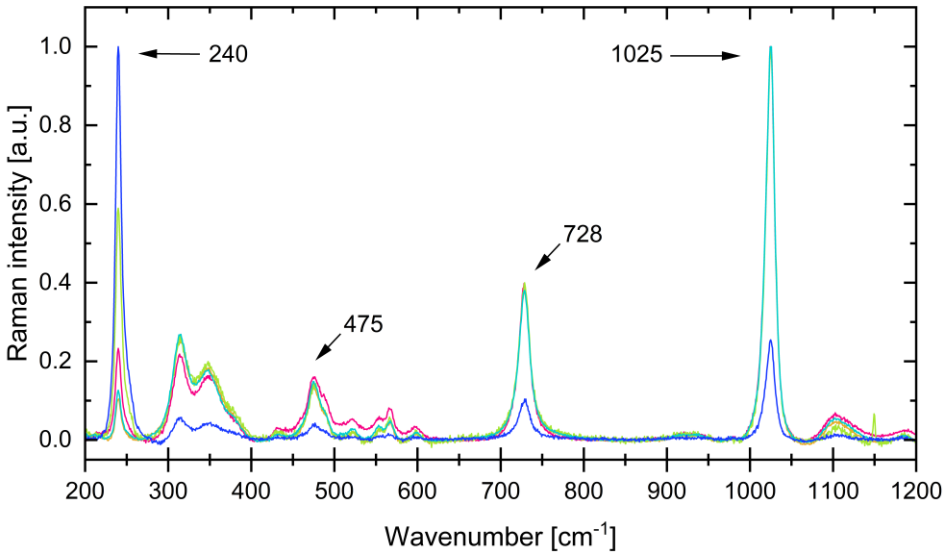

Figure 36: Raman spectra of BaF_2 after 24 hours in $Na_4O_7P_2$ solution. The presence of a peak at 1025 cm^{-1} suggests that the diphosphate group was bound to the surface of BaF_2 crystal and formed $Ba_2P_2O_7$.

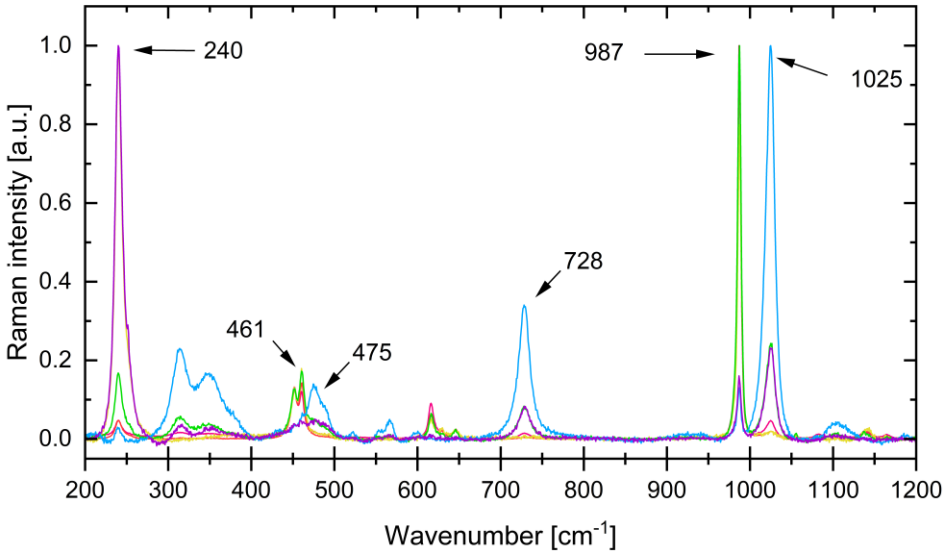

Figure 37: Raman spectra of BaF_2 pre-treated by incubation in the $Na_4O_7P_2$ solution after 24 hours in Na_2SO_4 solution. The presence of peaks at 987 cm^{-1} and 1025 cm^{-1} suggests that diphosphate bound to the surface of BaF_2 was partially substituted by sulphate and domains of barite and $Ba_2P_2O_7$ were formed.

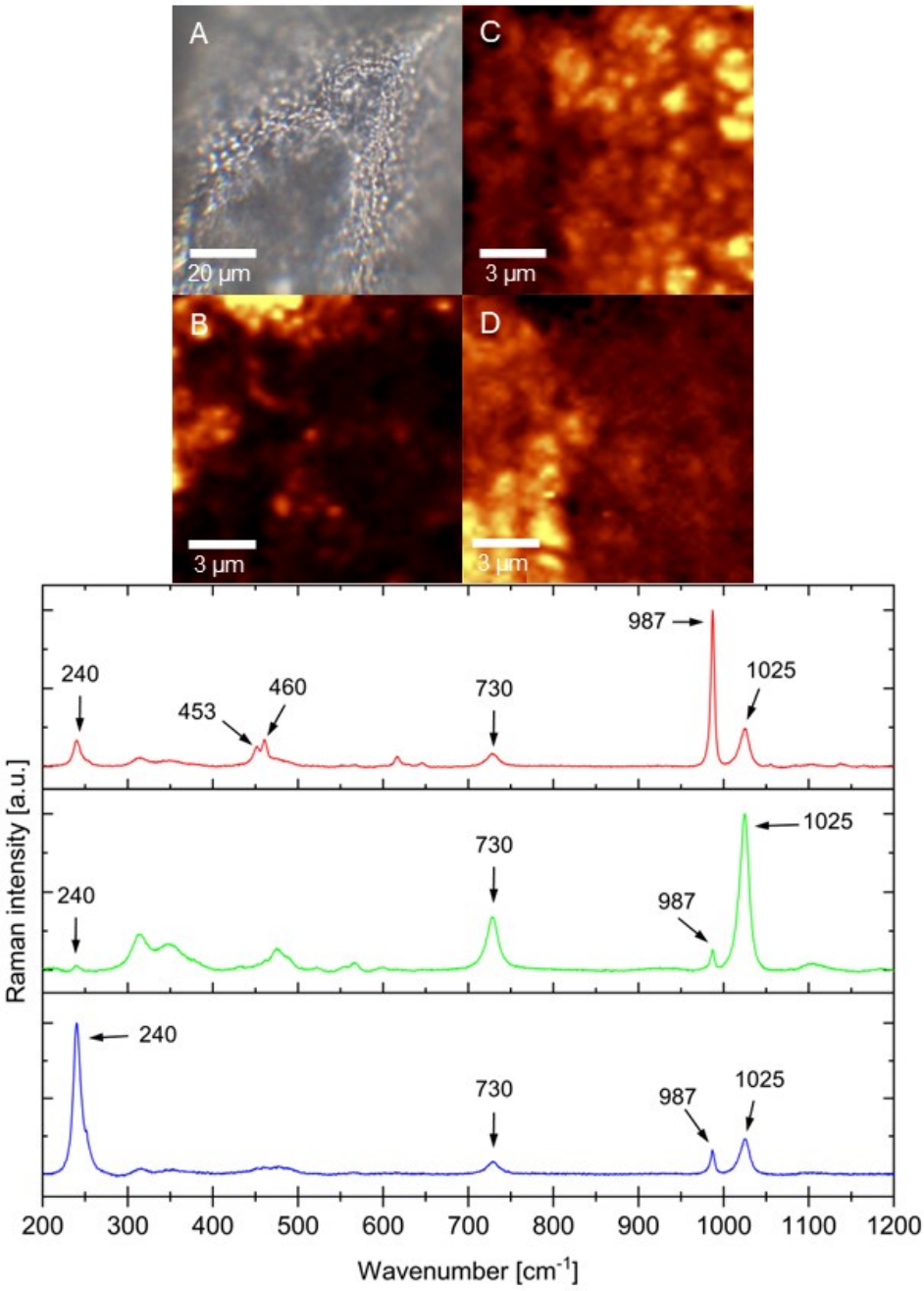

Figure 38: Raman spectra of BaF_2 pre-treated by incubation in the $Na_4O_7P_2$ solution after 24 hours in Na_2SO_4 solution and its spectral components illustrating spatial distribution of barite and $Ba_2P_2O_7$ domains. All spectra are normalized to the maximum of their most intense band. Image from the optical microscope (A), Raman intensity map for barite peak at 987 cm^{-1}, Raman intensity map for diphosphate peak at 1025 cm^{-1} (C) and Raman intensity map for BaF_2 peak at 240 cm^{-1} (D).

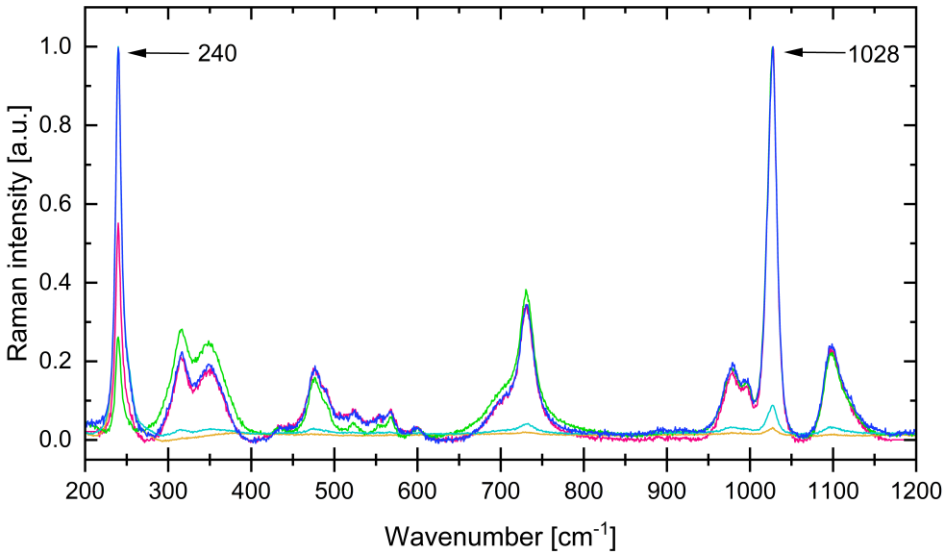

Figure 39: Raman spectra of BaF_2 after 24 hours in $Na_5O_{10}P_3$ solution. The presence of a peak at 1028 cm^{-1} suggests that the triphosphate group was bound to the surface of BaF_2 crystal and formed BaP_3O_{10}.

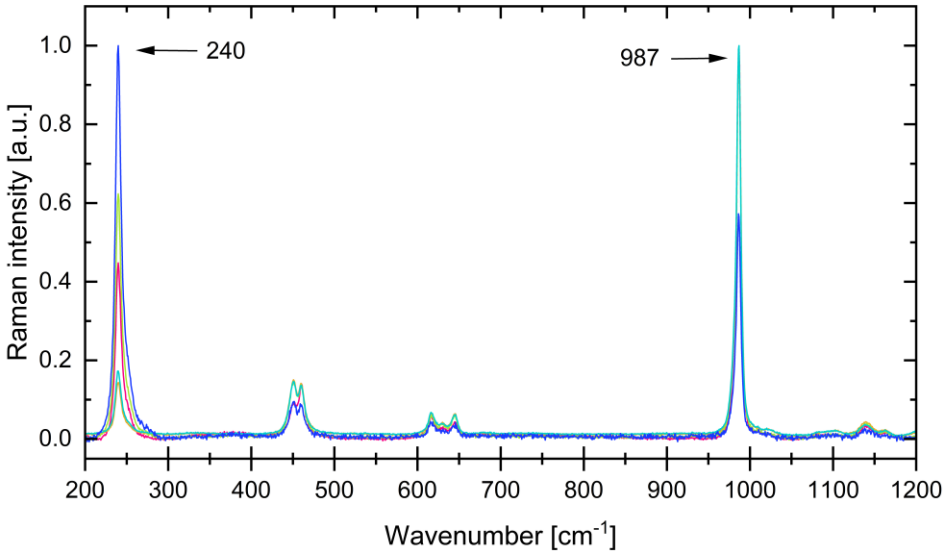

Figure 40: Raman spectra of BaF_2 pre-treated by incubation in the $Na_5O_{10}P_3$ solution after 24 hours in Na_2SO_4 solution. The absence of a peak at 1028 cm^{-1} and the presence of a peak at 987 cm^{-1} suggests that the triphosphate group bound to the surface of BaF_2 was fully substituted by sulphate and the barite layer at the surface was formed.

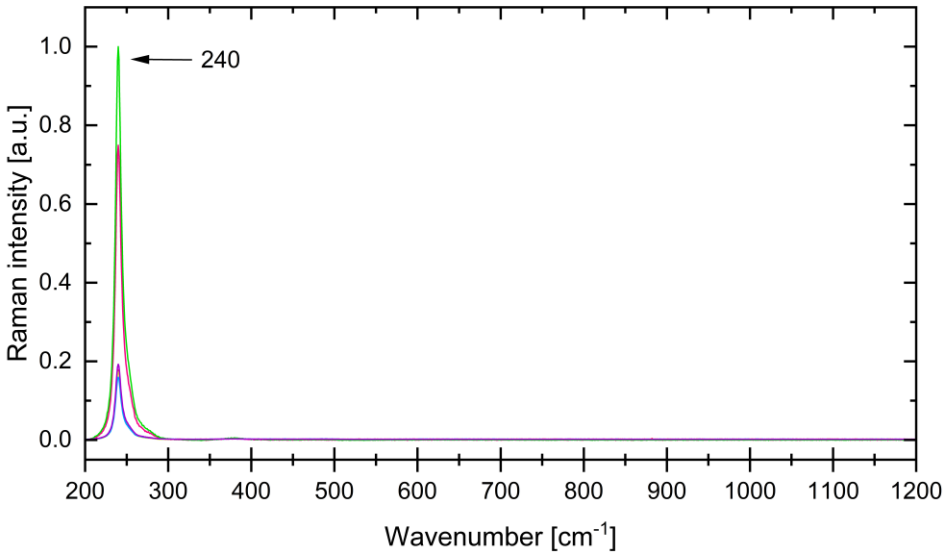

Figure 41: Raman spectra of BaF_2 after 24 hours in $Na_6[(PO_3)_6]$ solution. The complete absence of other peaks, except the peak at 240 cm^{-1} corresponding to the BaF_2 suggests that hexametaphosphate was not bound to the surface of BaF_2 crystal.

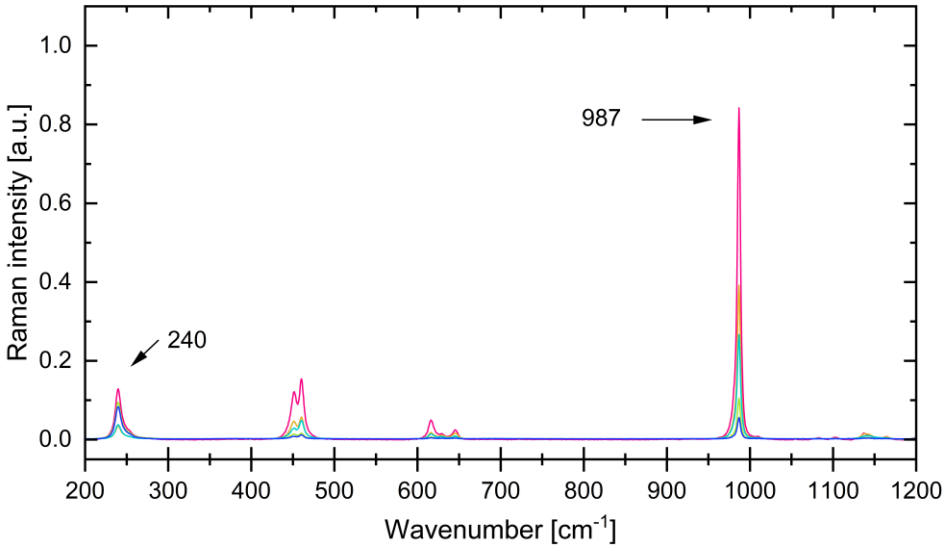

Figure 42: Raman spectra of BaF_2 pre-treated by incubation in the $Na_6[(PO_3)_6]$ solution after 24 hours in Na_2SO_4 solution. The presence of a peak at 987 cm^{-1} suggests barite formation.

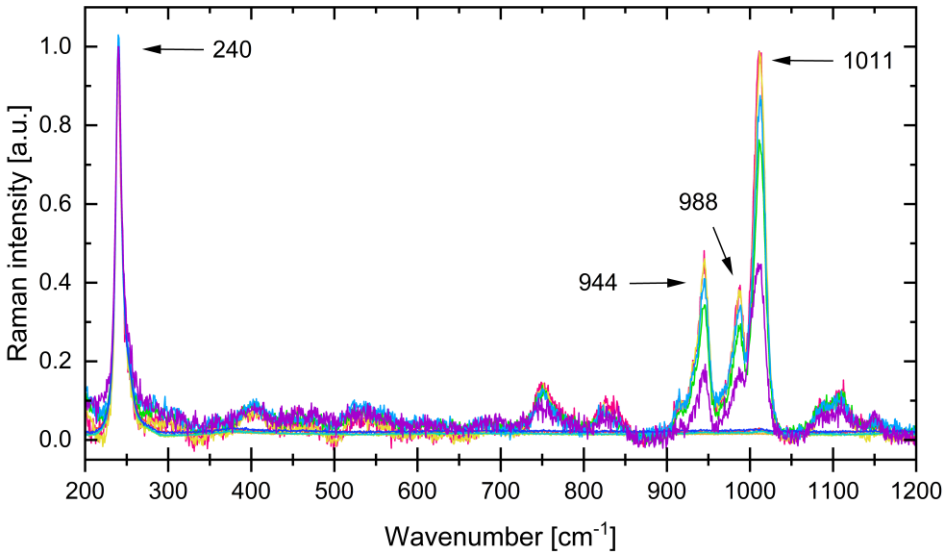

Figure 43: Raman spectra of BaF_2 after 24 hours in phytic acid solution. The peaks at 944 cm^{-1}, 988 cm^{-1} and 1011 cm^{-1} suggest the presence of phytic acid.

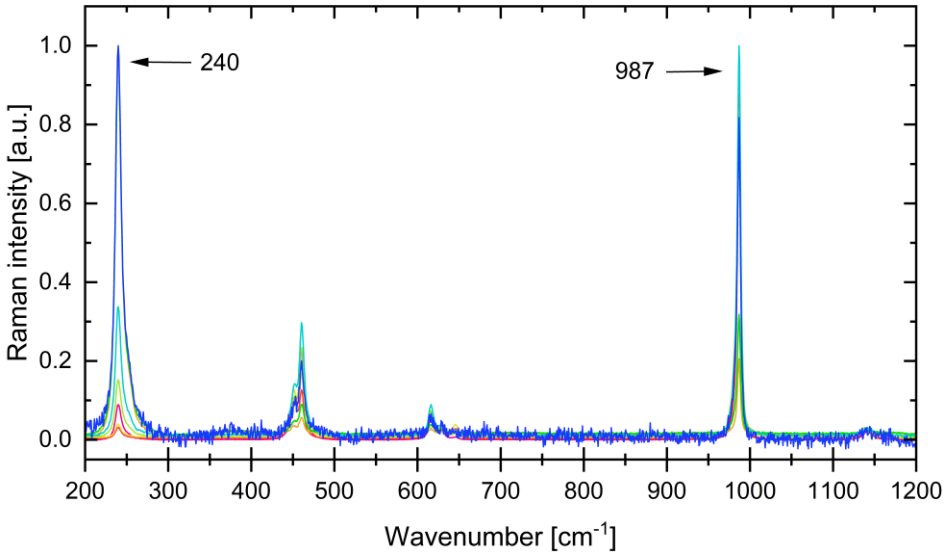

Figure 44: Raman spectra of BaF_2 pre-treated by incubation in the phytic acid solution after 24 hours in Na_2SO_4 solution. The presence of a peak at 987 cm^{-1} suggests barite formation.

As indicated in the corresponding pair of Figures (*e.g.* 34 and 35 for HNa_2O_4P·and Na_2SO_4·solutions). The PO_4-containing solutions were successfully bound to the surface of BaF_2, with the exception of $Na_6[(PO_3)_6]$. Consequently, fully substituted by sulphate with its higher affinity to the Ba, to form a barite layer on the surface as confirmed by the measurements. An interesting phenomenon occurred in the case of $Na_4O_7P_2$, where the diphosphate groups were successfully bound to the surface,

however only partially substituted by sulphate groups. The evidence suggests the formation of barite and $Ba_2P_2O_7$ domains on the surface of BaF_2 as shown in Fig. 38. If the diphosphate is able to withstand the substitution by sulphate this could potentially explain the spatial separation of SO_4 from the barium pre-concentrated by EPS in marine environment.

3.3. DNA-agarose sheets

The main goal of this experiment was to determine if the EPS can mediate barite formation and if the phosphate groups of EPS can act as a pre-concentrator for barium ions. As known, DNA is a polyanionic polymer containing a large number of phosphate groups oriented outside the double helix. Since high-molecular-weight DNA incorporated into the agarose matrix will not be released into the surrounding solution, it can be used as a simplified model of EPS. The measurements depicted in the Figs. 46 and 47 of this section were performed while some troubles with the CCD detector were being experienced, therefore the irremovable periodic signal in the spectra is present. Although these spectra were measured in the full spectral range (in the so-called panoramic mode with a grating of 600 grooves/mm to also capture the region of stretching vibrations of CH groups and water), all subsequent spectra will be shown only in the characteristic region covering the bands of barite and celestine.

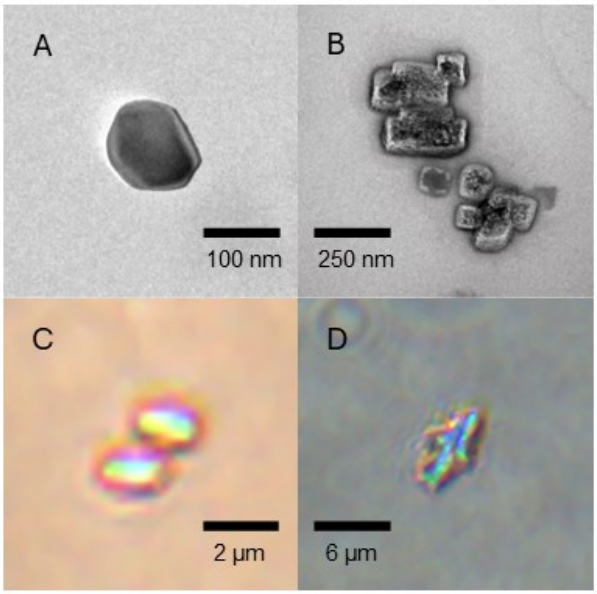

Figure 45: Exemplary images of barite crystals formed in the DNA-agarose sheet acquired by TEM (A, B) and optical microscope (C, D).

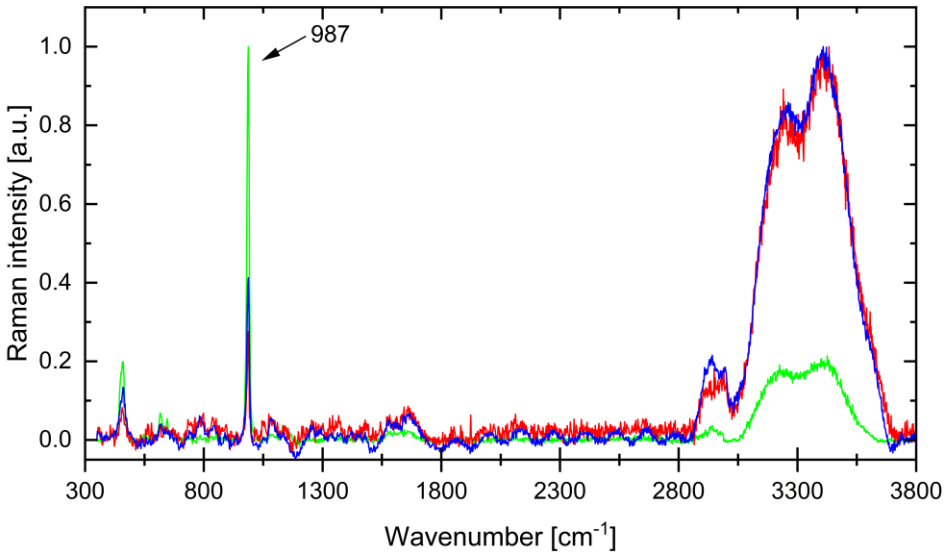

Figure 46: Raman spectra of DNA-agarose sheet after exposure to $BaCl_2$ solution. The peak at 987 cm^{-1} suggests the formation of barite crystals. Spectra are normalized to their respective maxima. The periodic signal forming the background of the spectra was caused by a defect in the CCD detector.

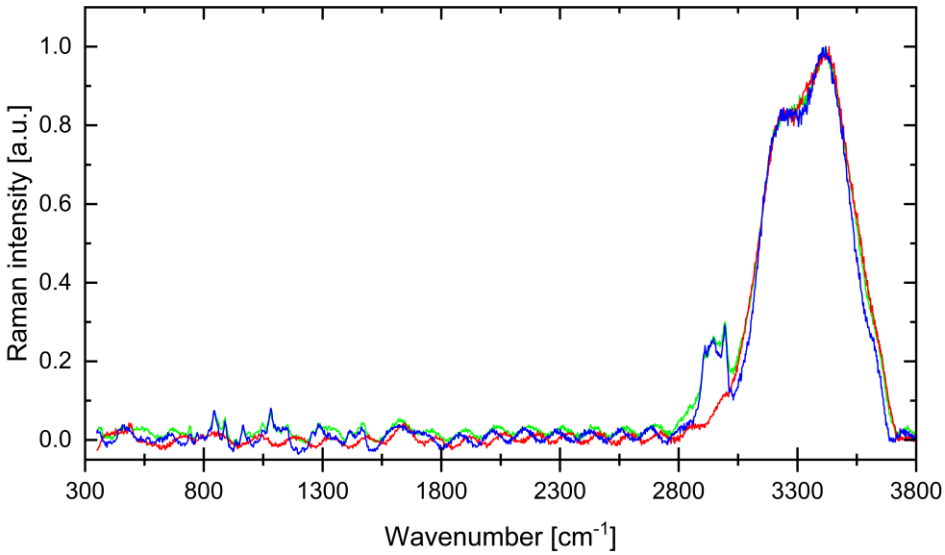

Figure 47: Raman spectra of pure agarose sheet (containing no DNA) after exposure to $BaCl_2$ solution. No evidence of barite crystals is present. The spectra show Raman bands of CH stretching vibrations (around 2800 cm^{-1}) belonging to agarose and stretching bands of water (around 3400 cm^{-1}).

From the Figs. 46 and 47 it can be seen that just the presence of DNA in the agarose sheet was enough to mediate the formation of barite crystals after exposure to $BaCl_2$ even without exposure to the Na_2SO_4 solution. This phenomenon could be explained

by small residual amounts of SO_4 in the agarose (up to 0.1% of dry weight according to the manufacturer) and binding of Ba to the phosphate groups of the DNA, therefore effectively pre-concentrating Ba ions. Consequently, this simplified model of EPS can be used as a reasonable approximation of real EPS systems.

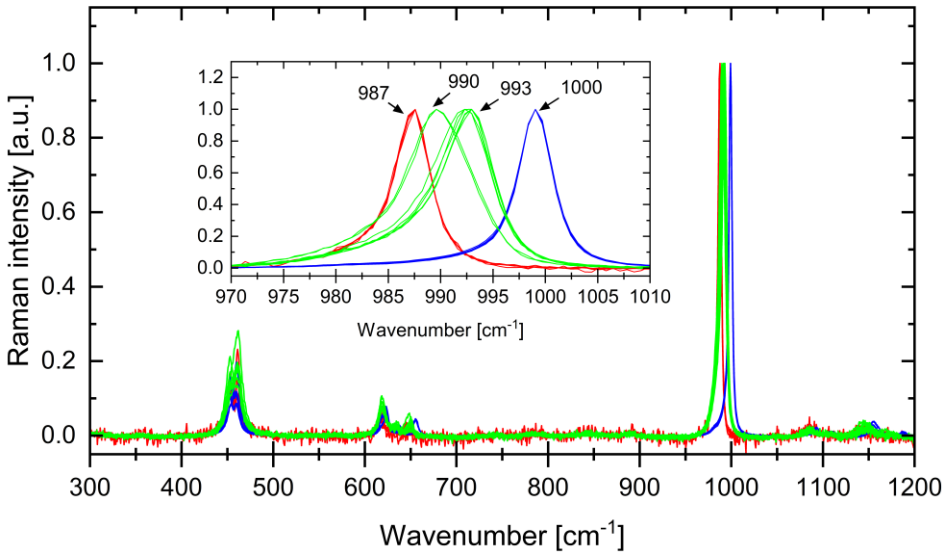

Figure 48: Raman spectra of DNA-agarose sheet after exposure to $BaCl_2$ solution (red), $SrCl_2$ solution (blue) or equimolar $BaCl_2$ and $SrCl_2$ solution (green), a thorough washing in distilled water and subsequent exposure to Na_2SO_4 solution. The peaks at the 987 cm^{-1}, 990 cm^{-1}, 993 cm^{-1} and 1000 cm^{-1} suggest the formation of barite, strontium-enriched barite and celestine crystals, respectively.

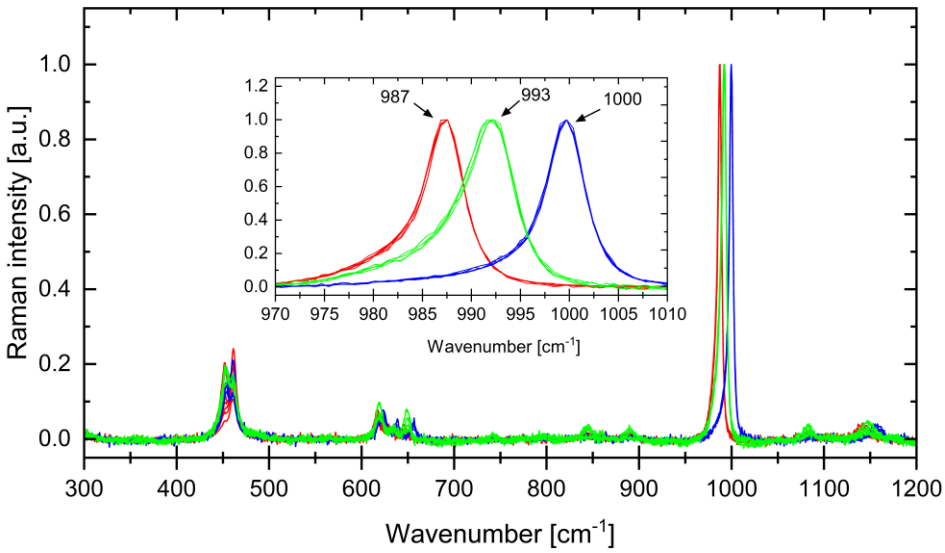

Figure 49: Raman spectra of pure agarose sheet after exposure to $BaCl_2$ solution (red), $SrCl_2$ solution (blue) or equimolar $BaCl_2$ and $SrCl_2$ solution (green), a thorough

washing in distilled water and subsequent exposure to Na_2SO_4 solution. The peaks at 987 cm^{-1}, 993 cm^{-1} and 1000 cm^{-1} suggest the formation of barite, strontium-enriched barite and celestine crystals, respectively.

To further test the functionality of our model system for EPS, the DNA-agarose and pure agarose sheets were exposed to a solution of $BaCl_2$, a solution of $SrCl_2$ or an equimolar solution of $BaCl_2$ and $SrCl_2$. Afterwards thoroughly washed in distilled water and finally exposed to the Na_2SO_4 solution and measured. Obtained spectra are shown in the Figs. 48 and 49. The position of the main peak maxima for the individual solution ($BaCl_2$, $SrCl_2$ or equimolar $BaCl_2$ and $SrCl_2$) are well correlated with the reference spectra in Fig. 19. However, possible preference for Ba can be present in the DNA-agarose sheets as depicted by the peak maxima at 990 cm^{-1}.

As the final experiment using agarose sheets, the dilution series of $BaCl_2$ was performed. From the initial concentration of 50 mM to the final 5 μM solution of $BaCl_2$ was used as media from which the DNA-agarose sheets should potentially "pull out" the Ba ions as opposed to the pure agarose sheets. Results in the form of brightfield images from the optical microscope and Raman intensity maps are shown in Fig. 50. The obtained spectra from individual measurements are shown in the Supp. Fig. 1-8. For the corresponding pair of DNA and pure agarose sheet for the given concentration, it can be seen that the amount and dimensions of the formed crystals are larger for the DNA-agarose sheet. However, for the first pair (A, B) and (C, D) the concentration of $BaCl_2$ of 50 mM was used, which could explain the conspicuous amounts of crystals formed in both cases.

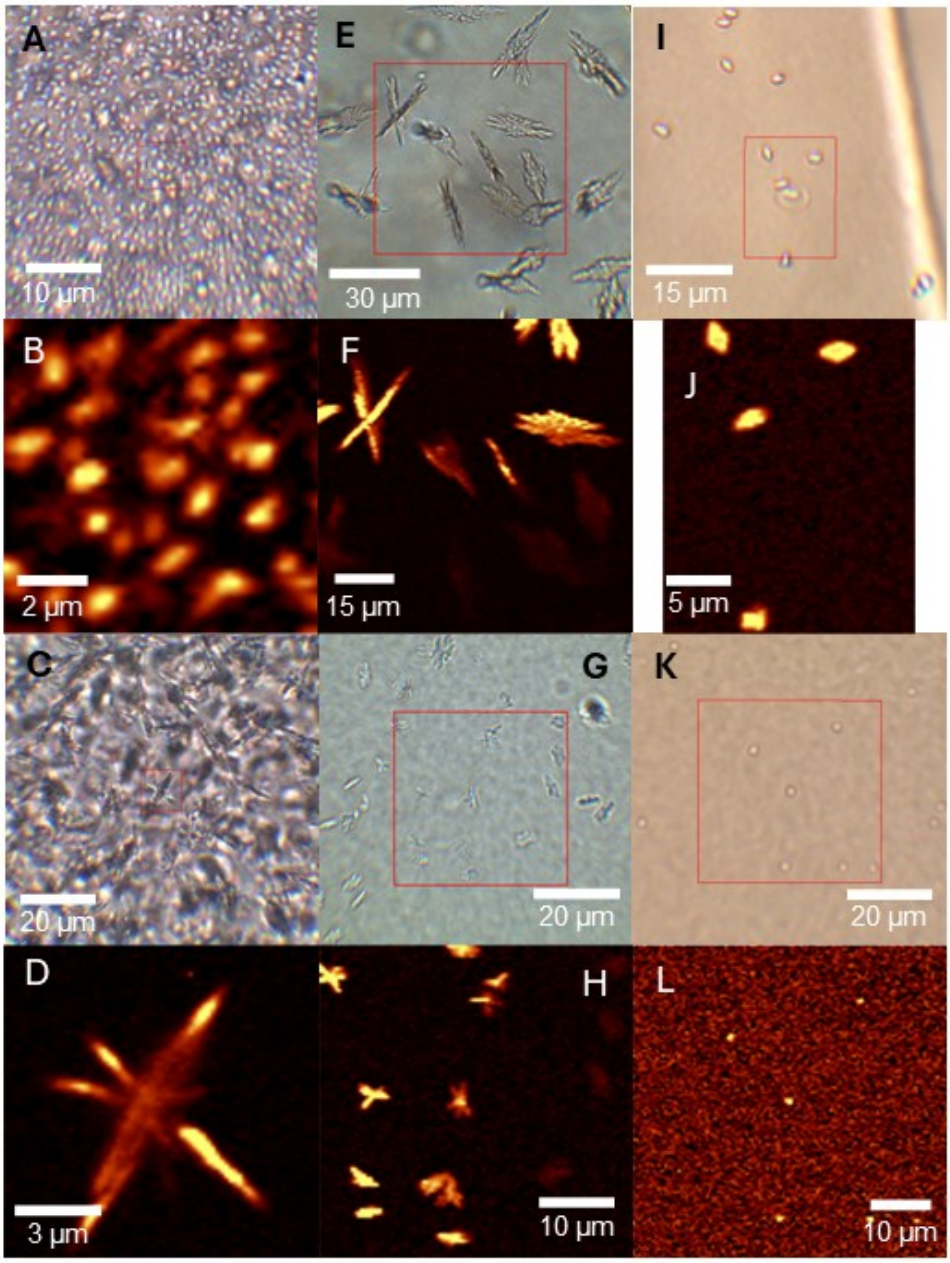

Figure 50: Images from the optical microscope and Raman maps for the peak at 987cm^{-1} of DNA-agarose (A, B; E, F; I, J) and pure agarose sheets (C, D; G, H; K, L) after exposure to $BaCl_2$ solution (50 mM; 500 µM; 5 µM), a thorough washing in distilled water and subsequent exposure to Na_2SO_4 solution.

3.4. Algal Cultures

Both algal cultures were measured 1, 3, and 7 days after the addition of $BaCl_2$ or $SrCl_2$ to the cell culture flasks. The entire experiment was performed twice due to unexpected results obtained the first time. Human error in the preparation of the cultures was suspected. However, the values obtained the second time were identical to those measured during the first round. The measured spectra for each culture 24 hours after the addition of either $BaCl_2$ or $SrCl_2$ are shown in Fig. 53-56. Spectra measured on day 3 and day 7 after the addition of $BaCl_2$ or $SrCl_2$ are shown in the Supp. Fig. 9-16.

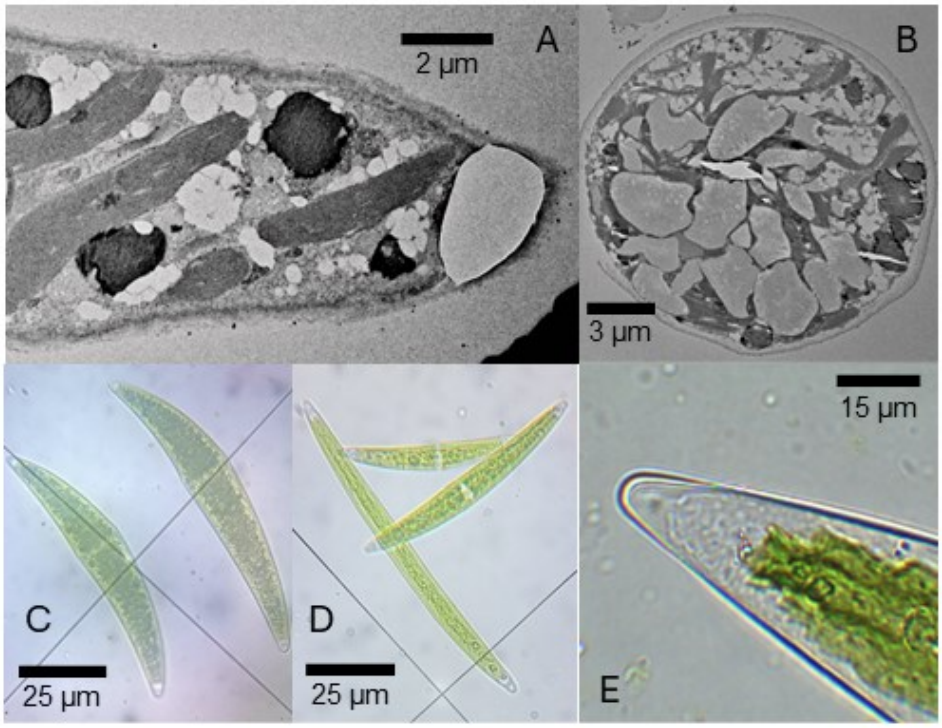

Figure 51: Exemplary images of algal cultures used in this thesis. TEM image of NIES-68 sliced lengthwise, depicting the vacuole space at the tip of the cell (A). TEM image of NIES-68 sliced across the cell (B). Images from the optical microscope of NIES-68 (C), NIES-173 (D) and details of NIES-173 cell tip vacuole containing barite crystals (E).

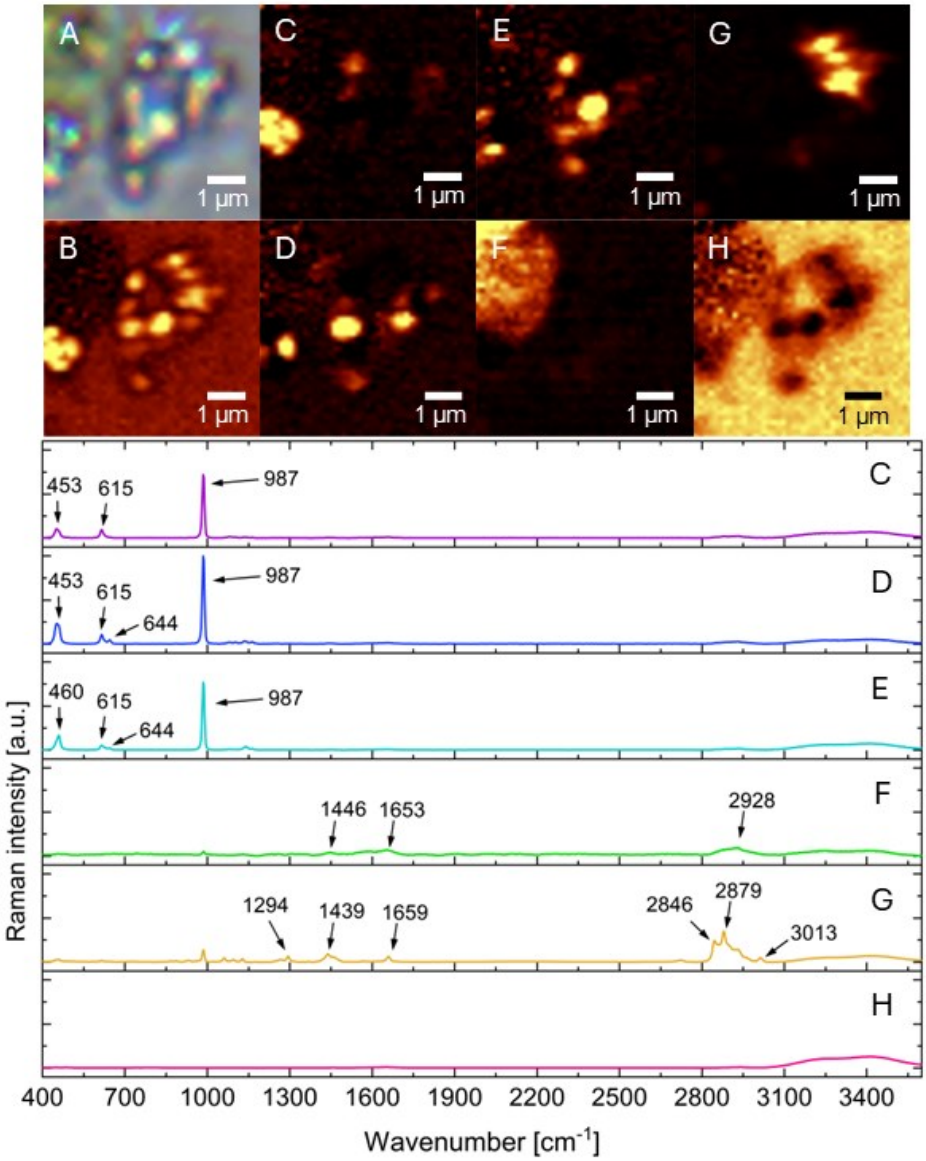

Figure 52: Typical Raman measurement of algal cell 1 day after addition of $BaCl_2$. Image from the optical microscope (A), Raman intensity map for the peak at 987 cm^{-1} (B), individual spectral components, their corresponding spectra and localization in the sample: barite crystals (C-E), proteins (F), lipids (G) and water (H).

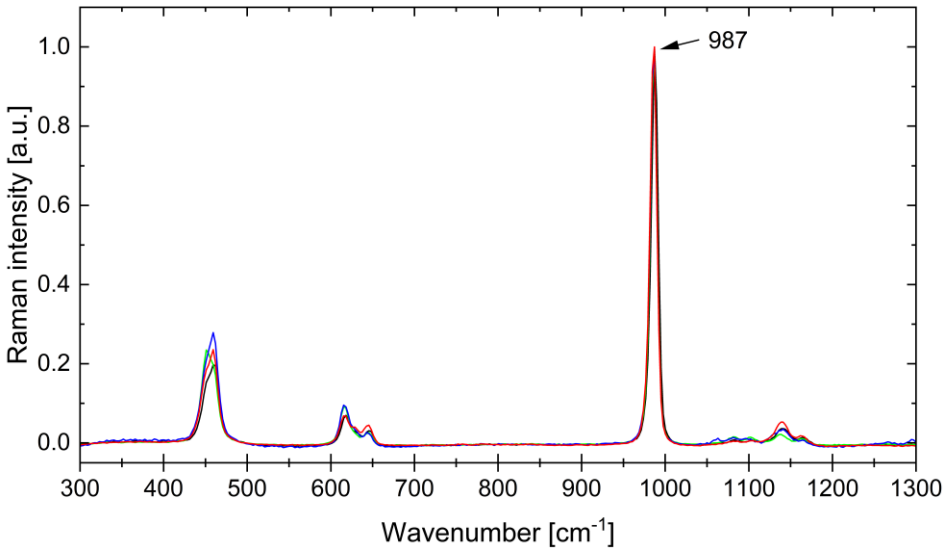

Figure 53: Measured spectra of NIES-68, 1 day after the addition of $BaCl_2$ to the culture media. The presence of a peak at 987 cm^{-1} suggests barite formation.

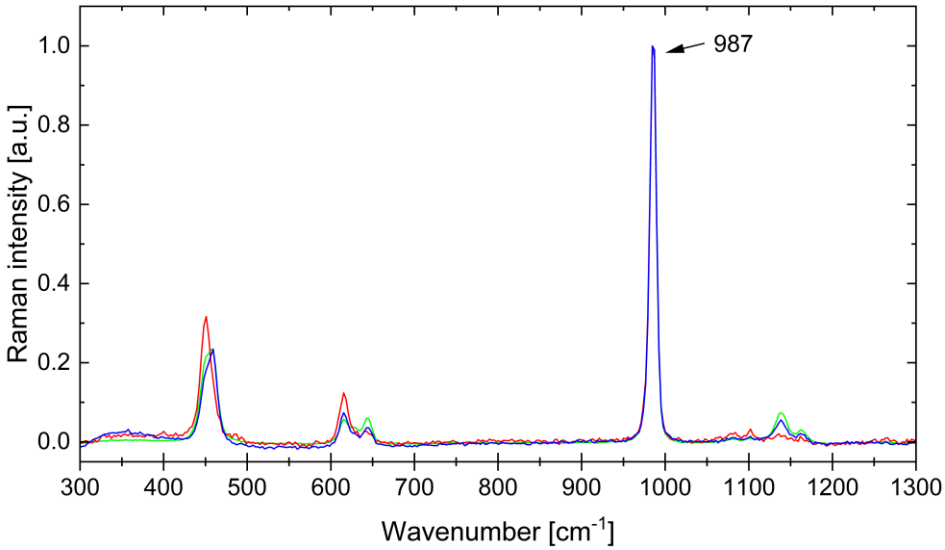

Figure 54: Measured spectra of NIES-68, 1 day after the addition of $SrCl_2$ to the culture media. The presence of a peak at 987 cm^{-1} suggests barite formation.

In Fig. 53-56, the characteristic region for barite/celestine of measured cell spectra is shown. Independently on the strain or the added solution, only pure barite crystals were formed inside the NIES-68 and NIES-173 cells as indicated by the presence of the Raman band at 987 cm^{-1}. The industrial separation of Ba and Sr is probably difficult, therefore the strontium solution used even with purity ≥99.99 % presumably contained enough residual Ba for pure barite formation. This evidence suggests extreme selectivity for Ba over Sr of the two strains used in this experiment.

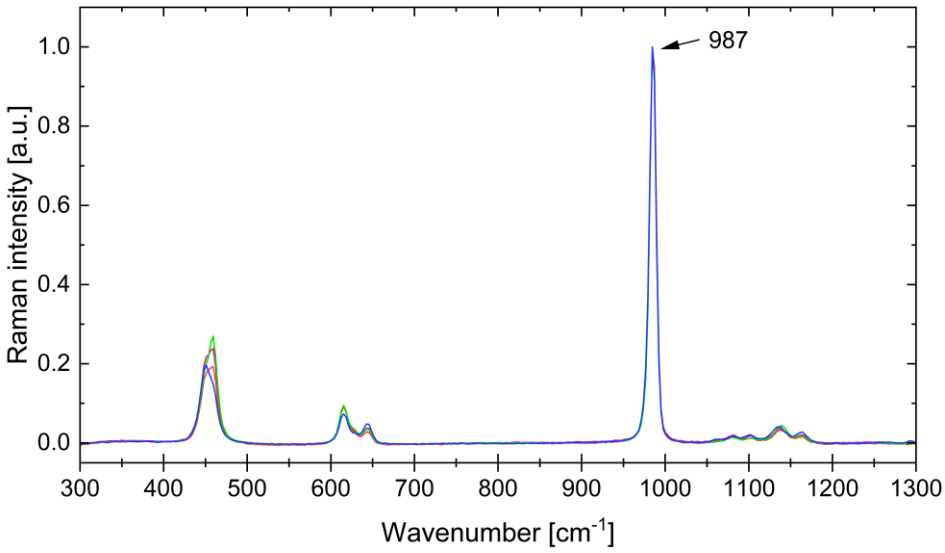

Figure 55: Measured spectra of NIES-173, 1 day after the addition of $BaCl_2$ to the culture media. The presence of a peak at 987 cm^{-1} suggests barite formation.

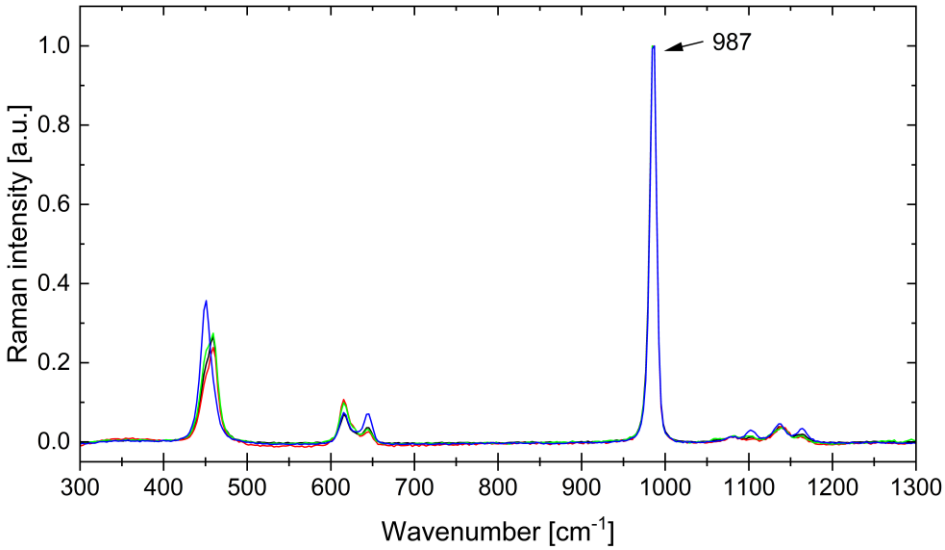

Figure 56: Measured spectra of NIES-173, 1 day after the addition of $SrCl_2$ to the culture media. The presence of a peak at 987 cm^{-1} suggests barite formation.

4. Discussion

The samples of the barium/strontium sulphate series exhibit four spectral regions of interest, corresponding to the internal vibrations of sulphate. The position of these regions depends on the cation present in the compound. The main peak, which serves as a reliable indicator of the presence or absence of sulphate compounds, can be found in the spectral range of 987-1000 cm^{-1}. For pure barite (x = 0, represented in purple in Fig. 19), the peak maximum is located at 987 cm^{-1}, whereas for pure celestine (x = 1, shown in red in Fig. 19), the peak maximum is located at 1000 cm^{-1}. The second most prominent region, albeit only 20% in intensity with respect to the main peak is located at the spectral range of 450-465 cm^{-1} and is shown in Fig. 20. The doublet peak located in this region does not exhibit any positional changes concerning different Ba:Sr ratios. However, we discovered that the intensity ratio between the individual maxima of the doublet changes significantly depending on the crystal orientation with respect to the polarization of excitation radiation as shown in Fig. 23. Last two spectral regions at 610-660 cm^{-1} (shown in Fig. 21) and 1120-1190 cm^{-1} (shown in Fig. 22) exhibit similar changes in peaks positions as main peak with respect to the Ba:Sr ratio.

Co-crystal samples of the sulphate series display intriguing behaviour. Barite precipitates transferred to the $SrCl_2$ solution tend to form an outer layer or shell. This phenomenon can be clearly seen in Raman maps, with spatially distributed components of different ratios between the peaks corresponding to the barite and celestine as shown in Fig. 24. On the other hand, celestine precipitates transferred to the $BaCl_2$ solution do not form an outer layer. Instead, it appears that celestine particles in $BaCl_2$ solution undergo at least partial dissolution in $BaCl_2$ solution. Therefore, these small particles of the celestine act as a nucleation core for crystal growth, resulting in the formation of strontium-enriched barite. The dissolution of celestine particles and consequent barite or strontium-enriched barite formation might be a supporting factor in the hypothesis for marine barite formation as proposed by (Bernstein & Byrne, 2004).

Similarly to the sulphate series, the samples of the monophosphate series exhibit one high-intensity peak and several spectral regions with lower-intensity peaks. The main peak can be found in the spectral range of 944-948 cm^{-1}. In the case of pure $BaPO_4$ (x

= 0, represented in purple in Fig. 26), the peak maximum is located at 944 cm^{-1}, and for pure $SrPO_4$ (x = 1, shown in red in Fig. 26), the peak maximum is located at 948 cm^{-1}. In contrast to the sulphate series, other spectral regions of the phosphate series do not exhibit any changes in peak position concerning Ba:Sr ratio (as shown in Figs. 27 and 28). Additionally, no doublet peaks in the spectra therefore no dependence on the crystal orientation with respect to the polarization of excitation radiation was found.

For diphosphate series samples two intense spectral regions were identified, with their intensity ratio in the range of 0.3-0.4 across all the samples. The main peak is positioned in the spectral range of 1025-1031 cm^{-1}. The lower value located at 1025 cm^{-1} represents pure barium diphosphate (x = 0, represented in purple in Fig. 29) and the higher value positioned at 1031 cm^{-1} represents pure strontium diphosphate (x = 1, represented in red in Fig. 29). In the second spectral region of interest the measured maxima of the peaks can be found in the range of 722-745 cm^{-1} as shown in Fig. 30. One interesting phenomenon can be observed, which cannot be fully explained with our current data. With increasing wavenumber, the first maximum corresponds to pure strontium diphosphate, the next maximum to pure barium diphosphate and further maxima to the compounds gradually decreasing in barium content.

Finally, the spectra of triphosphate series samples exhibit the most intriguing behaviour as shown in Fig 31. Similarly to the diphosphate series, we identified two intense spectral regions. However, as the barium content in the precipitated crystals gradually decreases, the maxima of the two last samples of the series shifts suddenly by 30 cm^{-1}. In the zoomed part of Fig. 31 wide side wing of the peak can be seen. This evidence suggests that the main peak of these two samples is the convolution of two peaks. One being more intense, and the position of its maximum would be identical with the one measured. The second, less intense peak could naturally extend the trend observed in peak maxima. The second spectral region located in the range of 730-763 cm^{-1} exhibits a similar shift in peak maxima for the last two samples of the series as shown in Fig.32.

The experiments involving BaF_2 yielded slightly expected results. All phosphate groups containing solutions, except for hexametaphosphate, bound to the surface of the BaF_2 (as shown in Figs. 34, 36, 39, 41, 43) were successfully substituted by

sulphate in the time span of 24 hours (as shown in Fig. 35,37,40,42,44), resulting in the barite formation on the surface of BaF_2 crystal. This evidence leads to the conclusion that sulphate has a higher affinity for barium than phosphate. However, in the case of diphosphate solution the presence of a peak corresponding to the diphosphate, even after 24 hours in sulphate solution might be a significant discovery. The hypothesis for barite formation mediated through EPS is based on the presence of phosphate groups acting as a pre-concentrator of barium ions. On the other hand, in a marine environment, the ubiquity of sulphate would immediately result in barite formation, therefore the mechanism of "shielding" the barium bound to the EPS must be present. If a "shielding" mechanism in barite formation mediated by EPS is provided by the diphosphate, this question would be resolved.

In the first part of the experiment, the DNA-agarose and pure agarose sheets were exposed only to the barium solution and measured. For the DNA-agarose sheet, the presence of barite crystals is documented (as shown in Fig. 46). As for the pure agarose sheet no barite crystals were located as indicated by the absence of the peak at 987 cm^{-1} (as shown in Fig. 47). This phenomenon can be explained with the binding of barium ions to the phosphate groups of DNA and consequent barite formation with the residual sulphate in the agarose (up to 0.1% of dry weight according to the manufacturer).

In the second part of the experiment the DNA-agarose and pure agarose sheets were exposed to the a) $BaCl_2$ solution and $NaSO_4$ solution (Fig. 48, 49, b) $SrCl_2$ solution and $NaSO_4$ solution (Fig. 50, 51) and c) equimolar solution of $BaCl_2$ and $SrCl_2$, and afterwards $NaSO_4$ solution (Fig. 52 53). In the first two cases, a) and b), particles of pure barite and celestine respectively were formed. For the equimolar solution of $BaCl_2$ and $SrCl_2$, heavily strontium-enriched barite particles were formed as indicated by the presence of a peak at 990 cm^{-1} in Fig. 52 and 53. This phenomenon can be explained by higher solubility of celestine or preferential binding of barium to the phosphate groups of DNA, although the former is more likely as the peak at 990 cm^{-1} is also present in the pure agarose sheets.

In the third and final part of the experiment with DNA-agarose sheets, the dilution series of barium solution to which the sheets were exposed was performed to estimate the ability of phosphate groups of DNA to bind barium in contrast to the pure agarose

sheets. As the series progressed the formed barite particles became smaller and were located less often in the samples as shown in the Fig. 50.

In the experiment involving algal cultures and their exposure to the $BaCl_2$ or $SrCl_2$ barium or strontium solution, only pure barite crystals were identified and measured for both strains as shown in Fig. 53-56. This scenario might have happened under one of these assumptions: a) occurrence of human error and the $BaCl_2$ solution was used instead of $SrCl_2$ solution, b) another occurrence of human error and the wrong sample was measured, c) the purity of $SrCl_2$ solution was falsely stated as ≥99.99% or d) the *Closterium* strains NIES-68 and NIES-173 possess extreme levels of selectivity and preference for Ba over Sr. While assumptions a) and b) are most likely to occur, the experiment was performed twice exactly for this reason. After evaluating the results from the first round of measurement, the second round was performed with utmost care and diligence. Even though we were unable to determine the exact purity of the $SrCl_2$ used for the preparation of the solution, we performed the control measurement of precipitated crystals from this solution by adding Na^2SO^4. The produced particles exhibited the Raman band at 1000 cm^{-1}, thus crystals of pure celestine were measured and we could rule out assumption c). Therefore, option d) must be true and *Closterium* strains NIES-68, and NIES-173 possess extreme levels of selectivity for Ba over Sr.

5. Conclusion

In this diploma thesis, we studied crystals of different molar Ba:Sr ratios precipitated from the solution by adding Na_2SO_4, HNa_2O_4P, $Na_4O_7P_2$, and $Na_5O_{10}P_3$. For the Na_2SO_4 series, we identified a Raman band in the spectral range 987-1000 cm^{-1} as a reliable spectral marker for the Ba:Sr molar ratio of the crystals. The Raman band is positioned at 987 cm^{-1} for pure barite, and at 1000 cm^{-1} for pure celestine and changes practically linearly in between depending on the molar ratio of Ba:Sr. The position of this Raman band can thus serve as a proxy for estimating the molar ratio of barium to strontium in mixed crystals. Furthermore, we have found that the ratio between the intensity of the individual maxima of the doublet Raman band at 453-462 cm^{-1} is strongly dependent on the crystal orientation with respect to the polarization of excitation beam and can serve for discerning differently oriented microcrystals.

For the HNa_2O_4P series, the position of the most intense Raman band of monophosphate crystals changes only slightly from 944 cm^{-1} for pure $BaPO_4$ to 948 cm^{-1} for pure $SrPO_4$. The shift seems to be relatively small and linear only for the Sr:Ba molar ratio 0 – 0.9. The band position shows a jump of 2 cm^{-1} if barium ions are completely absent from the solution. This indicates that the influence of barium ions prevails in the mixed complexes. For the $Na_4O_7P_2$ series, similar behaviour was observed. The position of the most intense Raman band changes from 1025 cm^{-1} for pure $Ba_2P_2O_7$ to 1031 cm^{-1} for pure $Sr_2P_2O_7$ and an asymmetric broadening occurs for the Sr:Ba ratios below 0.9. For the $Na_5O_{10}P_3$ series, the position of the most intense Raman band changes only slightly between 1027 cm^{-1} for pure $Ba_3P_3O_{10}$ to 1032 cm^{-1} for the Sr:Ba ratio 0.9. For pure $Sr_3P_3O_{10}$ (molar ratio Sr:Ba 1:0) and sudden shift from 1032 cm^{-1} to 1059 cm^{-1} was detected. This peculiar behaviour can be attributed to the higher affinity of the phosphate groups for barium than for strontium ions, where even with a relative excess of strontium, the influence of barium will become more apparent. In addition, the relatively higher affinity of phosphate groups for barium seems to increase with the length of the phosphate chain. This higher affinity could explain the pre-concentration of barium on EPS containing a large amount of phosphate groups. For none of these phosphate series, the dependence of the other bands on the polarization of the excitation beam was observed, which means that the aggregates formed are probably amorphous.

Measurements on DNA-agarose sheets used as a model system for EPS in testing the hypothesis of the formation of barite by a bacterial mechanism confirm the active participation of PO4 groups in the preconcentration of barium, which could facilitate the formation of barite even in conditions of its extremely low concentrations. The finding that the formation of barite microcrystals in DNA-agarose sheets occurs even when these sheets are exposed to solutions with a very low concentration of barium shows that the preferential binding of barium to phosphate groups could be an explanation for the molecular mechanism by which some microorganisms can select between strontium and barium. Although it is still unclear how important is a role PO_4 in the selective pre-concentration of barium by EPS under real seawater conditions where sulphates are continuously present in high concentrations, our results suggest that the bacterial hypothesis reported by other authors may have a real basis. At the same time, it opens up the questions of which molecular mechanisms to select these two ions of similar chemical properties are used by various microorganisms selectively accumulating barite or celestine.

The experiment with solid-state BaF_2 yielded interesting results regarding the ability of diphosphate groups attached to the surface to resist sulphate substitution. Therefore, we propose a potential "shielding" effect of diphosphate groups of EPS for pre-concentrated barium ions.

Finally, accumulation experiments with two different *Closterium* strains NIES-68 and NIES-173 confirmed high preference of these freshwater microalgae for barium accumulation and barite formation than for strontium. The preference for barite could be related to its higher specific density, which may be important for its biological function as specific weight. However, our results showed that this selectivity is probably much higher than indicated by the few studies published so far by other authors. If we exclude significantly higher chemical contamination of the chemicals obtained from two suppliers than declared by the manufacturers, these microalgae were able to selectively accumulate barium even from “pure” $SrCl_2$, where barium ions should represent only as residual contamination. Our experiments also showed that confocal Raman microscopy is a very useful and practical tool for studying the formation of these inclusions in microorganisms, because it is significantly simpler than electron microscopy in terms of sample preparation and applicability, and it can

provide a number of important information about the chemical composition of microcrystals and their morphological heterogeneity.

.

Bibliography

Aloisi, G., Wallmann, K., Bollwerk, S. M., Derkachev, A., Bohrmann, G., & Suess, E. (2004). The effect of dissolved barium on biogeochemical processes at cold seeps. *Geochimica et Cosmochimica Acta*, *68*(8), 1735-1748. https://doi.org/10.1016/j.gca.2003.10.010

Barbosa, N., Jaquet, J.-M., Urquidi, O., Adachi, T. B. M., & Filella, M. (2022). Combined *in vitro* and *in vivo* investigation of barite microcrystals in *Spirogyra* (Zygnematophyceae, Charophyta). *Journal of Plant Physiology*, *276*, 153769. https://doi.org/https://doi.org/10.1016/j.jplph.2022.153769

Bernstein, R. E., & Byrne, R. H. (2004). Acantharians and marine barite. *Marine Chemistry*, *86*(1-2), 45-50. https://doi.org/10.1016/j.marchem.2003.12.003

Bernstein, R. E., Byrne, R. H., Betzer, P. R., & Greco, A. M. (1992). Morphologies and transformations of celestite in seawater: The role of acantharians in strontium and barium geochemistry. *Geochimica et Cosmochimica Acta*, *56*(8), 3273-3279. https://doi.org/10.1016/0016-7037(92)90304-2

Bernstein, R. E., Byrne, R. H., & Schijf, J. (1998). Acantharians: a missing link in the oceanic biogeochemistry of barium. *Deep-Sea Research Part I: Oceanographic Research Papers*, *45*(2-3), 491. https://doi.org/10.1016/s0967-0637(97)00095-2

Bertram, M. A., & Cowen, J. P. (1997). Morphological and compositional evidence for biotic precipitation of marine barite. *Journal of Marine Research*, *55*(3), 577-593. https://doi.org/10.1357/0022240973224292

Bishop, J. K. B. (1988). The barite-opal-organic carbon association in oceanic particulate matter. *Nature*, *332*(6162), 341-343. https://doi.org/10.1038/332341a0

Bowers, T. S., Jackson, K. J., & Helgeson, H. C. (1984). *Equilibrium Activity Diagrams: For Coexisting Minerals and Aqueous Solutions at Pressures and Temperatures to 5 KB and 600°C*. Springer-Verlag. https://doi.org/10.1007/978-3-642-46511-6

Brook, A. J., Fotheringham, A., Bradly, J., & Jenkins, A. (1980). Barium accumulation by desmids of genus Closterium (Zygnemaphyceae). *British Phycological Journal*, *15*(3), 261-264. https://doi.org/10.1080/00071618000650251

Brook, A. J., Grime, G. W., & Watt, F. (1988). A study of barium accumulation in desmids using the Oxford scanning proton microprobe (SPM). *Nuclear Instruments & Methods in Physics Research Section B-Beam Interactions with Materials and Atoms*, *30*(3), 372-377. https://doi.org/10.1016/0168-583x(88)90027-4

Chan, L. H., Drummond, D., Edmond, J. M., & Grant, B. (1977). On the barium data from the Atlantic GEOSECS expedition. *Deep Sea Research*, *24*(7), 613-649. https://doi.org/10.1016/0146-6291(77)90505-7

Chang, L. L. Y., Deer, W. A., Howie, R. A., & Zussman, J. (1998). *Rock-forming Minerals: Non-Silicates, Volume 5B; Sulphates, Carbonates, Phosphates and Halides*. Geological Society. https://doi.org/10.1180/minmag.1996.060.400.20

Chester, R. (1990). *Marine Geochemistry*. Island Press. https://doi.org/10.1007/978-94-010-9488-7

Church, T. M., Guichard, F., Treuil, M., & Jaffrezic, H. (1979). Rare-earths in barites - distribution and effects on aqueous partitioning. *Geochimica et*

Cosmochimica Acta, *43*(7), 983-997. https://doi.org/10.1016/0016-7037(79)90088-7

Cremer, C., Kaufmann, R., Gunkel, M., Pres, S., Weiland, Y., Müller, P., Ruckelshausen, T., Lemmer, P., Geiger, F., Degenhard, S., Wege, C., Lemmermann, N. A., Holtappels, R., Strickfaden, H., & Hausmann, M. (2011). Superresolution imaging of biological nanostructures by spectral precision distance microscopy. *Biotechnol J*, *6*(9), 1037-1051. https://doi.org/10.1002/biot.201100031

De Lange, G. J., Boelrijk, N. A. I. M., Catalano, G., Corselli, C., Klinkhammer, G. P., Middelburg, J. J., Müller, D. W., Ullman, W. J., Van Gaans, P., & Woittiez, J. R. W. (1990). Sulphate-related equilibria in the hypersaline brines of the Tyro and Bannock Basins, eastern Mediterranean. *Marine Chemistry*, *31*(1), 89-112. https://doi.org/10.1016/0304-4203(90)90032-8

De Lange, G. J., Middelburg, J. J., Van der Weijden, C. H., Catalano, G., Luther, G. W., Hydes, D. J., Woittiez, J. R. W., & Klinkhammer, G. P. (1990). Composition of anoxic hypersaline brines in the Tyro and Bannock Basins, eastern Mediterranean. *Marine Chemistry*, *31*(1), 63-88. https://doi.org/10.1016/0304-4203(90)90031-7

Dehairs, F., Chesselet, R., & Jedwab, J. (1980). Discrete Suspended Particles of Barite and the Barium Cycle in the Open Ocean. *Earth and Planetary Science Letters*, *49*(2), 528-550. https://doi.org/10.1016/0012-821x(80)90094-1

Dehairs, F., Stroobants, N., & Goeyens, L. (1991). Suspended barite as a tracer of biological activity in the Southern Ocean. *Marine Chemistry*, *35*(1-4), 399-410. https://doi.org/10.1016/s0304-4203(09)90032-9

Dey, T. (2022). Microplastic pollutant detection by Surface Enhanced Raman Spectroscopy (SERS): a mini-review. *Nanotechnology for Environmental Engineering*, *8*(1), 41-48. https://doi.org/10.1007/s41204-022-00223-7

Falkner, K. K., klinkhammer, G. P., Bowers, T. S., Todd, J. F., Lewis, B. L., Landing, W. M., & Edmond, J. M. (1993). The behavior of barium in anoxic marine waters. *Geochimica et Cosmochimica Acta*, *57*(3), 537-554. https://doi.org/10.1016/0016-7037(93)90366-5

Fisher, N. S., Guillard, R. R. L., & Bankston, D. C. (1991). The accumulation of barium by marine phytoplankton grown in culture. *Journal of Marine Research*, *49*(2), 339-354. https://doi.org/10.1357/002224091784995882

Gaines, R. V., Dana, J. D., & Dana, E. S. (1997). *Dana's New Mineralogy: The System of Mineralogy of James Dwight Dana and Edward Salisbury Dana* (8 ed.). Wiley.

Gonzalez-Munoz, M. T., Fernandez-Luque, B., Martinez-Ruiz, F., Ben Chekroun, K., Arias, J. M., Rodriguez-Gallego, M., Martinez-Canamero, M., de Linares, C., & Paytan, A. (2003). Precipitation of barite by *Myxococcus xanthus*: Possible implications for the biogeochemical cycle of barium. *Applied and Environmental Microbiology*, *69*(9), 5722-5725. https://doi.org/10.1128/aem.69.9.5722-5725.2003

Gonzalez-Munoz, M. T., Martinez-Ruiz, F., Morcillo, F., Martin-Ramos, J. D., & Paytan, A. (2012). Precipitation of barite by marine bacteria: A possible mechanism for marine barite formation. *Geology*, *40*(8), 675-678. https://doi.org/10.1130/g33006.1

Gooday, A. J., & Nott, J. A. (1982). Intracellular barite crystals in 2 xenophyophores, Aschemonella amuliformis and Galatheammina sp (Protozoa, Rhizopoda) with comments on the taxonomy of Aschemonella ramuliformis. *Journal of*

the Marine Biological Association of the United Kingdom, *62*(3), 595-605. https://doi.org/10.1017/s0025315400019779

Griffith, E. M., & Paytan, A. (2012). Barite in the ocean - occurrence, geochemistry and palaeoceanographic applications. *Sedimentology*, *59*(6), 1817-1835. https://doi.org/10.1111/j.1365-3091.2012.01327.x

Hanor, J. S. (2000). Barite–Celestine Geochemistry and Environments of Formation. *Reviews in Mineralogy and Geochemistry*, *40*(1), 193-275. https://doi.org/10.2138/rmg.2000.40.4

Hein, J. R., Zierenberg, R. A., Maynard, J. B., & Hannington, M. D. (2007). Barite-forming environments along a rifted continental margin, Southern California Borderland. *Deep-Sea Research Part Ii-Topical Studies in Oceanography*, *54*(11-13), 1327-1349. https://doi.org/10.1016/j.dsr2.2007.04.011

Hollricher, O., & Ibach, W. (2010). High-Resolution Optical and Confocal Microscopy. In T. Dieing, O. Hollricher, & J. Toporski (Eds.), *Confocal Raman Microscopy* (pp. 1-20). Springer Berlin Heidelberg. https://doi.org/10.1007/978-3-642-12522-5_1

Horner, T. J., Pryer, H. V., Nielsen, S. G., Crockford, P. W., Gauglitz, J. M., Wing, B. A., & Ricketts, R. D. (2017). Pelagic barite precipitation at micromolar ambient sulfate. *Nature Communications*, *8*(1), 1342. https://doi.org/10.1038/s41467-017-01229-5

Jamieson, J. W., Hannington, M. D., Tivey, M. K., Hansteen, T., Williamson, N. M. B., Stewart, M., Fietzke, J., Butterfield, D., Frische, M., Allen, L., Cousens, B., & Langer, J. (2016). Precipitation and growth of barite within hydrothermal vent deposits from the Endeavour Segment, Juan de Fuca Ridge. *Geochimica et Cosmochimica Acta*, *173*, 64-85. https://doi.org/10.1016/j.gca.2015.10.021

Javed, Y., Ali, K., Akhtar, K., Jawaria, Hussain, M. I., Ahmad, G., & Arif, T. (2018). TEM for Atomic-Scale Study: Fundamental, Instrumentation, and Applications in Nanotechnology. In S. K. Sharma (Ed.), *Handbook of Materials Characterization* (pp. 147-216). Springer International Publishing. https://doi.org/10.1007/978-3-319-92955-2_5

Jeandel, C., Dupré, B., Lebaron, G., Monnin, C., & Minster, J. F. (1996). Longitudinal distributions of dissolved barium, silica and alkalinity in the western and southern Indian Ocean. *Deep Sea Research Part I: Oceanographic Research Papers*, *43*(1), 1-31. https://doi.org/10.1016/0967-0637(95)00098-4

Kravchishina, M., Prokofiev, V., Dara, O., Baranov, B., Klyuvitkin, A., Iakimova, K., Kalgin, V., Lein, A., Poonoosamy, J., & Brandt, F. (2023). Fluid Inclusion Studies of Barite Disseminated in Hydrothermal Sediments of the Mohns Ridge. *Minerals*, *13*, Article 1117. https://doi.org/10.3390/min13091117

Krejci, M. R., Finney, L., Vogt, S., & Joester, D. (2011). Selective Sequestration of Strontium in Desmid Green Algae by Biogenic Co-precipitation with Barite. *Chemsuschem*, *4*(4), 470-473. https://doi.org/10.1002/cssc.201000448

Krejci, M. R., Wasserman, B., Finney, L., McNulty, I., Legnini, D., Vogt, S., & Joester, D. (2011). Selectivity in biomineralization of barium and strontium. *Journal of Structural Biology*, *176*(2), 192-202. https://doi.org/10.1016/j.jsb.2011.08.006

Martinez-Ruiz, F., Paytam, A., Gonzalez-Munoz, M. T., Jroundi, F., Abad, M. M., Lam, P. J., Bishop, J. K. B., Horner, T. J., Morton, P. L., & Kastner, M.

(2019). Barite formation in the ocean: Origin of amorphous and crystalline precipitates. *Chemical Geology*, *511*, 441-451. https://doi.org/10.1016/j.chemgeo.2018.09.011

Maynard, J. B., & Okita, P. M. (1991). Bedded barite deposits in the United States, Canada, Germany, and China - two major types based on tectonic setting. *Economic Geology and the Bulletin of the Society of Economic Geologists*, *86*(2), 364-376. https://doi.org/10.2113/gsecongeo.86.2.364

Mojzeš, P., Palacký, J., Bauerová, V., & Bednárová, L. (2011). Ramanova mikrospektroskopie a mapování buněk a tkání. *Československý časopis pro fyziku*, *61*(3), 178-184.

Monnin, C. (1999). A thermodynamic model for the solubility of barite and celestite in electrolyte solutions and seawater to 200°C and to 1 kbar. *Chemical Geology*, *153*(1-4), 187-209. https://doi.org/10.1016/s0009-2541(98)00171-5

Moore, J. W. (1991). *Inorganic contaminants of surface water: research and monitoring priorities* (1 ed.). Springer New York, NY. https://doi.org/10.1007/978-1-4612-3004-5

Niedermeier, M., Gierlinger, N., & Lütz-Meindl, U. (2018). Biomineralization of strontium and barium contributes to detoxification in the freshwater alga *Micrasterias*. *Journal of Plant Physiology*, *230*, 80-91. https://doi.org/10.1016/j.jplph.2018.08.008

Paytan, A., & Griffith, E. M. (2007). Marine barite: Recorder of variations in ocean export productivity [Review]. *Deep-Sea Research Part Ii-Topical Studies in Oceanography*, *54*(5-7), 687-705. https://doi.org/10.1016/j.dsr2.2007.01.007

Paytan, A., Kastner, M., & Chavez, F. P. (1996). Glacial to interglacial fluctuations in productivity in the equatorial Pacific as indicated by marine barite. *Science*, *274*(5291), 1355-1357. https://doi.org/10.1126/science.274.5291.1355

Paytan, A., Mearon, S., Cobb, K. M., & Kastner, M. (2002). Origin of marine barite deposits: Sr and S isotope characterization. *Geology*, *30*(8), 747-750. https://doi.org/10.1130/0091-7613(2002)030<0747:Oombds>2.0.Co;2

Pilátová, J., Tashyreva, D., Týč, J., Vancová, M., Bokhari Syed Nadeem, H., Skoupý, R., Klementová, M., Küpper, H., Mojzeš, P., & Lukeš, J. (2023). Massive accumulation of strontium and barium in diplonemid protists. *mBio*, *14*(1), e03279-03222. https://doi.org/10.1128/mbio.03279-22

Raven, J. A., & Knoll, A. H. (2010). Non-Skeletal Biomineralization by Eukaryotes: Matters of Moment and Gravity. *Geomicrobiology Journal*, *27*(6-7), 572-584. https://doi.org/10.1080/01490451003702990

Ray, D., Kota, D., Das, P., Prakash, L. S., Khedekar, V. D., Paropkari, A. L., & Mudholkar, A. V. (2014). Microtexture and Distribution of Minerals in Hydrothermal Barite-Silica Chimney from the Franklin Seamount, SW Pacific: Constraints on Mode of Formation. *Acta Geologica Sinica-English Edition*, *88*(1), 213-225. https://doi.org/10.1111/1755-6724.12192

Rhein, M., Chan, L. H., Roether, W., & Schlosser, P. (1987). 226Ra and Ba in northeast Atlantic deep water. *Deep Sea Research Part A. Oceanographic Research Papers*, *34*(9), 1541-1564. https://doi.org/10.1016/0198-0149(87)90108-7

Rushdi, A. I., McManus, J., & Collier, R. W. (2000). Marine barite and celestite saturation in seawater. *Marine Chemistry*, *69*(1-2), 19-31. https://doi.org/10.1016/s0304-4203(99)00089-4

Shipp, D. W., Sinjab, F., & Notingher, I. (2017). Raman spectroscopy: techniques and applications in the life sciences. *Advances in Optics and Photonics*, *9*(2), 315-428. https://doi.org/10.1364/AOP.9.000315

Torres, M. E., Brumsack, H. J., Bohrmann, G., & Emeis, K. C. (1996). Barite fronts in continental margin sediments: A new look at barium remobilization in the zone of sulfate reduction and formation of heavy barites in diagenetic fronts. *Chemical Geology*, *127*(1-3), 125-139. https://doi.org/10.1016/0009-2541(95)00090-9

van Beek, P., François, R., Conte, M., Reyss, J. L., Souhaut, M., & Charette, M. (2007). $^{228}Ra/^{226}Ra$ and $^{226}Ra/Ba$ ratios to track barite formation and transport in the water column. *Geochimica et Cosmochimica Acta*, *71*(1), 71-86. https://doi.org/10.1016/j.gca.2006.07.041

Von Damm, K. L. (1995). Controls on the chemistry and temporal variability of seafloor hydrothermal fluids. In S. E. Humphris (Ed.), *Seafloor Hydrothermal Systems: Physical, Chemical, Biological, and Geochemical Interactions*. American Geophysical Union. https://doi.org/10.1029/gm091p0222

Widanagamage, I. H., Waldron, A. R., & Glamoclija, M. (2018). Controls on Barite Crystal Morphology during Abiotic Precipitation. *Minerals*, *8*(11), 15, Article 480. https://doi.org/10.3390/min8110480

Wilcock, J. R., Perry, C. C., Williams, R. J. P., & Brook, A. J. (1989). Biological Minerals Formed from Strontium and Barium Sulphates. II. Crystallography and Control of Mineral Morphology in Desmids. *Proceedings of the Royal Society Series B-Biological Sciences*, *238*(1292), 203. https://doi.org/10.1098/rspb.1989.0077

List of Tables

List of Figures

Supplementary

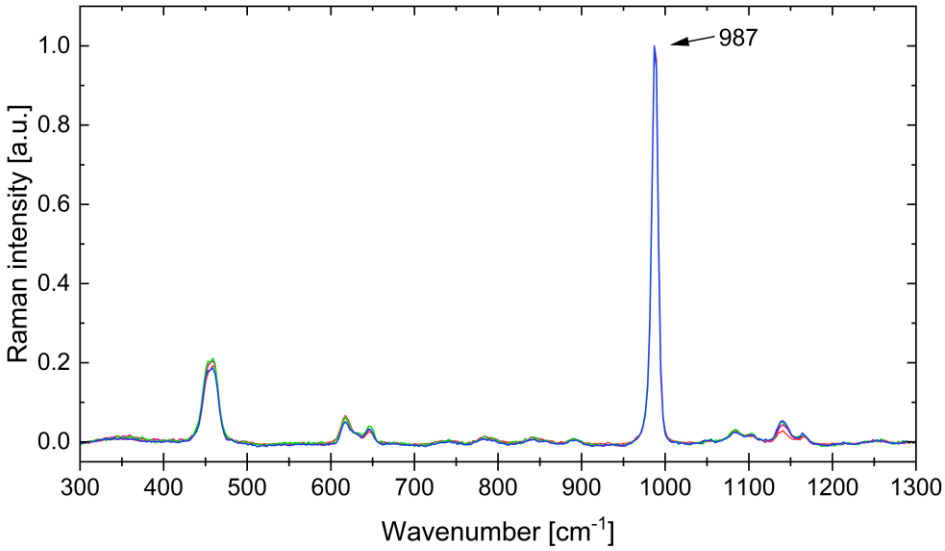

Supplementary Figure 1: Raman spectra of DNA-agarose sheet exposed to the 10× diluted $BaCl_2$ solution (5 mM) and Na_2SO_4 solution. The peak at 987 cm^{-1} suggests the presence of barite crystals.

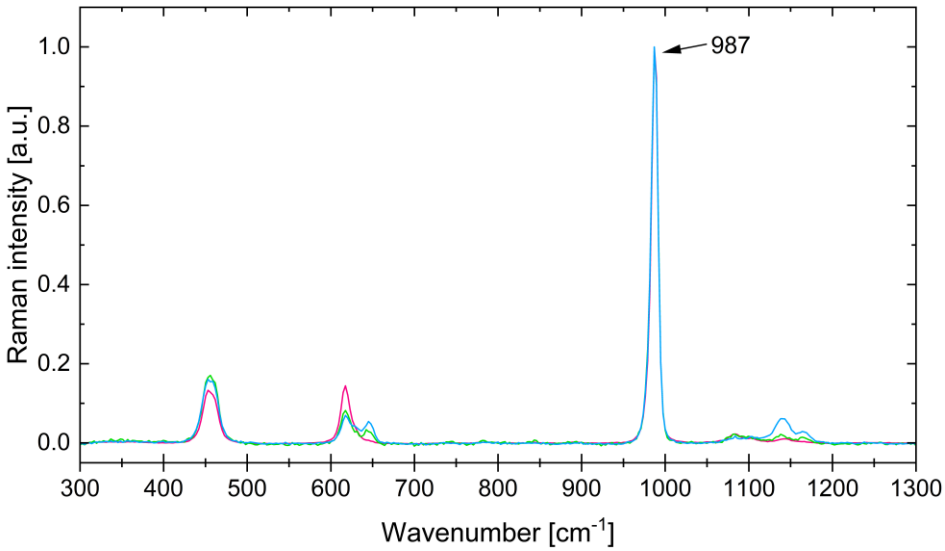

Supplementary Figure 2: Raman spectra of DNA-agarose sheet exposed to the 100× diluted $BaCl_2$ solution (500 µM) and Na_2SO_4 solution. The peak at 987 cm^{-1} suggests the presence of barite crystals.

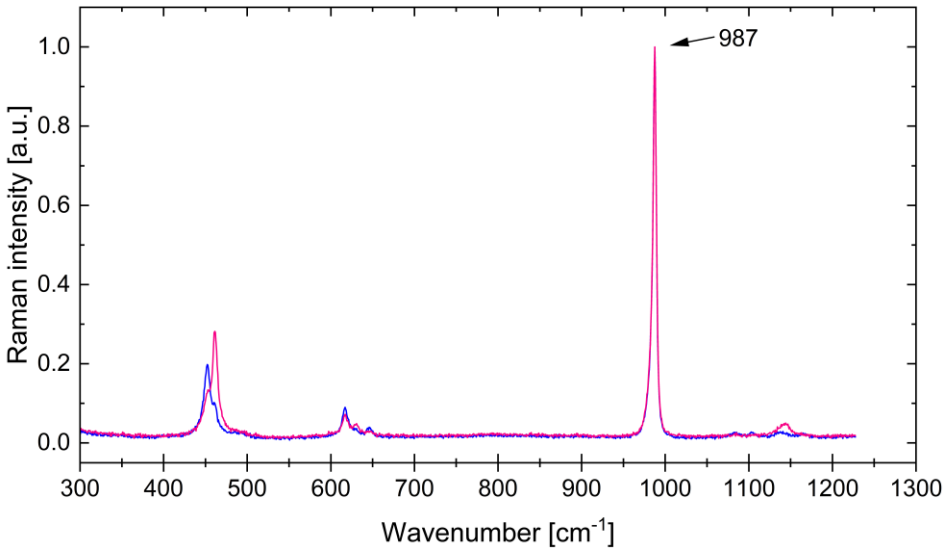

Supplementary Figure 3: Raman spectra of DNA-agarose sheet exposed to the 1000× diluted $BaCl_2$ solution (50 µM) and Na_2SO_4 solution. The peak at 987 cm^{-1} suggests the presence of barite crystals.

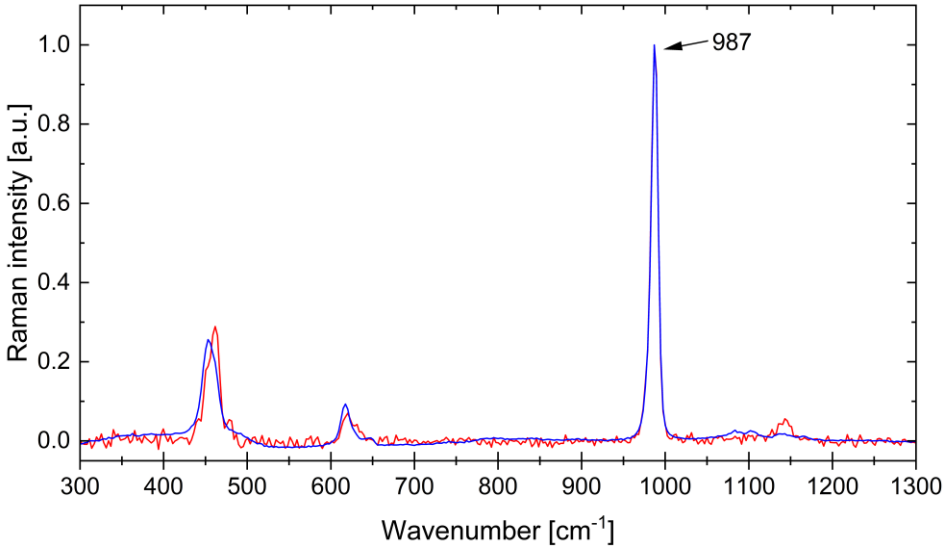

Supplementary Figure 4: Raman spectra of DNA-agarose sheet exposed to the 10 000× diluted $BaCl_2$ solution (5 µM) and Na_2SO_4 solution. The peak at 987 cm^{-1} suggests the presence of barite crystals.

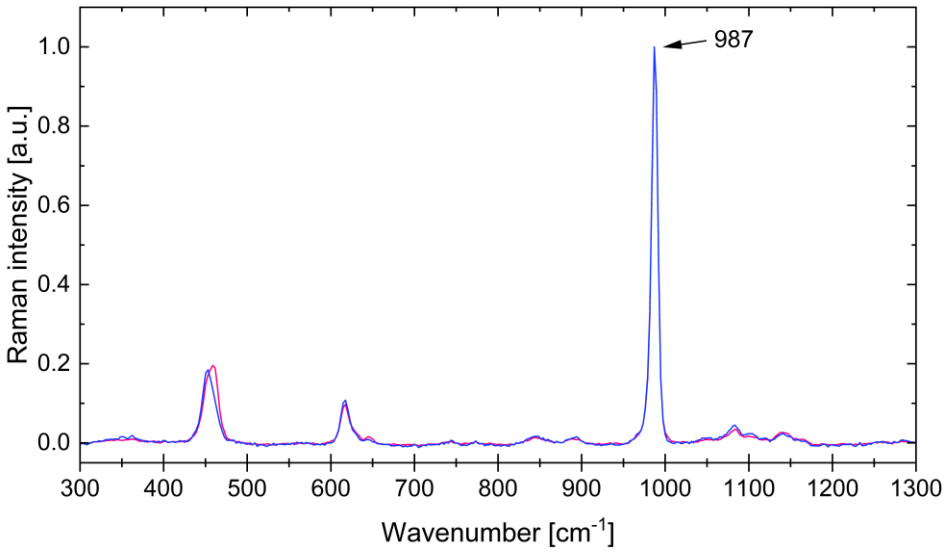

Supplementary Figure 5: Raman spectra of pure agarose sheet exposed to the 10× diluted $BaCl_2$ solution (5 mM) and Na_2SO_4 solution. The peak at 987 cm^{-1} suggests the presence of barite crystals.

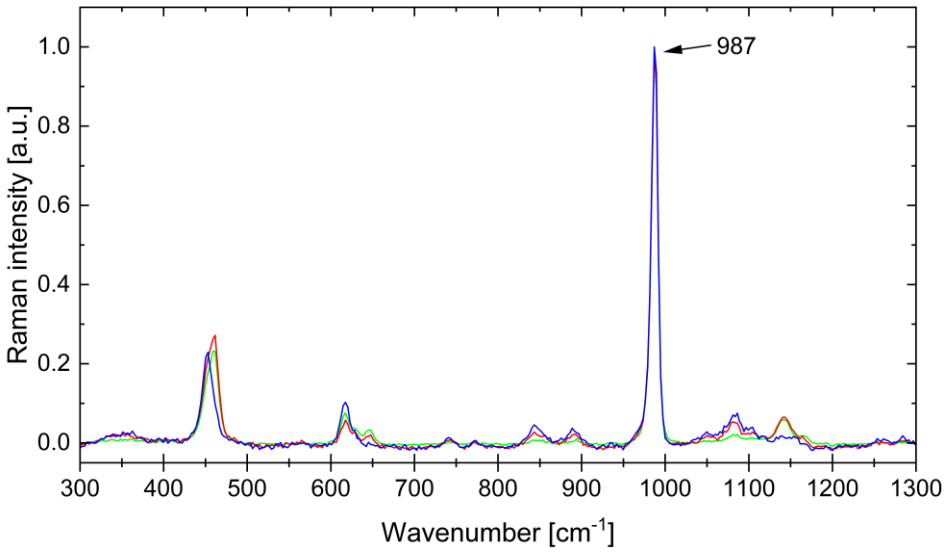

Supplementary Figure 6: Raman spectra of pure agarose sheet exposed to the 100× diluted $BaCl_2$ solution (500 µM) and Na_2SO_4 solution. The peak at 987 cm^{-1} suggests the presence of barite crystals.

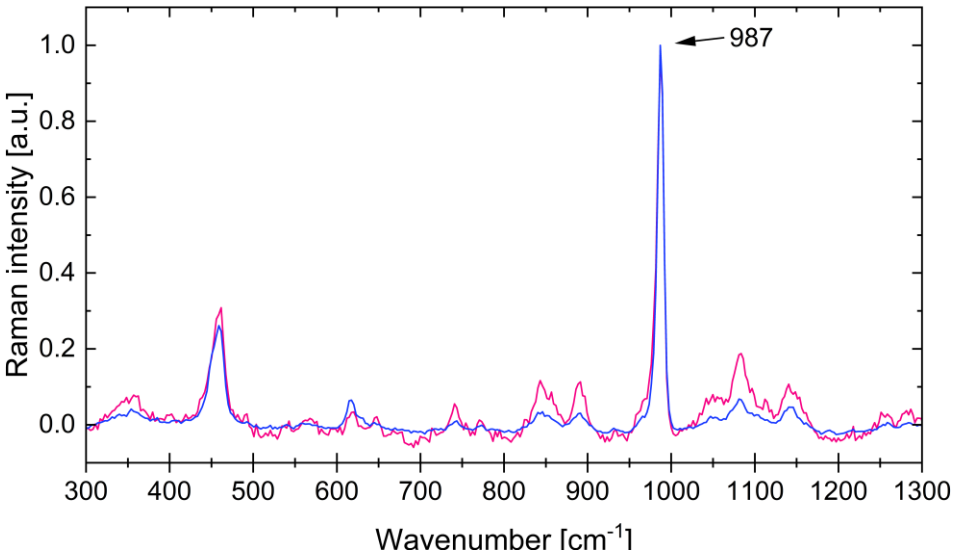

Supplementary Figure 7: Raman spectra of pure agarose sheet exposed to the 1000× diluted $BaCl_2$ solution (50 µM) and Na_2SO_4 solution. The peak at 987 cm^{-1} suggests the presence of barite crystals.

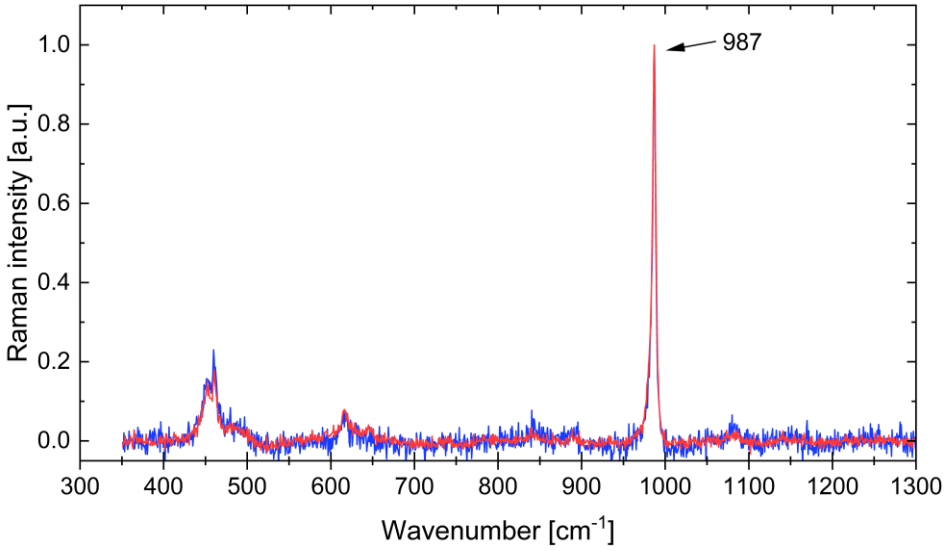

Supplementary Figure 8: Raman spectra of pure agarose sheet exposed to the 10 000× diluted $BaCl_2$ solution (5 µM) and Na_2SO_4 solution. The peak at 987 cm^{-1} suggests the presence of barite crystals.

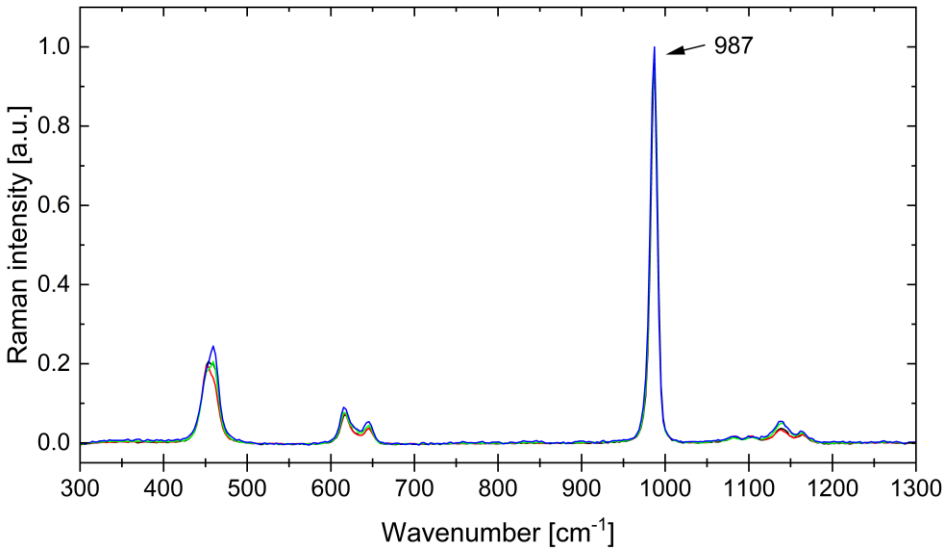

Supplementary Figure 9: Measured spectra of NIES-68, 3 days after the addition of $BaCl_2$ to the culture media.

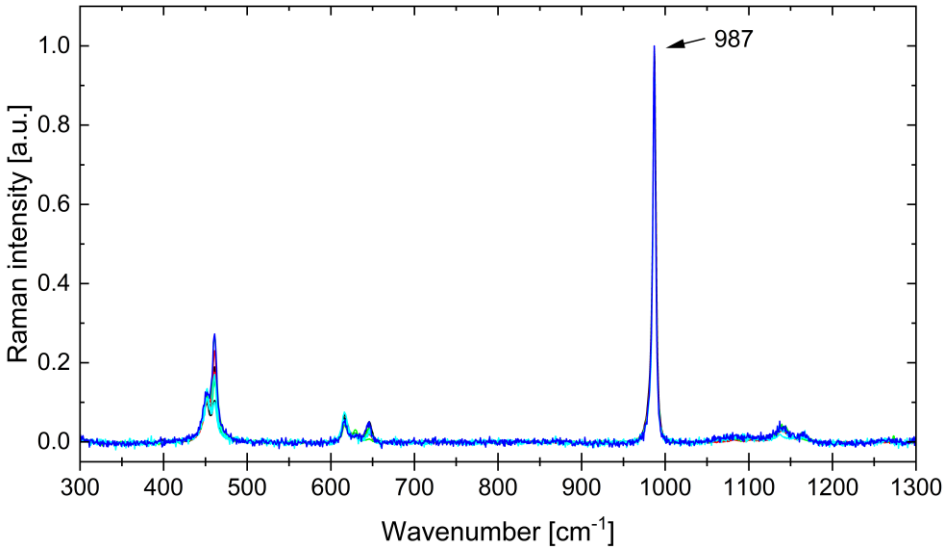

Supplementary Figure 10: Measured spectra of NIES-68, 7 days after the addition of $BaCl_2$ to the culture media.

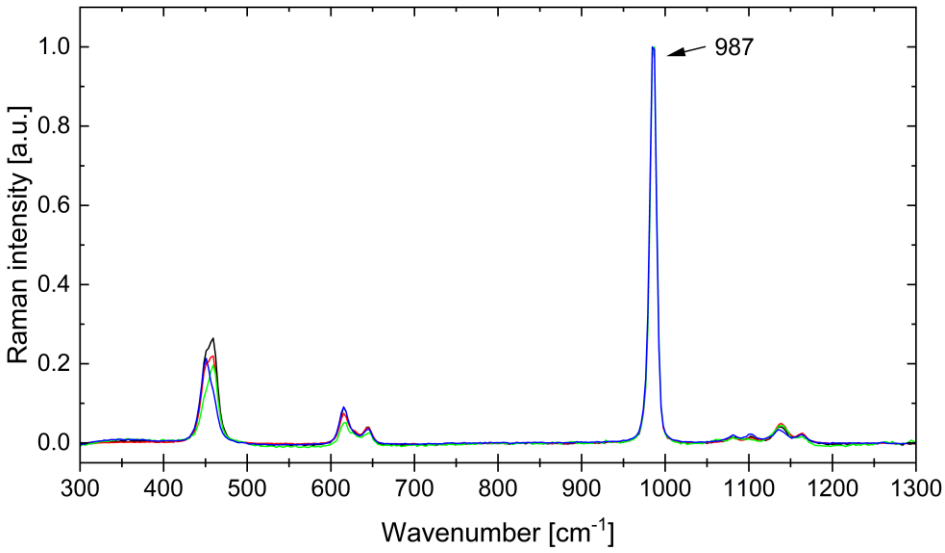

Supplementary Figure 11: Measured spectra of NIES-68, 3 days after the addition of $SrCl_2$ to the culture media.

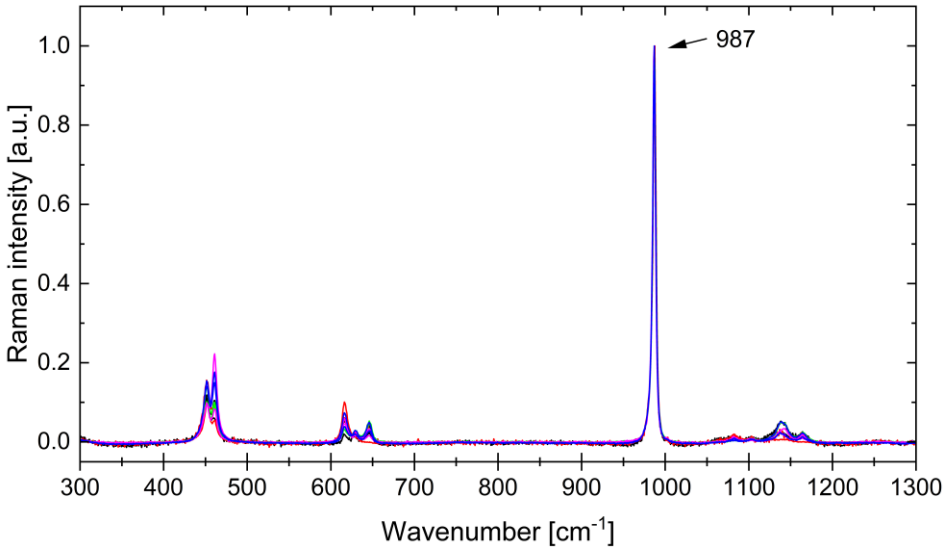

Supplementary Figure 12: Measured spectra of NIES-68, 7 days after the addition of $SrCl_2$ to the culture media.

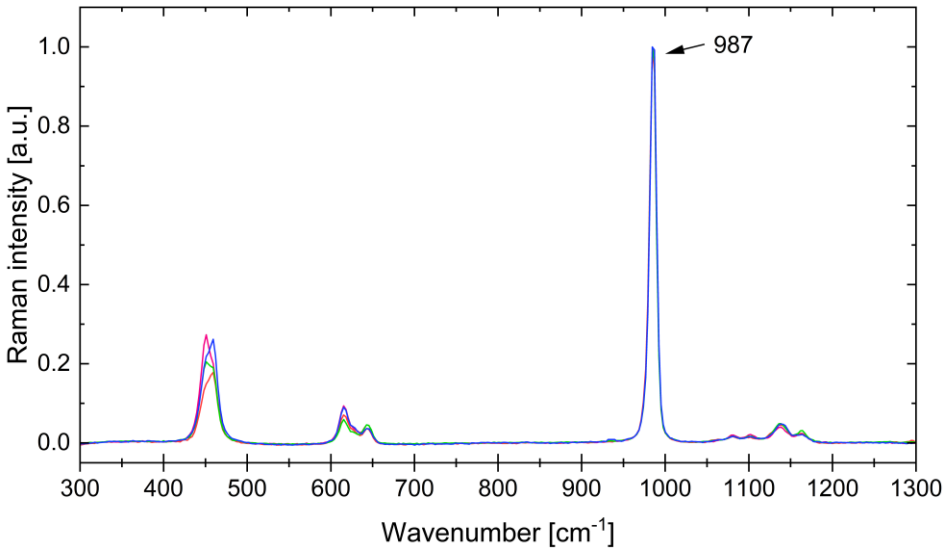

Supplementary Figure 13: Measured spectra of NIES-173, 3 days after the addition of $BaCl_2$ to the culture media.

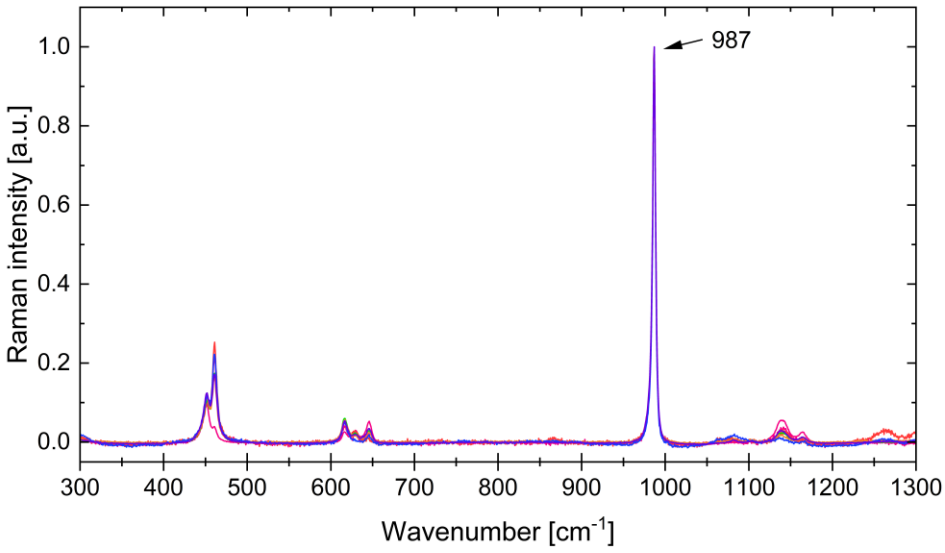

Supplementary Figure 14: Measured spectra of NIES-173, 7 days after the addition of $BaCl_2$ to the culture media.

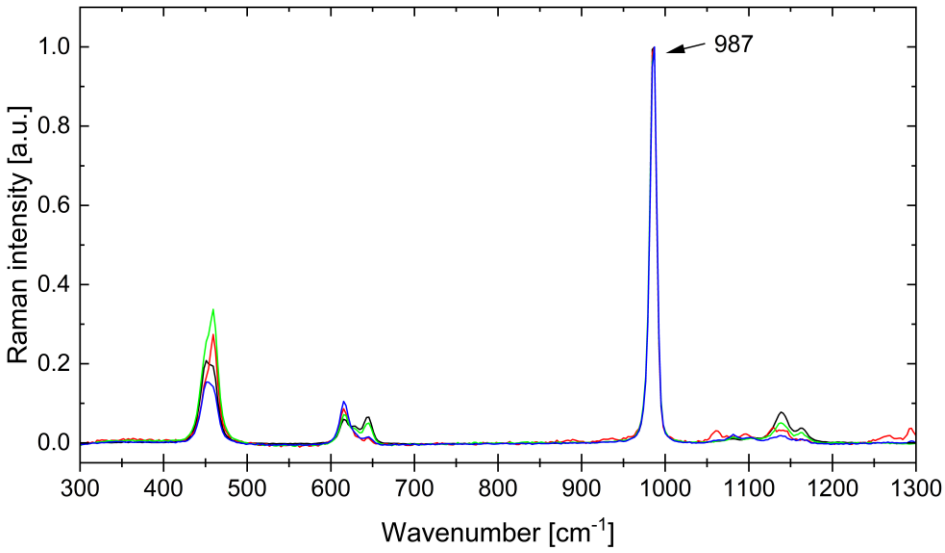

Supplementary Figure 15: Measured spectra of NIES 173, 3 days after the addition of $SrCl_2$ to the culture media.

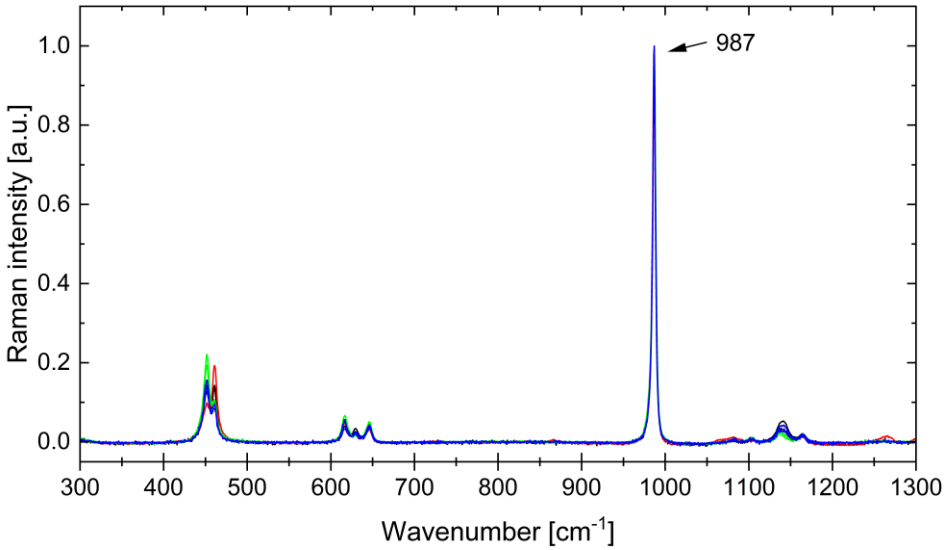

Supplementary Figure 16: Measured spectra of NIES 173, 7 days after the addition of $SrCl_2$ to the culture media.